University of California
Los Angeles

Some Non-linear Aspects of Ultra-intense, Laser-Plasma Interactions

A dissertation submitted in partial satisfaction
of the requirements for the degree
Doctor of Philosophy in Electrical Engineering

by

Fang Fang

2008

The dissertation of Fang Fang is approved.

Warren B. Mori

Francis F. Chen

Steve Cowley

Chandrashekhar J. Joshi, Committee Chair

University of California, Los Angeles

2008

To my beloved husband, Hongjian, Li and yet to be born son, Paul Li.

Table of Contents

List of Figures

List of Tables

Acknowledgments

There are many individuals I would like to acknowledge at UCLA for their help with my graduate study for the past four and half years. First and foremost I offer my sincerest gratitude to my advisor, Dr Chan Joshi, who recruited and supported and supervised me throughout my PhD study with his patience and knowledge. I feel very lucky to have been one of his students because his expectations of his students are very high. Because he is always standing at a much higher vantage point, his brilliant guidance during my data analysis and thesis writing have been more valuable than I can express.

I want to thank Dr Chris Clayton, with whom I spent the most time in the lab and from whom I learned the most. His knowledge of experimental techniques, data analysis and technical writing is encyclopaedic. I also owe my great appreciation to Ken Marsh, who for months stayed late and helped me with my experiments. For this, I also owe my thanks to his wife Beth and his two daughters, Olivia and Natalie. I also want to thank my fellow student Joe Ralph for staying late with me to help with my experiment even during the time his wife was pregnant with their second son. So I also owe my appreciation to his wife, Naomi and his two little sons, Tobi and Cory. Also thank my other fellow student, Arthur Pak, for staying late for my experiment during the later days and the advices he gave to me on making Monday meeting reports and presentations. I want to thank everybody in this group, including the new student Tyanlin Wang and the graduated student Chad Vandenbosch, for the numerous discussions, encouragement and friendship. They are like family members to me. I am sure I will miss them.

I would also like to thank Nelson Lopes, a visiting scholar from Instituto Superior Tecnico in Portugal, for his help with the lasers and my early work on

laser guiding through capillary discharges. Thanks Carmen Constantin for her help while she was a postdoc in our lab. Patric Muggli, a research scientist of USC, also gave me a lot of good advices. Thank them all for their encouragement during my hard times. Thanks to Sergei Tochitsky, Neptune research scientist, for his good comments on my talks and the kindness of lending lab tools to me.

The simulations presented in this thesis were done in Prof. Warren Mori's laser plasma simulation group of UCLA. I would like to acknowledge Wei Lu, Frank Tsung, Miaomiao Zhou, and Chengkun Huang for their help with my simulations and numerous discussions.

Thanks to Prof. Frank Chan, Prof. Worren Mori and Prof. Steve Cowley for agreeing to serve as members of my thesis committee.

I also want to show my appreciation to Maria for her help with all the administrative tasks which made my life easier.

I would also want to show my special thanks to my advisor and his wife Asha, and their son Neel and daughter Tera for their warmth on Thanksgiving evenings and the delicious dinners. My husband and I spent our Thanksgivings in their home for the past 5 years.

Finally, on a more personal note, I would like to thank my parents and my husband for their support and love during all these years of my study and my yet to be born son for his company and stimulation throughout the whole time of my thesis writing.

This work was supported by NNSA Grant no. DE-FG52- 03NA00138, and DOE Grant no DE-FG02-92ER40727

Vita

April 14, 1976	Born, Shangqiu, P. R. China
1999	B. S., Physics, Henan University, Kaifeng, P. R. China
2001	M. S., Plasma Physics, Institute of Plasma Physics, Chinese Academy of Sciences, Hefei, P. R. China
1999	M. S., Condensed Matter Physics, University of Minnesota at Twin Cities, Minneapolis, Minnesota
2008	PhD, Plasma Electronics, University of California at Los Angeles, Los Angeles, California

Publications

F. Fang et al., *Plasma wave front evolution due to photon acceleration*, to be submitted.

F. Fang et al., *Laser Group Velocity Drop Induced by Photon Deceleration in a Plasma*, Particle accelerator conference proceeding, NM, 2007

F. Fang et al., *Laser focusing through a Plasma lens*, Proceedings of the 12th Advanced Accelerator Concepts Workshop, Lake Geneva, WI, 2006

Abstract of the Dissertation

Some Non-linear Aspects of Ultra-intense, Laser-Plasma Interactions

by

Fang Fang

Doctor of Philosophy in Electrical Engineering

University of California, Los Angeles, 2008

Professor Chandrashekhar J. Joshi, Chair

Ultra-intense, laser-plasma interactions refers to physical processes that occur when subpicosecond laser pulses are focused in an underdense or solid target plasmas to give relativistic intensities. In this thesis one such process, the forced excitation of a wake in underdense plasma, is experimentally investigated. In this process a non-optimal (2-3 plasma wavelengths long rather than one half plasma wavelength long), but intense ($a_0 \sim 1$) laser pulse relativistically self-focuses and evolves spatially and temporally as it propagates through the plasma. As a result of these changes it can excite a large amplitude wakefield that can trap and accelerate plasma electrons. It is this so-called "forced-laser wakefield accelerator" (F-LWFA) regime that is studied in this thesis by carefully monitoring the velocity at which a plasma density front associated with the wakefield propagates through various phases of these changes until the laser pulse finally becomes too weak to excite the wakefield. We find that there are four overlapping but distinguishable phases of the evolution of the wakefield in this regime.

First the wakefield appears to move superluminaly as the laser pulse relativistically self-focuses and its peak intensity increases by up to a factor of 9. There-

after the wakefield density front propagates at approximately the nonlinear group velocity of the laser in the plasma. This occurs over approximately one linear dephasing length. In the third phase, the wakefield density front begins to slow down. This slowdown is thought to be related to photon frequency downshifting as a consequence of energy transfer to the wake. Indeed forward transmitted spectrum measurements show significant red-shifting of the spectrum. Finally the wakefront rapidly recedes relative to the laser pulse as the laser pulse pump depletes.

Three-dimensional particle-in-cell code simulations of our experiment reproduce many of the features of our experiment discussed above although the agreement on the electron spectrum observed in the experiment and the simulation is at best qualitative. As a result of interaction between the trapped electrons and the laser electric field the emittance is seen to be blown up in the simulations whereas in the experiment, round relatively high quality electron beams with equal emittance in both directions are often observed. This discrepancy requires further investigation.

CHAPTER 1

Introduction

The physics of Laser-plasma interactions had been under study for many years before the laser intensity was high enough to create relativistic effects in plasmas. After the invention of the chirped pulse amplification (CPA) technique [1–8], it was possible to amplify short (sub-picosecond) laser pulses to high energies and thus, focused laser intensities jumped from $10^{16} W cm^{-2}$ to well above $10^{18} W cm^{-2}$ [9]. In this ultra-intense laser-plasma interaction regime, relativistic effects start playing a major and sometimes dominant role in determining the fate of the phenomena that occur. This relativistic regime has many applications: e.g., x-ray lasers [10–13], inertial confinement fusion via the fast ignitor concept [14,15], and laser-plasma based accelerators [16–22].

Prior to the advent of the CPA laser, a relatively low-intensity, two-wavelength laser ($I < 10^{15} W cm^{-2}$) was used in a plasma accelerator scheme called the plasma beat wave accelerator (PBWA) to excite a relativistically-propagating electron plasma wave (REPW) [23]. A REPW has a phase velocity v_p close to the speed of light c. In this scheme, the REPW is resonantly excited to large amplitudes by using N beats present in the interference-envelope of the two-wavelength laser pulse with $N \gg 1$. To achieve the resonant condition the difference frequency between the two lasers is matched to the plasma frequency. For a useful accelerator, the phase velocity v_p of the REPW must be such that $\gamma \equiv \frac{1}{\left(1-\frac{v_p^2}{c^2}\right)^{1/2}} \gg 1$, so

that an accelerating electron can interact with the longitudinal accelerating field of the wave for a long distance. Since $v_p \equiv \omega_p/k_p$, $\gamma \gg 1$ requires that $k_p \approx \omega_p/c$. Here $\omega_p(k_p)$ is the frequency (wavenumber) of the REPW. Early experiments on PBWA indeed found that such a wave could be excited to reasonably large amplitudes and preaccelerated electrons could be trapped and accelerated by such a structure over a distance of about 1cm [24–28].

With the advent of CPA lasers, intense, single-frequency-pulses could be used to drive the REPW to accelerate either self-trapped or externally injected electrons. This scheme is called the laser wake field accelerator (LWFA). The LWFA was first proposed by Tajima and Dawson [16]. There are four distinct regimes for LWFA: the linear or resonant regime, the self-modulated regime, the forced regime and the bubble regime. These four regimes will be briefly described below.

The resonant regime is when the full width at half maximum of the laser pulse duration τ_L satisfies $c\tau_L \simeq 1/2\lambda_p$, where λ_p is the plasma wavelength and the laser is modestly relativistic, i.e. the normalized vector potential $a \sim \frac{eA}{mc^2} \sim 1$. This is analogous to the classic *pi*-pulse experiments in resonant atomic systems [29]. In a one dimensional picture, where the laser spot size is larger than the plasma wavelength the excitation of the wake can be described as follows: The longitudinal ponderomotive force of the laser pulse, which is proportional to the gradient of the laser intensity, pushes the plasma electrons both forward and backward, from the region of high to low laser intensity. The more massive ions are immobile and exert a restoring space-charge force on the displaced electrons as the laser passes by. The displaced electrons over shoot their original positions and form a periodic oscillation of the electron density; a longitudinal electron plasma wave. Hamster et al [30] were the first to measure microwave radiation from a He plasma generated by an intense short laser pulse as a function of a wide

range of He pressures and found a strong enhancement of the radiation at the resonant condition $c\tau \simeq \frac{1}{2}\lambda_p$. The clean radiation signal at the plasma frequency ω_p produced by the process of inverse mode conversion indicated that a strong and stable plasma wake field was excited. Several groups subsequently probed these wakes in this resonant regime using either injected electrons [31] or probe photons [32,33] and found that these were in fact radial waves because laser spot sizes used were much smaller than λ_p to achieve $a_0 \sim 1$. That is, the transverse ponderomotive force of the laser pulse pushed the electrons out from the axis. As a result this linear-resonant LWFA regime envisioned by Tajima and Dawson has not been produced to-date in experiments. Furthermore, these experiments occurred without any observed "dark current"; that is, no self-trapped electrons.

The self-modulated regime is when $c\tau \gg \frac{1}{2}\lambda_p$. Correspondingly, the LWFA in this regime is called the self-modulated laser wake field accelerator (SM-LWFA) [34–44]. To grow the relativistic plasma wave from noise, the plasma density has to be much higher than in the resonant LWFA case, and with a laser power $P \geq P_c$, where P_c is the critical power for relativistic guiding [45,46], to increase the laser-plasma interaction length. In the high density plasma, the laser pulse envelope is longitudinally modulated at the plasma period due to the beating of the pump beam and photons (that initially are scattered from plasma noise spectrum) at frequencies $\omega_0 \pm \omega_p$ and wavenumbers $k_0 \pm k_p$ (Stokes and anti-Stokes), where ω_0 is the center frequency of the pump beam. The ponderomotive force of the modulated laser pulse leads to an exponential growth of the plasma wave. This is why this process is extremely closely related to the one-dimensional, four-wave Raman forward scattering instability [47]. The red shifted sidebands can enhance this growth (due to theλ^2 scaling of the ponderomotive force) and results in a large density modulation (δn) of $\delta n \geq 0.5 n_0$, where n_0 is the average plasma density.

The first experimental evidence for the generation of MeV electrons via the breaking of plasma wave was in fact attributed to Raman Forward scattering in 1981, using a nanosecond long CO_2 laser pulse. More than a decade later the same process was observed using a CPA, 1μm laser by Coverdale et al and was attributed to wave growth via stimulated Raman forward and backward Raman scattering [38]. Two MeV electrons were observed in these experiments. Since then, electron acceleration has been observed by a many groups [38, 39, 47, 48], with energies up to a few hundred MeV. However the electron energy spectrum in this regime was typically broad and continuous.

As many applications favor a well collimated, short electron bunch with narrow energy spread, several schemes that have the potential to produce such electron bunches were proposed. Laser pulse duration of the CPA laser decreased further from $\sim 600 - 800fs$ using Nd:glass lasers to $50fs$ as Ti:Sapphire lasers were developed. A Forced LWFA (F-LWFA) regime was first termed by Malka et al [49] in 2002 to explain experimental results where the pulse was longer than that needed for resonant LWFA but too short so that forward Raman scattering could not be operational. When the intense laser pulse is longer (only a few times the plasma wave length λ_p), the laser pulse rapidly undergoes self-phase modulation, longitudinal compression by group velocity dispersion (GVD) [50–52], self-steepening in the front of the pulse by diffraction and a big increasing in a_0 due to both self-focusing and frequency down-shifting by photon deceleration. Thus the original somewhat longer laser pulse becomes shorter with most of the laser energy in the first two plasma wave "buckets" and more intense with a sharp rising edge. The laser intensity is large enough to completely blow-out all the plasma electrons radially. Some of these electrons as they are attracted back by the ions can now be trapped in this wake and accelerated.

A forth regime is the recently discovered ideal bubble regime. Here the laser pulse length is $\sim \lambda_p/2$ and intense enough to blow out all the plasma electrons which now form a sheath around the ion bubble. The returning electrons overshoot and set up a 3-dimensional wake. Because all the electrons expelled from the bubble will be in a thin sheath and will come back to the axis, the electron density in the back sheath of the bubble can be many times higher than the average plasma density, thus the electrons on the inside of the sheath will gain forward longitudinal momentum from both the electron sheath and the ion bubble, enough to be trapped in the bucket and accelerated. Simulations show that this trapping process can occur in the first few buckets. It is believed that, if a sufficient number of electrons are trapped, then the space-charge of these electrons will suppress further trapping and lead to one or more electron bunches with a relatively narrow energy spectrum if the plasma length is close to the dephasing length L_d, (will be discussed later in this chapter).

Interestingly none of the experiments to-date have been in the ideal bubble regime of the LWFA. And yet many groups have obtained evidence of quasi-mono-energetic electron beams. These experiments are all thought to be in the forced LWFA regime as discussed earlier. In 2004, three experimental groups [20–22] reported the generation of high charge ($\geq 0.1nC$) and low emittance quasi-monoenergetic electron beams with a center energy of a few hundred MeV. Very recently, a 1GeV beam was also observed in LBNL from a centimeter-scale plasma [53].

In LWFA, there are a few very important basic concepts that need to be introduced, which include the "self-focusing length" L_{sf}, "dephasing length" L_d, "pump depletion length" L_{pd} and "electron trapping threshold" E_{th}. Understanding these quantities is necessary for understanding the physics that will be

discussed in later this thesis.

A. Self-focusing length

The self-focusing of the laser pulse in a F-LWFA is mainly relativistic self-focusing, which further focuses the laser to a spot size a few times smaller than the vacuum spot size for the parameters of this experiment. Correspondingly, the laser intensity can be increased more than 10 times. This can easily cause a laser pulse, which was originally too weak to drive a large wave up to the wave breaking limit, to trap and accelerate electrons.

As known in nonlinear optics, the radial refraction index, $\eta_r = \eta_0 + \eta_2 I$, has a nonlinear term that depends on laser intensity. In a plasma, the refraction index can be expressed as [46]

$$\eta_r \simeq 1 - \frac{\omega_{p0}^2}{2\omega_0^2}\left(1 - \frac{a^2}{2}\right), \tag{1.1}$$

where ω_{p0} is the average plasma frequency and $a = \frac{eE}{mc\omega_0}$ is the vector potential. This formula is given in the weakly-relativistic limit ($a^2 \ll 1$).

Using this refraction index, the laser spot size evolution can be given by the following equation [54]:

$$\frac{d^2R}{dz^2} = \frac{1}{Z_R^2 R^3}\left(1 - \frac{P}{P_c}\right), \tag{1.2}$$

where $R = w/w_0$ is the normalized laser spot size, w_0 is the initial spot size entering the plasma (which we assume to be at a waist). $Z_R = \pi w_0^2/\lambda$ is the corresponding Rayleigh length, λ_0 is the laser wavelength, and $P_c(GW) \simeq 17.4\left(\omega_0/\omega_{p0}^2\right)$ is the critical power for relativistic self-focusing. The first term of this equation represents diffraction and the second term represents relativistic self-focusing.

The solution to Eq.1 with initial condition $dR/dz = 0$ at $z = 0$ is

$$\frac{w^2}{w_0^2} = 1 + \left(1 - \frac{P}{P_c}\right)\frac{z^2}{z_R^2}. \tag{1.3}$$

This solution indicates that the laser diffracts for $P < P_c$, remain guided for $P = P_c$ and self-focus for $P > P_c$. It also indicates a "catastrophic" focusing, the spot size w will go to zero and then negative, thus the theory breaks down. To estimate L_{sf}, the propagation length for the laser spot to self-focus to a minimum spot size w_{min}, $w_{min} = 0$ can be used to get a rough estimate. Therefore, from Eq.1.3, the self-focusing length can be expressed as

$$L_{sf} \simeq Z_R\sqrt{\frac{1}{\frac{P}{P_c} - 1}}. \tag{1.4}$$

For example, for a Ti:Sapphire laser with $w_0 = 10\mu$m and a power of ~ 2TW, propagating into a He plasma with a density of $5 \times 10^{19} cm^{-3}$, $L_{sf} \simeq 200\mu$m from Eq.1.4.

B. Dephasing length

In LWFA, as the electrons are trapped and accelerated by the longitudinal electric field of the plasma wave, their velocity will quickly increase and reach the speed of light, $v_{ez} \to c$. Here subscript e, z represent electron and the direction of propagation z. For highly relativistic electrons, $v_{ez} \simeq c$. The phase velocity of the plasma wave v_p is the same as the group velocity of the driving laser beam (v_g) assuming no evolution of the driver. In a underdense plasma with a density of n_p, $v_p \simeq v_g - v_{etch} \simeq c\left(1 - \frac{1}{2}\frac{\omega_p^2}{\omega_0^2}\right) < c$, Therefore, the electrons will eventually outrun the accelerating field of the plasma wave and begin to interact with the decelerating field. The total time it take for this to happen, assuming the electrons are at the beginning of the accelerating field, is called the dephasing

time t_d. This implies that the distance that the electrons move relative to the plasma wave is half the plasma wave length, hence $t_d\,(c - v_p) = \lambda_p/2$. Therefore the dephasing length is

$$\begin{aligned} L_d &= t_d c \\ &\simeq \frac{c\lambda_p}{2} \frac{1}{c\left(1 - \frac{v_p}{c}\right)} \frac{1 + \frac{v_p}{c}}{1 + \frac{v_p}{c}} \\ &\approx \frac{\lambda_p}{1 - \frac{c_p^2}{c^2}} \\ &= \gamma_p^2 \lambda_p \\ &\simeq \left(\omega_0^2/\omega_p^2\right) \lambda_p \end{aligned} \tag{1.5}$$

where $\gamma_p \simeq \omega_0^2/\omega_p^2$ in an underdense plasma. Eq.1.5 is the formula for the dephasing in linear limit ($a_0 \ll 1$). In the nonlinear case ($a_0 \gg 1$), wave steepening and the associated increasing of the nonlinear plasma wavelength for one-dimensional waves occur as the wave amplitude grows. The nonlinear plasma wavelength (for $a_0 > 1$) is given as [55]

$$\lambda_{NL} = (2/\pi)\left(1 + \left(a_0^2/2\right)\right) \lambda_p. \tag{1.6}$$

Therefore, considering both the linear and nonlinear cases together, the dephasing length can be given as follows [56]

$$L_d \simeq \left(\omega_0^2/\omega_p^2\right) \lambda_p \begin{cases} 1, & \text{for } a_0^2 \ll 1 \\ 2a_0^2/\pi, & \text{for } a_0^2 > 1, \end{cases} \tag{1.7}$$

For example, the dephasing length in a LWFA with a Ti:Sapphire laser and a plasma with a density of $5 \times 10^{19} cm^{-3}$ is $L_d \simeq 200\mu$m from Eq.1.7. The dephasing length response with the change of a_0 is shown in Fig.1.1. If the laser a_0 increases

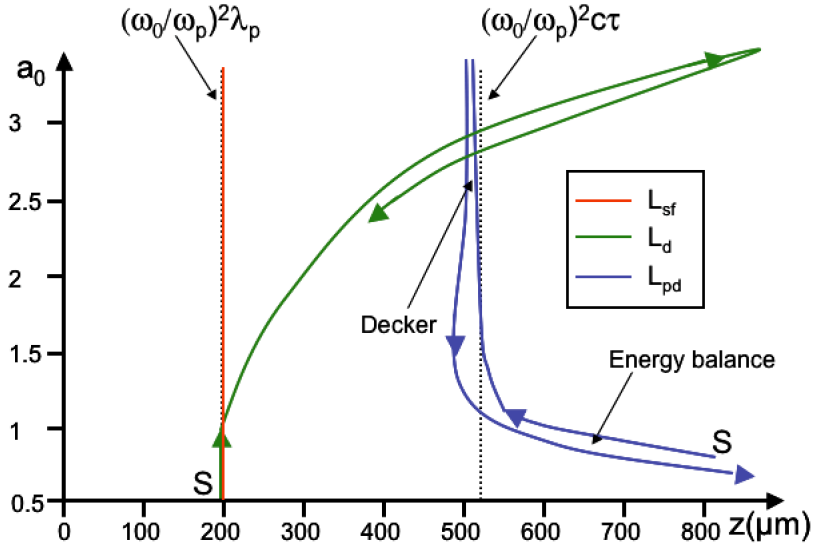

Figure 1.1: A schematic of the variation of the self-focusing length L_{sf}, dephasing length L_d and pump depletion length L_{pd} as the laser pulse self-focuses and depletes (a_0 increases and then drops) in a He plasma with a density of $n_p = 5 \times 10^{19} cm^{-3}$. Start with a 2TW Ti:Sapphire laser pulse with a duration of $\tau \sim 50$fs. "s" is the start point of the laser plasma interaction.

(from $a_0 < 1$ linear case to $a_0 > 1$ nonlinear case) at the beginning due to self-focusing and then drop back due to pump depletion, the dephasing length will increase from $\sim 200\mu$m to $\sim 800\mu$m as a_0^2 increases, and again decreases back as a_0 decreases.

C: Pump depletion length

Another importance length in LWFA is the pump depletion length L_{pd}. As the laser pulse propagates in the plasma, it loses energy to generate the plasma wave. The pump depletion length is the the distance it takes for the laser to lose most of its energy.

There are two approaches of estimating the pump depletion length. The first

one [56, 57] assumes the pump pulse loses all its energy to the plasma wave, hence $< E_z^2 > L_{pd} \simeq < E_L^2 > c\tau_L$, where E_z^2 is the average plasma wake field, E_L^2 is the laser field and $c\tau_L$ is the laser pulse length. From this approach, the pump depletion length is given as

$$L_{pd} \simeq \left(\omega_0^2/\omega_p^2\right) \begin{cases} \frac{c\tau}{a_0^2}, & \text{for } a_0^2 \ll 1 \\ \frac{c\tau}{3\pi}, & \text{for } a_0^2 \gg 1, \end{cases} \tag{1.8}$$

Another approach developed by Decker et al [50], assumes that the energy loss of the laser pulse is dominated by the loss in the front for $a_0 > 1$. Using a 1D nonlinear model, the etching speed of the laser was estimated as $v_{etch} \simeq c\omega_p^2/\omega_0^2$. Therefore the pump depletion length can be calculated as

$$L_{pd} \simeq c\frac{c\tau_L}{v_{etch}} \simeq \frac{\omega_0^2}{\omega_p^2} W_0 \tag{1.9}$$

where it is assumed that $W_0 \simeq c\tau_L$ is the laser spot size. This type of pump depletion (etching of the laser energy from the front) is applicable to the blowout regime. Knowing that in blowout regime, $k_p W_0 = 2\sqrt{a_0}$ [58], therefore,

$$L_{pd} \simeq \frac{\omega_0^2}{\omega_p^2} \frac{2\sqrt{2a_0}}{k_p} \tag{1.10}$$

For the parameters $a_0 = 0.8$ ($P = 2TW$), $\lambda_0 = 0.8\mu$m, $\tau_L \simeq 50fs$, $n_p = 5 \times 10^{19} cm^{-3}$, the pump depletion length from the linear formula is $L_{pd} \simeq 815\mu$m. However, the laser pulse will self-focuses at the beginning, which will cause a_0 to increase. As the pump depletes, a_0 will drop again. We notice that the linear formula in Eq.1.8 and the nonlinear formula of Eq.1.10 gives continuous results. The nonlinear formula in Eq.1.8 gives a smaller value than Eq.1.10. Therefore in Fig.1.1, the pump depletion length was calculated using the linear formula for $a_0 < 1$ and Eq.1.10 for $a_0 > 1$. As shown in Fig.1.1, when $a_0 > 1$ the nonlinear regime, the pump depletion length is $\simeq 500\mu$m, while in the linear regime, it

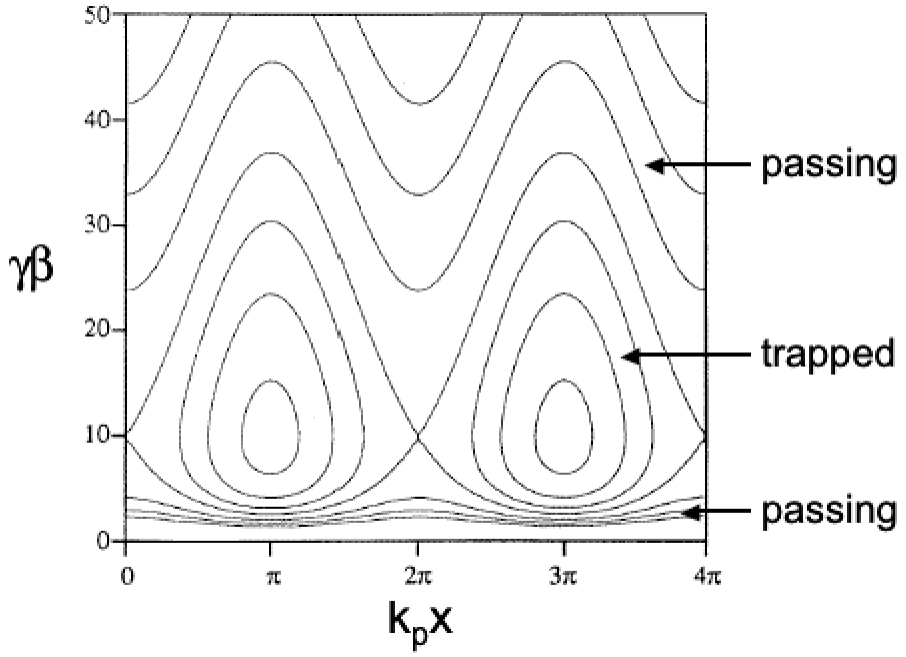

Figure 1.2: The separatrix in the wave frame for $\gamma_p = 10$ and $\delta n/n = 0.05$.

inversely proportional to a_0^2. Therefore, as the laser self-focuses (a_0 increases from < 1 to > 1) and depletes in a plasma, the pump depletion length will drop quickly from a bigger number to $\omega_0^2/\omega_p^2 c\tau$ as a_0 approaches 1 and very slowly decrease afterwards before the laser length $c\tau$ gets smaller. When a_0 drops to 1 again due to the pump depletion, *Lpd* will increase again as a_0 drops all the way to zero.

D: Electron trapping threshold

Electron trapping threshold (ETT) is a relatively new term in LWFA. It is often interchangeably used with the well known term wave breaking limit in 1D plasma theory. Wave breaking limit by definition is the maximum electric field amplitude of a self-sustained wave that can be supported in a plasma. Wave "breaks" because of the occurrence of trajectory crossing and the subsequent breakdown of the fluid model. Fig.1.2 [59] shows the separatrix in the wave

frame for $\gamma_p = 10$ and $\delta n/n = 0.05$. The vertical axis is the relativistic factor $\gamma = \left(1 - (v/c)^2\right)^{-1/2}$ times $\beta = v/c$ with $\gamma_{max}\beta_{max}$ on the top of the separatrix and $\gamma_{min}\beta min$ on the bottom). The horizontal axis of the separatrix $k_p x$ is the phase of the electron relative to that of the plasma wave. Electrons can be considered either as trapped electrons with closed orbits or as passing electrons with open orbits shown in Fig.1.2. At wave breaking, $\gamma_{min} = \gamma_p$ and the minimum speed of electrons is v_{min} at the phase $(2k+1)\pi$, where k is an integer. Therefore all electrons will be trapped at the wave breaking limit, enough to load down the wave.

The nonrelativistic cold-plasma wave breaking field is given as $E_{cwb} = cm_e\omega_p/e$ by Dawson [60]. In relativistic case, the wave breaking field can be higher than E_0. The formula,

$$E_{w.b.,\gamma} = \sqrt{2}\left(\gamma_p - 1\right)^{1/2} E_{cwb}, \tag{1.11}$$

is given by Achiever and Polovin [61], using 1D nonlinear relativistic cold fluid equation. This value neglected the thermal effect of the electrons, which can lead to a reduction of the wave breaking field because of the thermal velocity spread of the electrons at higher temperature. Considering the this effect, the thermal wave breaking field is given by [62]

$$E_{th} = \left(m_e c^2/3T\right)^{1/4} f_{Th}\left(\gamma_p, T\right) E_{cwb} \tag{1.12}$$

where $f_{th}^2 = \ln 2\gamma_p^{1/2}\beta_{th}^{1/4}$ for $\gamma_p\beta_{th}^{1/2} \gg 1$ where $\beta_{th} = 3T/m_e c^2$. f_{th}^2 is a slowly varying function of γ_p and temperature T with an amplitude on the order of E_{cwb}.

The above expressions are all for 1D. In 3D, the fluid model can never be used due to the electron trajectory crossing, which always happens in 3D even with relatively small wave amplitude. Therefore, the concept of wave breaking although useful is no longer strictly valid. However, the electron or particle trapping threshold still exists because a non-evolving wake can grow in a driver's

frame until particle trapping occurs, as a result, the wave amplitude damps. The plasma wave has accelerating phase (backward electric field) and decelerating phase (forward electric field). The trapping condition is that the longitudinal velocity of the electrons is equal or greater than the phase velocity of the wake field before it leaves the accelerating phase. By calculating single electron motion in a plasma wake field, Lu (Wei Lu, UCLA) has given an expression for the electron trapping threshold in his dissertation,

$$\lambda + \delta\psi = \left(\frac{\gamma}{\gamma_p}\right)\frac{1}{\gamma_p}, \tag{1.13}$$

where $\gamma^2 = 1 + p_\perp^2 + p_z^2$, $p_\perp$ is the transverse momentum and p_z^2 is the longitudinal momentum of the electrons, $\delta\psi$ is the phase difference between the electron and the plasma wave. Here $\frac{\gamma}{\gamma_p} = \sqrt{\frac{1-V_p^2}{1-V_z^2-V_\perp^2}}$. In 1D case, $V_\perp = 0$, therefore $\gamma = \gamma_p$ when $V_z = V_p$, which recovers the 1D trapping condition.

Although the above expressions for self-focusing length, dephasing length, pump depletion length and electron trapping threshold, are commonly used by most scientists, the electron trapping, dephasing and escaping processes are still not so clearly explained by the above discussions. Recent work has been trying to resolve the physical process of LWFA [63–65]. Chang et al [64] used a time- (or spatially) resolved tomography to study the electron self-injection and acceleration processes. They found the electrons in the mono-energetic bunch were injected at the same location and accelerated over approximately one dephasing length. Instead of losing energy afterwards as predicted in simulations, the electrons keep more or less the same energy as they propagate all the way through the plasma. It seems that the electrons "escaped" from the plasma wake field. Thomas et al [65] claim they measured the $\dot{\beta}$ radiation from the electrons as they were accelerated to relativistic energy. More detailed and complete measurements which have similar features had been done in our lab, details of which will be dis-

cussed in Chapter A. The strong broadband infrared radiation only comes from one location (very short distance compared with the interaction length). However this observation as being due to the injection and violent sudden acceleration of electrons seems is hard to believe since the acceleration process seems to happen over a much longer distance in simulation. Therefore either the simulation is not mimicking the experiment or the interpretation for the radiation in this paper is wrong.

Above all, there are problems in the process of the electron acceleration in LWFA that haven't been understood by previous work. Trying to understand and solve these problem is exactly the goal of this thesis. By using four 50fs-time-resolved diagnostics, the refractometer, interferometer, Thomson scattering, side self-scattering, together with the forward Raman scattering, the electron spectrometer and surface barrier detecter on the interaction of a high intensity ultrashort laser beam with a few gas jets, the process of electron trapping, dephasing, pump depletion and electron escaping are carefully investigated. Better understanding of these process is achieved and discussed.

Chapter 2 of this thesis gives a brief introduction on the laser system, target chamber, the gas jets and the timing system that are used in the experiments. The 8 experimental diagnostics used in the experiments for both low density ($\sim 1.3 \times 10^{18}$ cm^{-3}) experiments and high density ($> 5 \times 10^{19}$ cm^{-3}) experiments are introduced one by one in Chapter 3. The experimental and simulation results of these diagnostics and the corresponding discussions are given in chapter 4, 5, 6, and A. Chapter 4 shows the results of forward scattering spectrum. A 400nm to $\sim 1.6\mu$m broad spectrum was measured the first time in the forward scattering diagnostic. Chapter 5 gives the results of the electron energy spectrum. A few tens of MeV electron beams with good collimation and low energy spread were

detected in the electron spectrometer. The results of the time resolved diagnostics are presented in chapter 6. The evolution of plasma wave front was measured with a resolution of $\sim 20\mu$m. This high resolution of the plasma wave front movement can give clues to the process of electron acceleration. The side scattering results are discussed and compared with the results shown in Thomas's paper [65] in Appendix A. The position and spectrum change with plasma density also helps us to understand the processes of electron acceleration and to help explain how the electrons escape the plasma. A summary of the thesis work is made in Chapter 7.

CHAPTER 2

Experimental facility and parameters

For the LWFA experiments discussed in this Thesis, the pump pulse that drives the relativistic plasma wave is provided by a Ti:Sapphire laser system. This laser, to be described in Section2.1, also provides a synchronized optical probe pulse, which can be used to diagnose the laser-plasma interaction. Also, the laser oscillator, which produces a continuous pulse train at about 93Mhz is used as the master clock for the entire experiment. The timing system that is seeded by this clock will be discussed in Section2.3. The plasma that supports the LWFA experiment is produced by focusing the high-power laser pulse onto the edge of a gas jet. Ideally, the laser is focused onto a sharp interface between vacuum and gas with the gas density being an adjustable parameter. A vacuum chamber is therefore used to ensure that the laser propagates and focuses in a reasonably high vacuum. The vacuum-gas interface is produced by a pulsed gas jet located in the center of the vacuum chamber; i.e., the center of the target chamber. The target chamber and the various gas jets used are the subject of Section2.2.

2.1 The Laser System

The laser used in our experiments is a high power ($\sim$ 2TW) ultra-short ($\sim$ $50fs$) pulse duration Ti:Sapphire laser. It was built by Positive Light, Inc.. Fig.2.1 shows the components of the laser system and the parameters of the

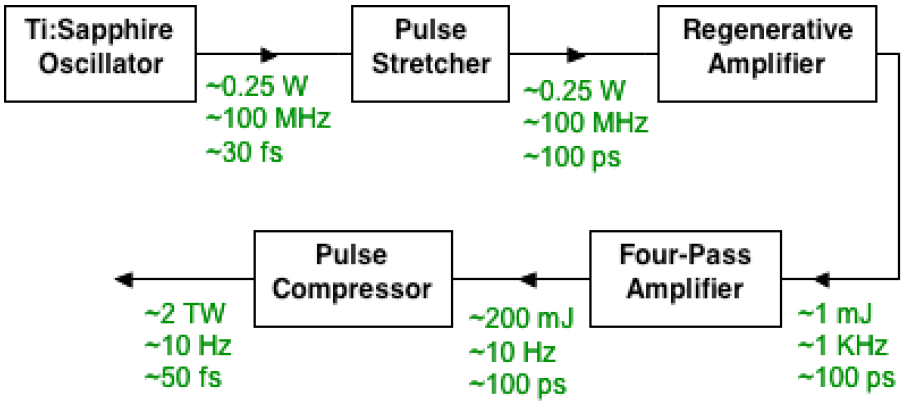

Figure 2.1: Diagram showing the parts of the laser system and the parameters of the laser pulses produced after each part.

laser pulses produced after each subsection of the system. It is a typical chirped pulse amplification (CPA) laser system that has following parts: the Ti:Sapphire oscillator, the pulse stretcher, the regenerative amplifier, the four-pass amplifier and the pulse compressor. Details of these parts will be provided in the following paragraphs.

2.1.1 Ti:Sapphire Oscillator

Fig.2.2 shows a schematic diagram of our Ti:Sapphire oscillator. The oscillator is pumped by a Millennia laser (Spectra Physics, Inc.), which is a 4W frequency doubled CW Nd:YAG laser. As shown in the figure, the pump beam is focused by a 10cm-focal-length lens (L1) onto the Ti:Sapphire crystal (C) and sent to a beam dump after it passes through the crystal. The oscillator cavity consists of one folding mirror (FM), a Ti:Sapphire crystal (C), two 5cm-focal-length spherical mirrors (SM1, SM2), three flat mirrors (M2, M3, M4), two prisms (P1, P2) and one output coupler (OC). The ends of the 10-mm-long Ti:Sapphire crystal are cut at the Brewster angle. The two prisms are used to compensate the group

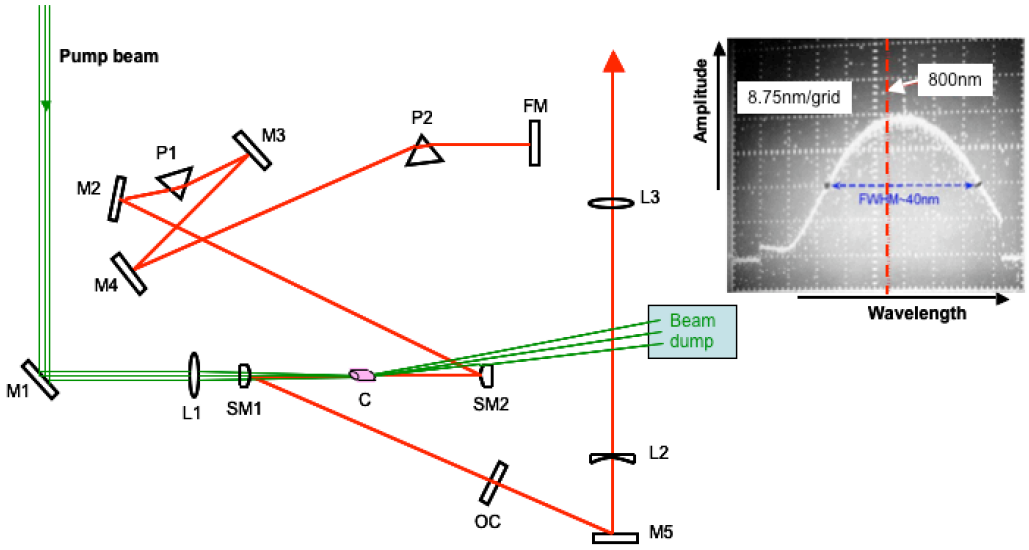

Figure 2.2: Schematic diagram of the Ti:Sapphire oscillator. The inset shows the spectrum of the laser out of the oscillator.

velocity dispersion (GVD) introduced by the crystal. The output coupler has a transmission of about 80%. This oscillator generates an 0.25W average power train of laser pulses with a repetition frequency of $\sim$ 93MHz. The pulse duration (τ_{osc}) is $\sim$ 30fs. The energy of each pulse (ε_{osc}) is $\sim$ 1nJ. The laser spectrum is measured with a spectrometer and displayed on an oscilloscope. The inset in Fig.2.2 shows a picture of the oscillator spectrum. The horizontal axis is the wavelength and the vertical axis is the amplitude. The wavelength axis is calibrated with a Neon lamp. The calibration for it is 6.7nm/grid and 800nm is at the red dotted line. The area under the spectrum is proportional to the average power of the oscillator. The FWHM of the spectrum is $\sim$ 40nm as shown in the picture. The resulting time-bandwidth product is $\tau_{osc}\triangle\nu_{osc} \simeq 0.56$, corresponding to a frequency spread of $\triangle\nu_{osc} \simeq 1.875 \times 10^{13}$. Hence the laser pulse is roughly bandwidth limited.

2.1.2 Pulse stretcher

The p-polarized laser pulses coming out of the oscillator remain p-polarized after going through a periscope (PS1) and a Faraday isolator, shown in Fig.2.3a. The Faraday isolator, including one polarizer (PI), one Faraday rotator (FR) and one quarter wave plate ($\lambda/4$), is used to prevent any back reflected light from going back to the oscillator. Before being amplified, the laser pulses need to be stretched to lower the intensity to avoid damaging the optics as well to minimize distortion to the spatial and temporal profile of the laser beam after it gets amplified. The stretcher consists of one pair of retro mirrors (RM), one grating (G), one rectangle folding mirror (FM), and one 4" diameter spherical mirror(SM), as shown in Fig.2.3a. It can be viewed as a lens-based stretcher, shown in Fig.2.3b, with two gratings (G1, G2, 1200 line per mm (lpm)), two lenses (L1, L2) and one folding mirror (FM1) if our stretcher is unfolded from the rectangular folding mirror (FM) and considering this mirror is at the dotted line in Fig.2.3b and the folding mirror in Fig.2.3b functions as the retro mirror in Fig.2.3a. The red, green and blue colors used here represent the red side, center and blue side of the laser spectrum, respectively. The distance $g - f$ in Fig.2.3 is the effective grating separation, where g is the distance from the lens to the grating, and f is the focal length of the lens. It can be easily seen from the diagram that if $g = f$, the focus is right on G2, thus there is no dispersion in the output beam. However when $g \neq f$, the focus will be either $2(g - f)$ before or after G2. The total dispersion depends on this factor $2(g - f)$, which is proportional to the stretching factor, the stretcher pulse length τ_{str} divided by τ_{osc}. When $g < f$, the pulses are positively chirped. We clearly see that the optical path length for the red is shorter than that for the blue. Hence the pulse leaving the stretcher will have a positive slope of frequency VS time; i.e., a positive chirp. In our stretcher

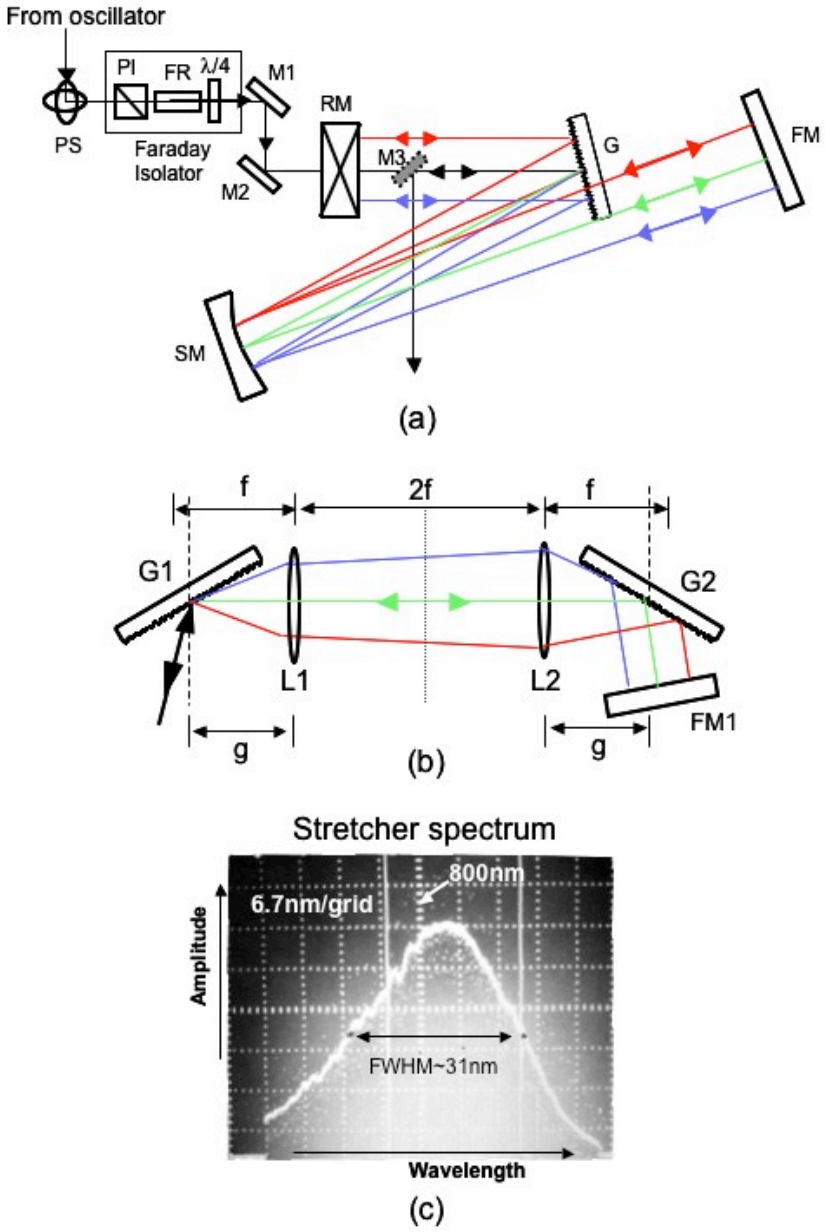

Figure 2.3: (a) Schematic diagram of the pulse stretcher; (b) Schematic diagram of a typical pulse stretcher; (c) The inset shows the spectrum of the laser after the stretcher.

(shown in Fig.2.2a), the focal length of the spherical mirror (f) is $36''$ and the distance between the grating and the spherical mirror (g) is $28''$. Therefore, our pulse is positively chirped upon leaving the stretcher. A spherical mirror is used in our case (instead of the two lenses shown in Fig.2.3b) to eliminate chromatic aberration and allow the holographic grating to be used near its most efficient Littrow angle of incidence, $\arcsin(\frac{\lambda}{2d})$, where $\lambda \sim 805$nm is the central wavelength and $d = \frac{1}{1200}$mm is the line separation of the grating. The dispersion can be expressed as [66]

$$\frac{\partial^2 \phi}{\partial \omega^2} = \frac{4\pi}{\lambda}\beta^2 \left(g - M^2 g\right), \tag{2.1}$$

where

$$\beta = \frac{\lambda^2}{2\pi c d \cos\theta_0}. \tag{2.2}$$

c is the speed of light, and $\theta_0 \sim 19^\circ$ is the emerging angle - the angle between the normal of the grating and the direction of the laser beam when leaving from the grating.

Therefore

$$.\frac{\partial t}{\partial \lambda} = -\frac{2\pi c}{\lambda^2}\frac{\partial^2 \phi}{\partial \omega^2} = -\frac{8\pi^2 c}{\lambda^3}\beta^2 \left(g + M^2 g\right) = 4.9\frac{ps}{nm} \tag{2.3}$$

The bandwidth of the laser spectrum after the stretcher is $\sim 31nm$, shown in Fig.2.3c. Hence, from eq.2.3, the laser duration τ_{str} is $4.9 \times 31 \simeq 152ps$.

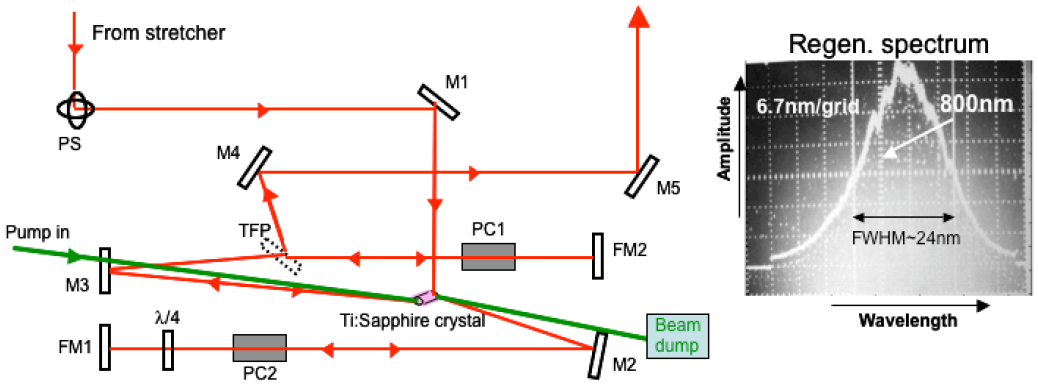

Figure 2.4: Schematic diagram the regenerative amplifier. The inset shows the spectrum of the laser out of the regenerative amplifier.

2.1.3 Regenerative Amplifier

After the stretcher, the laser pulse is first amplified with a regenerative amplifier - a Spitfire laser manufactured by Positive Light, Inc. The schematic diagram of the regenerative amplifier is shown in Fig.2.4. The cavity includes two folding mirrors (FM1, FM2), one thin film polarizer (TFP), two pockels cells (PC1, PC2), one quarter wave plate ($\lambda/4$) two flat mirrors (M2, M3) and one 5-mm-diameter and 10-mm-long Ti:Sapphire crystal. It is pumped by an Evolution laser, which is a 1KHz Q switched Nd:YAG frequency doubled green laser. Typical pump power is $\sim$ 8W. The incoming laser pulse from the stretcher is s-polarized after a periscope (PS), therefore it is first reflected from the crystal surface. With neither pockels cells turned on, double passing the quarter wave plate the first time will switch the laser polarization to p and trap the laser pulse in the cavity. However, in the second round trip, the quarter wave plate will switch the laser polarization back to s-polarized and the laser pulse will be reflected from the crystal. Therefore, to continue trapping the laser in the cavity, a pockels cell (PC2) needs to be turned on (by applying a quarter wave voltage) after the

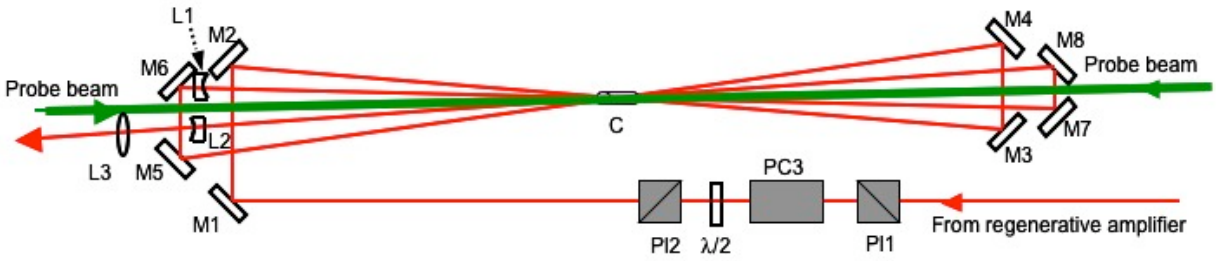

Figure 2.5: Schematic diagram of the four pass amplifier.

laser polarization is changed to p-polarized because double passing PC2 and the quarter wave plate will not change the laser polarization. After a few tens of round trips in the cavity, when the energy in the pulse has reached its maximum value, the laser pulse will be switched out by the thin film polarizer after PC1 turns on and rotates the polarization back to s-polarized. The bandwidth of the spectrum after the regenerative amplifier is $\sim 24nm$ as shown in the inset of Fig.2.4. The energy of the pulse is now about 1mJ, a gain of about 10^6 from the nJ oscillator level. PC1 and PC2 are triggered 1KHz to synchronize with the green pump, therefore the repetition frequency of the output laser pulse is 1 KHz.

2.1.4 Four-Pass Amplifier

After the regenerative amplifier, the pulse is further amplified by a four-pass amplifier, which is pumped by a Quanta-Ray laser (manufactured by Spectra Physics Inc.), a 10 Hz 1.5J Nd:YAG frequency doubled green laser. To synchronize with the pump, the 1KHz laser pulse out of the regenerative amplifier goes through a slicer before being amplified. The slicer includes two polarizers (Pl1, Pl2), one Pockels cell (PC3) and one half-wave plate ($\lambda/2$). As discussed in section2.1.3, the laser is s-polarized out of the regenerative amplifier. The pockels cell (PC3)

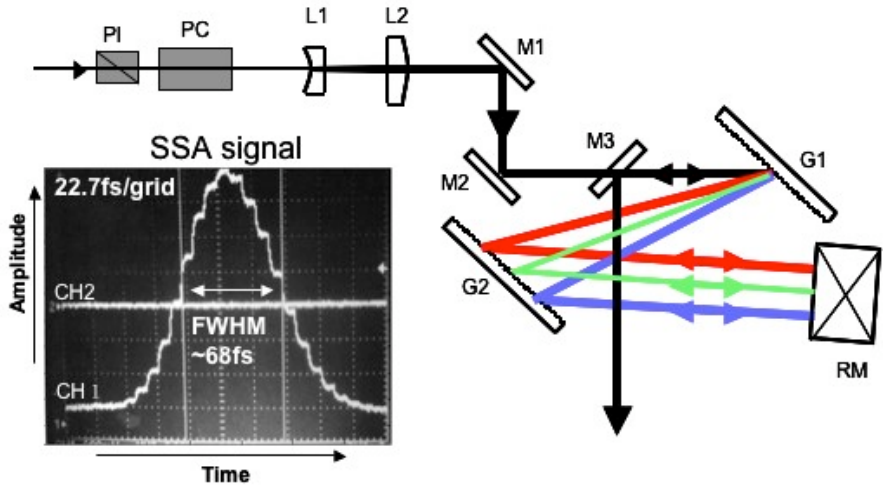

Figure 2.6: Schematic diagram of pulse compressor. The inset shows the single-shot-autocorrelator trace of the laser pulse after the compressor.

with a 10Hz trigger rotates polarization to p-polarized for ten out of each thousand laser pulses. Polarizer Pl2 only allows this laser pulse pass through, hence the repetition frequency will be 10Hz in the four-pass amplifier. The pockels cell (PC3) is also used to cut off the the prepulse and amplified spontaneous emission (ASE) leaking out of the regenerative amplifier. The amplifier system, as shown in Fig.2.5 is rather simple. It consists only 8 mirrors and one Ti:Sapphire crystal. The laser pulse passes through the Ti:Sapphire four times before it gets out. L1 is a 2m-focal-length length used to compensate for the thermal lensing from the Ti:Sapphire crystal. L2 and L3 are used to expand and collimate the beam out of the amplifier. The energy of the pulse after the four-pass amplifier is $\sim 200mJ$.

2.1.5 Pulse Compressor

Before the compressor, there is a polarizer and a PC, working as an isolator to protect the Ti:Sapphire crystal from being damaged by potential back reflected

light from the target. The compressor is basically to cancel all the dispersion created in the stretcher and in the optical path after the stretcher. Fig.2.6 illustrates how negative dispersion is created to compensate the positive dispersion discussed in subsection2.1.2. Clearly the optical path length for the red is longer here than that for the blue. Hence the pulse leaving the compressor will have a negative slope of frequency VS time; i.e., a negative chirp. The laser pulse length after the compressor (τ_{com}) is measured to be $\sim 48fs$ ($68fs/\sqrt{2}$) by a single short auto-correlater, as shown in the inset of Fig.2.6. The bandwidth of the spectrum is the same as that out of the regenerative amplifier, which is 24nm. The resulting time-bandwidth product is $\tau_{com}\triangle\nu_{com} \simeq 0.54$, corresponding to a frequency spread of $\triangle\nu_{com} \simeq 1.125 \times 10^{13}$. Therefore the laser pulse is approximately bandwidth limited. The transmission efficiency of the compressor is about 65%. The loss at other places after four pass amplifiers is about 10%. This gives a total loss of about 55%. Therefore the energy of laser energy on target is $\sim$ 110mJ and the power is $\sim$ 2 TW.

2.1.6 Prepulse monitor

Besides the power and duration, the peak-to-background intensity ratio is another important parameter of the laser pulse for laser-plasma interaction. For example, for a laser beam with a focused intensity of $10^{18}Wcm^{-2}$ interacting with He gas, a minimum peak-to-background ratio of 1000 : 1 is required because the HeI ionization threshold is $\sim 10^{15}cm^{-2}$. A prepulse or pedestal with an intensity of greater than this number will interact (ionize) with the He gas before the main laser pulse, which will change the physics of laser-plasma interaction [67] because of hydrodynamic expansion of this plasma. For other kind of interactions, for example, those involving other gases or solid target, the required value of the

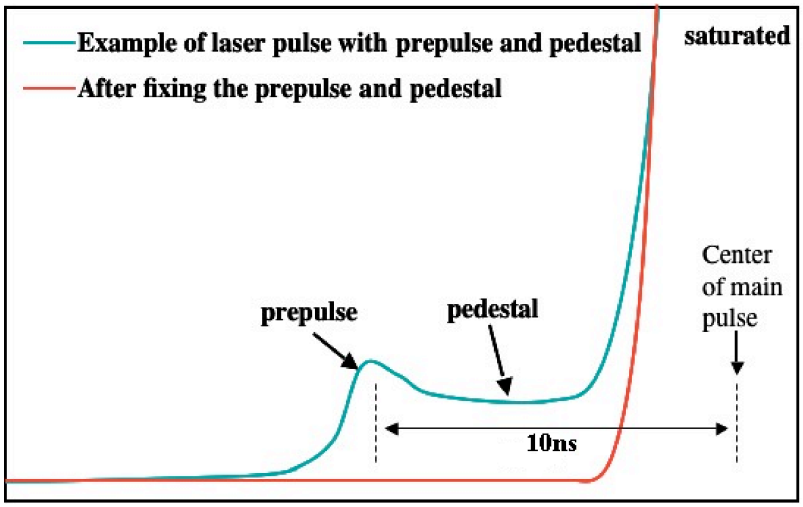

Figure 2.7: Schematic of the prepulse monitor signal. The green line shows the signal with both prepulse and pedestal before the main pulse. It's measures by a photodetector with a dynamic range of 1000 counts. The main pulse is intentionally made to be saturated on the scope so that the prepulse and pedestal can be seen clearly. The ratio of the peak-to-background intensity ratio of the main pulse is $\sim 1 : 50$. The red line shows the laser signal after fixing the prepulse and pedestal by adjusting the time of PC1 and PC2 in the regenerative amplifier and the slicer timing. By saturating the main pulse ~ 10 times, a signal background ratio of $\sim 10^4$ can be achieved.

peak-to-background intensity ratio may be even higher.

Therefore it is important to monitor and control the prepulse and pedestal of the laser pulse. The set up of the prepulse monitor is very simple. It uses only one fast photodetector to measure the signal leaking from the back of a mirror after the four-pass amplifier and an oscilloscope for the display. Both the prepulse and the pedestal come from the regenerative cavity when the timing of the two Pockels cells are not properly set. The proper timing for PC2 (for switching out the laser pulse) has to be right in the middle of two pulses. When it is too early, part of the previous pulse can leak out of the cavity and appear as the prepulse. The proper timing for PC1 (for trapping the seeded pulse into the cavity) is when the seeding is the best, which means that when the ASE reaches the minimum. The KHz pulse train after the regenerative amplifier cavity was detected by another photodetector and displayed on a oscilloscope. We adjust the timing of PC1 and PC2 while looking at the pulse train on the scope to see when PC2 turns on right in the middle of two pulse and when PC1 makes the ASE minimum. This will completely eliminate the prepulse and significantly reduce the pedestal. Slicer (before the four-pass amplifier) timing can be adjusted to further reduce the pedestal. Adjusting the slicer timing by looking at the scope of the prepulse monitor, we can put the slicer timing 0.5-1ns before the rising of the main pulse. The dynamic range of the photodetector used for the prepulse monitor is 1000 counts. However, by saturating the main pulse $\sim$10 times, a signal background ratio of $\sim 10^4$ can be achieved, as shown in Fig.2.7

One issue needs to be pointed out is that the rising time of the pockels cells is a few hundred pico-second and that of the photodetector is $\sim$1ns. Therefore, on the time scale, the best accuracy can be expected is $\sim$1ns.

2.2 The Target Chamber and Characterization of Gas Jets

As discussed earlier, the combination of a vacuum chamber and a pulsed gas jet provides a vacuum-gas interface that is the target for the focused laser beam. It is critical that this interface be as sharp as possible. As a general rule, we would like to have the transition region between vacuum and the full density of the jet to be $< Z_r$, the Raleigh length of the focused pump pulse. The reason for this is that we want the maximum possible laser intensity to couple to the LWFA. Without the vacuum, the laser could never be focused to the desired intensity due to a phenomenon called ionization-induced refraction [68]. Even with a relatively high vacuum surrounding the pulsed gas jet, experiments show that optimal coupling of the laser power to the LWFA requires fine-tuning of the gas-vacuum boundary relative to the vacuum focal-position (the location of the laser beam focus in the absence of any gas) on a scale of $< Z_r/2$. If the laser is focused, for example, one Z_r before the interface, the intensity on target will (by definition of Z_r) be 1/2 of the peak vacuum intensity. On the other hand, if the laser is focused, for example, one Z_r beyond the interface, the ionization-induced refraction mentioned above will prevent the laser from reaching the highest possible intensity within the gas. Clearly, if the interface is very sharp ($\ll Z_r$) then the full vacuum intensity can be coupled into the jet and used for the LWFA. The characterization of the gas jets used in these experiments will be discussed in Section2.2.2 and a description of the target chamber is given below.

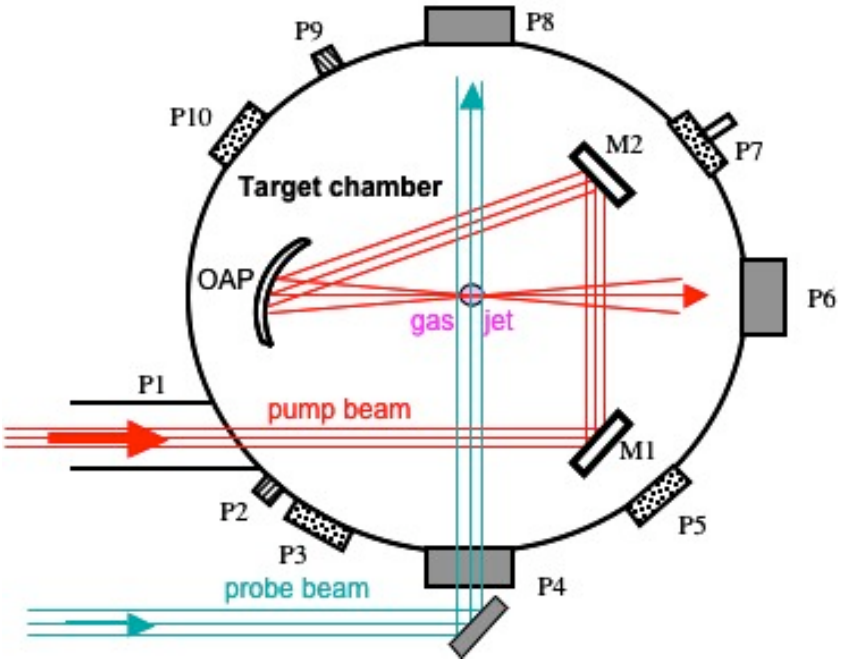

Figure 2.8: Schematic diagram of the target chamber. The compressed laser pulse enters through Port 1 (P1) and is focused with an off-axis parabolic mirror (OAP) onto the edge of the gas jet; i.e., the vacuum-gas interface.

Port	Size	Window	Used for
P1	4″	-	Entrance of pump beam
P4	4″	4″ laser window	Entrance of probe beam
P6	4″	4″ laser window	Forward diagnostics
P8	4″	4″ laser window	Side diagnostics
P3 and P5	3″	3″ glass window	Monitoring alignments
P7	3″	tube	Filling gas in the chamber
P10	3″	3″ laser window	diagnostics
P2 and P9	2″	-	Monitoring pressure

Table 2.1: Properties and functions of the target chamber ports

2.2.1 The target chamber

As discussed above, the main purpose of the target chamber is to provide a vacuum surrounding the gas jet target and allow for vacuum propagation between the grating compressor and the jet. Thus there must be many ports on this chamber to pass electrical, mechanical, and optical actions into and out of the chamber.

The chamber, as shown in Fig.2.8, has a diameter of $\sim 60cm$ and a height of $\sim 40cm$. It has twelve ports, ten of which, shown in Fig.2.8 are being used in the experiments. The properties and functions of these ten ports are listed in Table2.1. The target chamber is pumped by a turbo pump and a dry roughing pump. The vacuum pressure can be as low as $\sim 10^{-5}torr$. The pumping speed allows the high density gas jet ($10^{20}cm^{-3}$ helium density with a diameter of 1mm) to fire every 25 seconds with the chamber maintaining a vacuum better than 10^{-5}torr between shots.

2.2.2 Characterization of the gas jet

Gas jets, that can create desirable gas density profile and be completely open for all kind of diagnostics, are very useful for laser plasma interactions. As explained in the beginning of this section, the nonlinear laser plasma interaction study requires that the target gas has a sharp boundary ($< Z_r$) and a relatively flat profile between the boundaries. To satisfy this criterion, we followed the design that was first published by S. Semushin et al [69]. The design basically includes three parts, as shown in Fig.2.9: the gas jet nozzle, the neck and the poppet. There is a gas reservoir under the neck with a pressure called "the backing pressure". When the gas jet trigger is off, the poppet is pushed up against the neck by a spring so that the reservoir is sealed. When the trigger is on, the

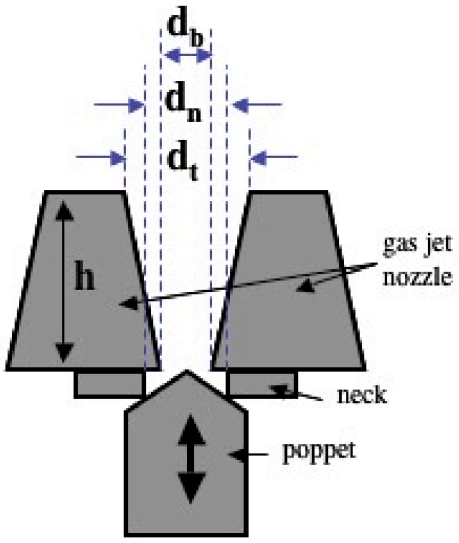

Figure 2.9: Schematic diagram of a typical gas jet shown in cross section.

poppet will be pulled down and release the gas stored in the reservoir which then flows supersonically through the nozzle and into the vacuum above. The design parameters of these three gas jets are listed in Table2.2. The only difference between them is the various dimensions of the gas jet nozzles, which determine the Mach number and therefore the gas density that the laser will encounter. d_t, and d_b are the top and bottom inner diameter of the gas jet nozzle, respectively. d_n is diameter of the neck and h is the depth of the nozzle.

The gas jet density is characterized with a Mach-Zehnder interferometer, as shown in Fig.2.10. using green-light ($\lambda = 0.632nm$) emitting Helium-Neon laser. Using He gas, a maximum of only 0.25 fringe shift was observed in HN1 jet with a backing pressure of 1400psi and no resolvable fringe shift was seen in either 2mm gas jets. To make a clear and accurate measurement, Ar gas ($\eta_{Ar} = 1.000281$), which has a much higher refraction index than He ($\eta_{He} = 1.000032426$), was therefore used to characterize the jets. However, there is still no measurable fringe shift in LN2 gas jet.

dimensions	LN2	HN2	HN1
d_t	2	2	1
d_b	0.5	1	0.5
d_n	0.8	0.8	0.8
h	5	6	4

Table 2.2: The dimensions of the gas jets. LN2: low density 2mm jet; HN2: high density 2mm jet; HN1: high density 1mm jet

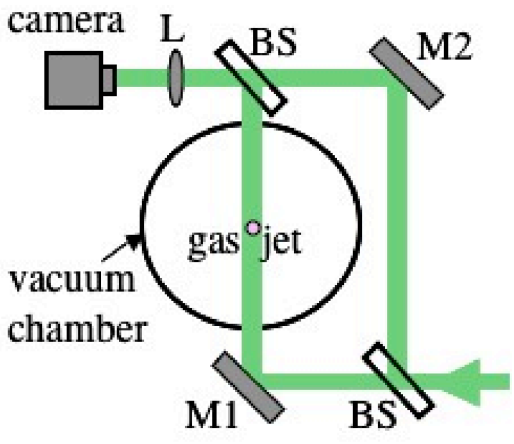

Figure 2.10: The Mach-Zehnder interferometer set up.

The density profile can be achieved by doing an Abel inversion [70] of the phase data fringe shift measured from Mach-Zehnder interferometer. The Ar density profile in HN1 and HN2 gas jets are shown in Fig.2.11a and Fig.2.11b respectively. Fig.2.11b shows that at a 1400 psi backing pressure, the density profile of the HN2 jet has the desired sharp boundary and a roughly flat-top density profile for heights $\sim< 1mm$ above the gas jet. Fig.2.11a shows that the density profile of the HN1 jet has good sharp boundary also, but only for heights $\sim< 0.5mm$ above the gas jet. Fig.2.12a shows that both the Ar density and the He density change with the backing pressure in HN1 gas jets. For both cases, the density increases with the backing pressure roughly linearly. The He density was found to be about 65% of the Ar density for the same backing pressure. Assuming this is a characteristic of the relative mass-flow rates of Ar and He gases, we suppose that this relationship can be applied to the HN2 gas jet to obtain the He density by multiplying the Ar density by 65%. The results are shown in Fig.2.12b for the HN2 jet.

2.3 The Timing System

.

The whole timing system for the experiments comprises mainly of 4 Research Systems (SRS) trigger boxes, as shown in Fig.2.13, and one Quantum Composer trigger box (see Fig.2.13 SRS♯3). The timing setting, output setting and function of every channel on each Stanford box are clearly shown in this figure. The Quantum Composer, which has 4 channels and is very close the target chamber, is only used to trigger the gas jet and some cameras for the diagnostics.

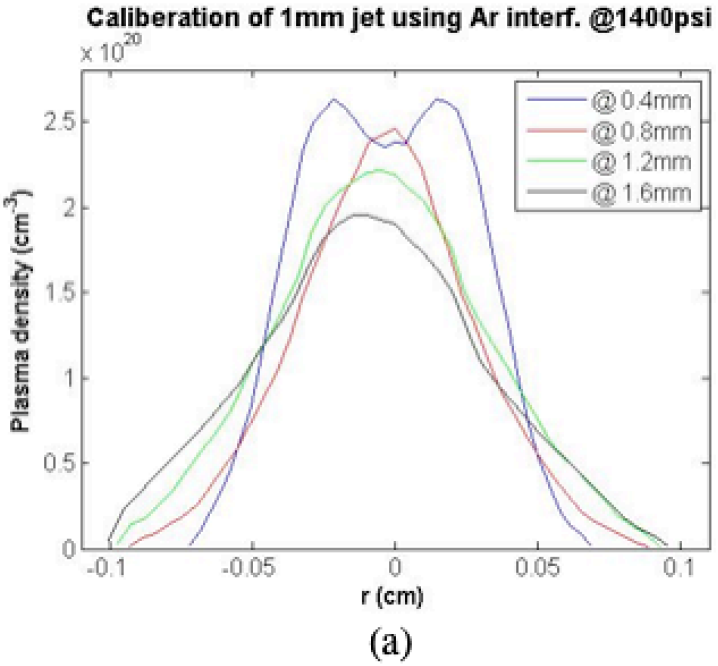

Figure 2.11: Characterization results of the neutral density of Ar gas jet. a) and b) show the Ar density at different height above the gas jet nozzle at 1400 psi for HN 1mm and HN 2mm gas jet respectively.

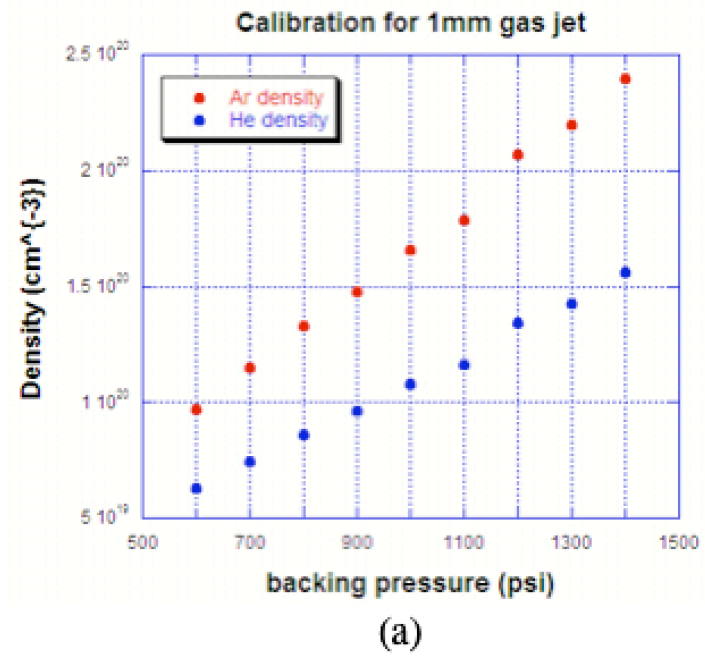

Figure 2.12: Characterization results of the neutral density of Ar gas jet. a) and b) show Ar density at different backing pressure at 0.5 mm above the gas jet nozzle for HN 1mm and 2mm gas jet respectively.

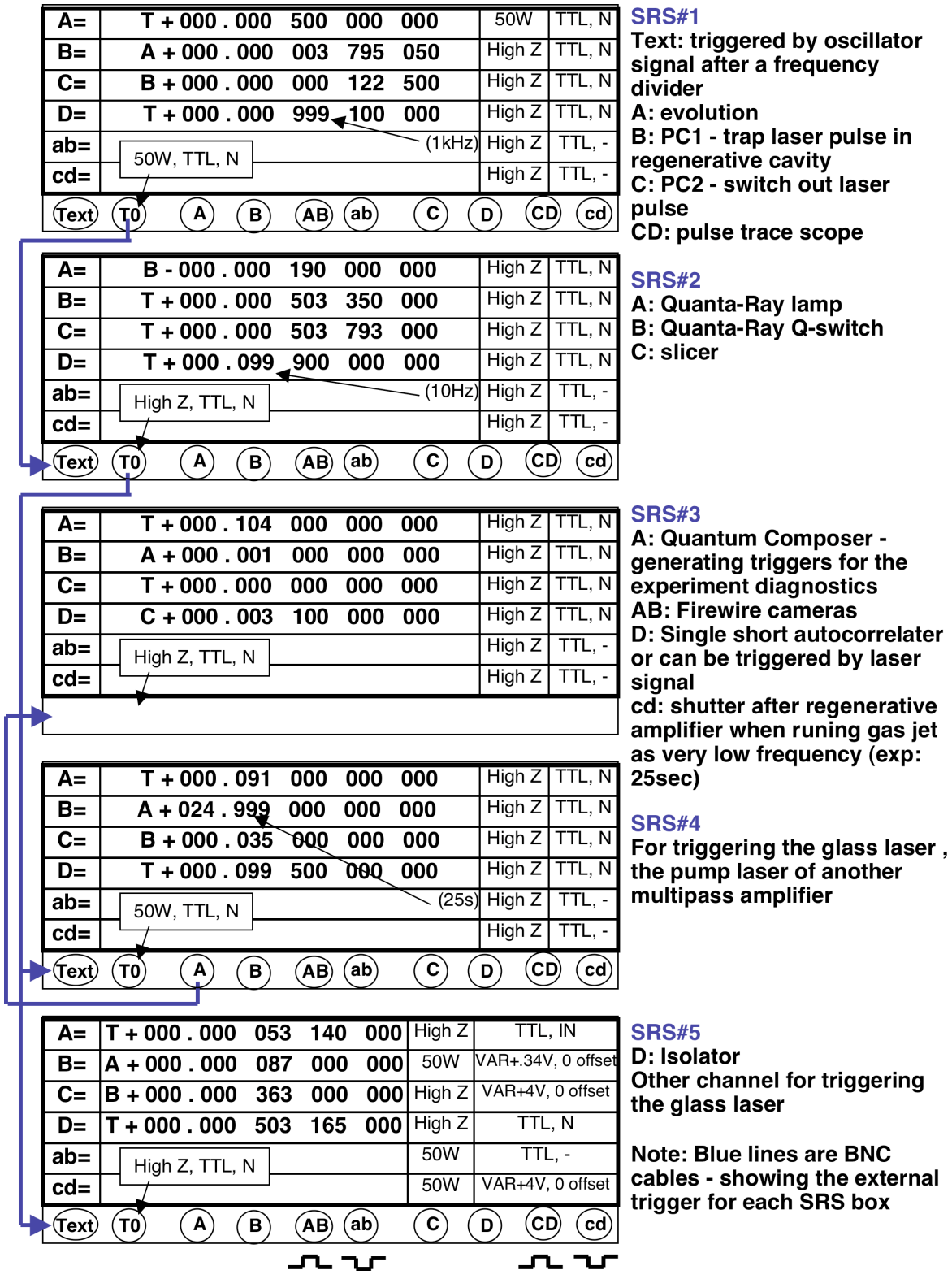

Figure 2.13: Diagram of the timing system for both laser and the experiment.

CHAPTER 3

Diagnostic techniques

In order to understand the physical process of LWFA, nine diagnostics are used in the experiments, with a maximum of six used simultaneously. The nine diagnostics, based on their location, can be separated into three categories: side view diagnostics, forward direction diagnostics, and a top view diagnostic. side view diagnostics includes time-resolved refractometer (TRR), time-resolved interferometer (TRI), time-resolved Thomson scattering (TRTS), side scattering spectrum (SSS), and time-resolved transmitted probe spectrum (TRTPS). forward direction diagnostics include forward scattering spectrum (FSS), electron energy spectrum (EES) and one surface barrier detecter (SBD). There is only one top view diagnostic, the top view image (TVI). To introduce each of these diagnostics in a convenient way, they will be separated into four groups: side view diagnostics for low density experiments, side view diagnostics for high density experiments, forward direction diagnostics and top view diagnostic. Each group will be discussed in one of the following sections. Low density experiments here refer to the experiments performed with the low density gas jet that was introduced in Chapter. In these experiments with the low density gas jet, the diagnostics show that there is no large amplitude plasma wave or accelerated electrons. Thus, the results of this experiment will be used as a reference for the high density experiment results. High density experiments are the experiments done with the two different high density gas jets, where diagnostics show a large

amplitude nonlinear plasma wave and electron acceleration are observed.

3.1 Side view diagnostics for low density experiments

Side view diagnostics for low density experiments include time resolved refractometer (TRR) and time-resolved interferometer (TRI). Other side view diagnostics as mentioned above were also tried in low density experiments, but without measurable signals. Time-resolved refractometer, although the set up is simple, is the most important diagnostic among all the diagnostics for both low density experiments and high density experiments. This is because at a certain probe time, it can tell the position of the pump laser with an accuracy of 20μm. It also gives information of plasma density from the phase modulation of the probe beam. Therefore by doing a probe time scan, we can tell if there is a prepulse in the pump beam and we also know the pump depletion length from it. For probe based diagnostics, TRR is also used to achieve the exact space and time overlap of the pump and probe beam and tell where another diagnostic signal, for example the Thomson scattering signal, comes from. Also for side-scattering spectrum, it can tell where the scattering signal comes from by removing the 800nm interference filter before the TRR camera. Details will be discussed in the following paragraphs.

3.1.1 Experimental set up of TRR and TRI

The set up of both TRR and TRI are shown in Fig.3.1. The 2 TW, Ti:Sapphire laser pulse with a length of 50fs, is split by a beam-splitter into two parts: 99% is reflected for the pump beam while the transmitted pulse is used as the probe beam. The pump beam is focused onto the gas-jet entrance with an off-axis

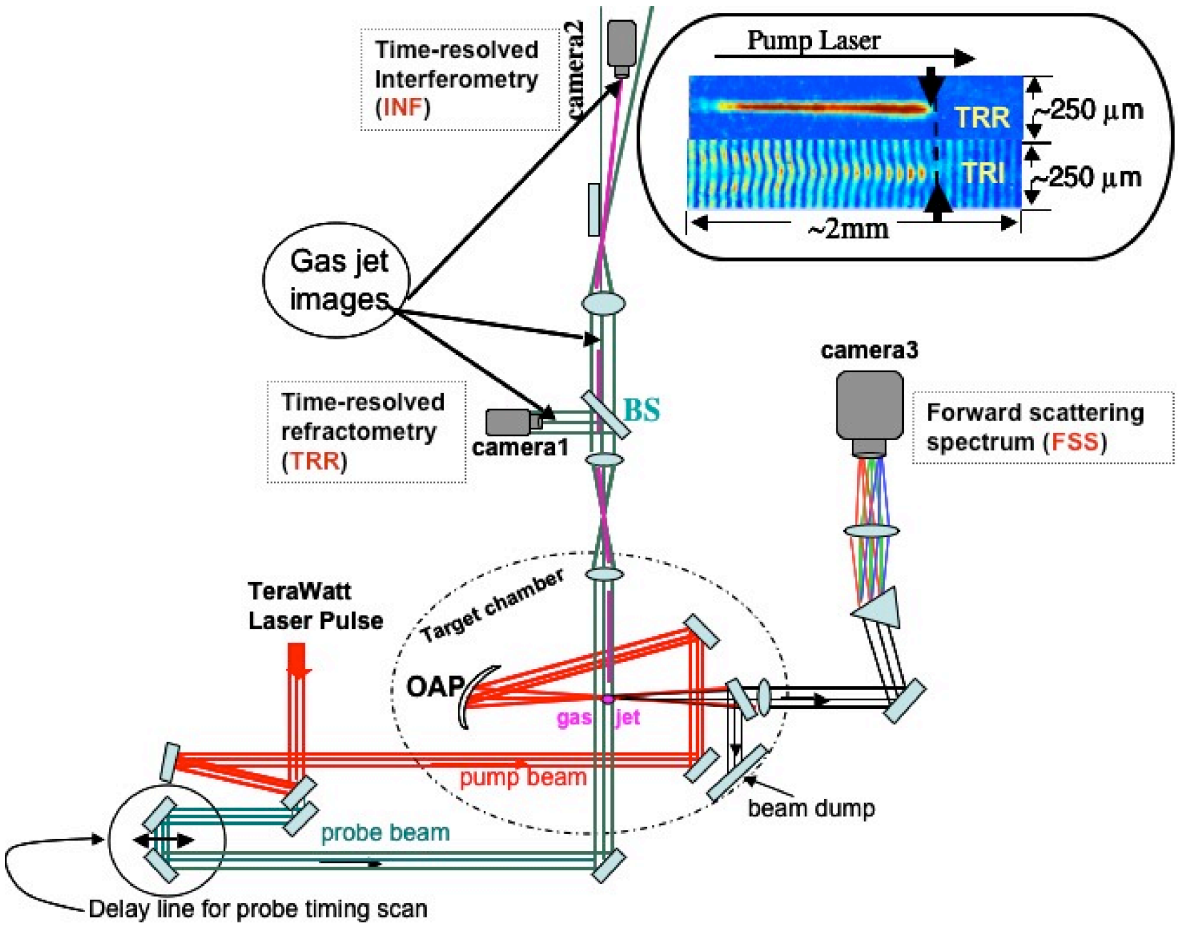

Figure 3.1: Schematic of the side view and forward direction diagnostics of the low density plasma. The two images shown are examples of the TRR (top) and TRI (bottom). The pump travels from left to right. The position of the fronts for these example images is about 1mm into the jet.

parabolic mirror (OAP) to a spot size 10μm. The probe beam, after an adjustable delay, is sent to the gas jet with an angle orthogonal to the pump beam. As shown in Fig.3.1, the two lenses downstream of the probe beam are used to image the gas-jet plane onto camera1 after reflection by a beamsplitter (BS). An 800nm/20nm interference filter is used on camera1 to see the image of the probe beam only at the gas jet. The refractive index of a plasma is $\eta \simeq 1 - \frac{n_e}{2n_{cr}}$, where n_e is the plasma electron density, $n_{cr} = \frac{\epsilon_0 m \omega_0^2}{e^2}$ is the critical density, and ω_0 is the laser frequency. Therefore, any on-axis depression in n_e acts as a cylindrical lens for the probe beam while the channel sheath acts as a negative lens. This is the time-resolved refractometry (TRR) diagnostic. On the transmission side of the BS, there is a short-focal length ($f = 5cm$) lens (located after the gas-jet image plane) to focus the probe beam to the front edge of a gold mirror as in a Lloyd-mirror interferometer [71]. This mirror reflects the "reference" beam (the part of the probe beam that does not go through gas jet) and overlaps it with the "scene" beam. This is the part that does go through the gas jet and contains information on the refractive index variation in the plasma (see heavy magenta lines in Fig.3.1). The image of the gas jet is reformed on camera2 within an interference pattern. This is the time-resolved interferometry (TRI) diagnostic.

3.1.2 Interpretation of TRR and TRI

The inset in Fig.3.1 shows one example each of TRR and TRI. The two pictures are scaled the same. Blocking the reference arm of TRI, the TRI image will look exactly like the TRR. TRR and TRI both give us the information about the plasma density. Comparing these two images together will help us to interpret TRR, which is a new diagnostic used in laser plasma physics. The spatial resolution of the TRR image is estimated to be 24μm; i.e., $\gg$ the laser spot size.

The well-defined, bright stripe comprising the TRR image is consistent with this view of the on-axis n_e depression acting as a focusing, cylindrical lens. This same on-axis enhancement of the probe beam intensity can also be seen in the TRI image. Here, the fringe spacing is about 65μm and the inferred peak n_e (after Abel inversion) is about $1.3 \times 10^{19} cm^{-3}$. Note that the fringes in the TRI suggest that the plasma formation occurs slightly ($\sim$ 50μm) ahead of the leading edge of the TRR image (see the two large black arrows in Fig.3.1). We believe that the well-defined leading edge seen in the TRR image is the "plasma wavefront"; that is, the perturbation to the refractive index due to the wakefield and transverse ponderomotive blowout, integrated over the transit time, convolved with the pulse length of the probe beam. On the other hand, the leading edge or first shifted fringe in the TRI occurs when the laser intensity exceeds the tunneling-ionization thresholds for He-I (He-II) at $10^{15} W/cm^2$ ($10^{16} W/cm^2$). Thus, this diagnostic measures the location of the ionization front. Note that this slight offset in the apparent longitudinal position of the plasma wave-front relative to the ionization front is consistent with ionization occurring before wake formation.

3.1.3 Linearity of pixels VS z position in TRR and TRI images

TRR and TRI are both time resolved diagnostics with an interaction length of $> 1mm$ in the longitudinal direction. To get reliable information for each time step, good linearity is required for the imaging system. However optical imaging frequently has deviation from rectilinear projection, which will cause distortion in the image. There are mainly two kind of distortions: barrel distortion, in which image magnification decreases with increasing distance from the optical axis and pincushion distortion, in which image magnification increases with increasing distance from the optical axis. Therefore, checking the linearity of TRR and TRI

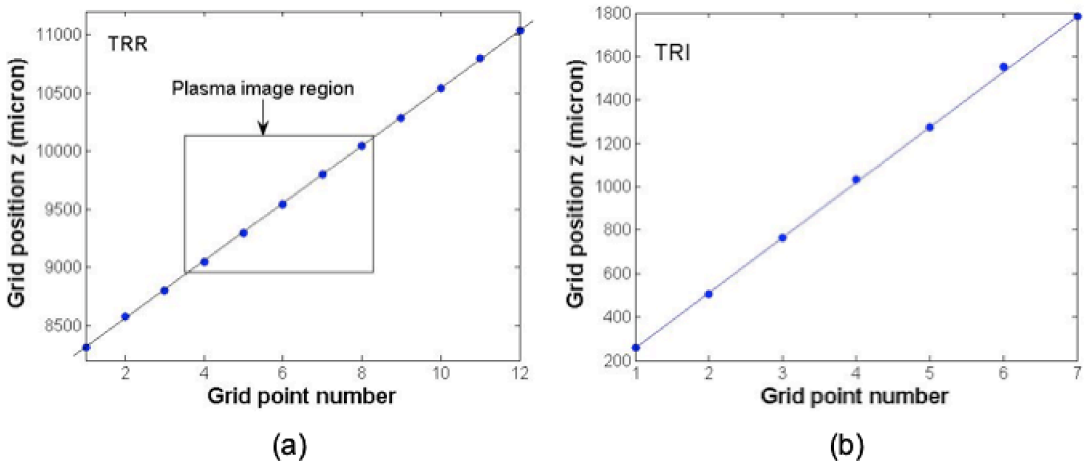

Figure 3.2: Calibration of the linearity of a) TRR and b) TRI images using 0.5mm grids.

images is important and necessary.

Fig.3.2 shows the calibration of TRR (Fig.3.2a) and TRI images (Fig.3.2b) of 0.5mm spaced grids at the same place where the plasma is. The data were taken from the center and the frame of each grid, therefore they are spaced by 250μm. In Fig.3.2a , the region within the square is where the plasma is located, which covers the total probe time scan ($\sim$ 1.5mm) for TRR diagnostic. It shows a deviation of $\sim$ 10μm within the region of plasma image. The line curls up a little bit with increasing distance, indicating that it has slight pincushion distortion. In Fig.3.2b, the probe time scan ($\sim$ 1.5mm) covers the whole width of the camera chip. It shows a maximum deviation of $\sim$ 15μm, which could be the error bar due to the limited resolution of TRI image. It is also hard to say what kind of distortion it has. Above all, the linearity is very good and will produce a negligible uncertainty effect on data interpretation.

TRTS, TRTPS and SSS diagnostics were also tried for the low density experiments, however there was no measurable signals from these diagnostics.

3.2 Side view diagnostics for high density experiments

The side view diagnostics of the high density experiments include TRR, TRTS, TRTPS and SSS as shown in Fig.3.3. TRI doesn't work in the high density experiment because the probe light that passes the area where the plasma density is high sees a very high refraction index gradient. This causes the probe beam to refract and thus miss the collective lens, thus forming discontinuous fringes. This makes it hard to quantify the fringe shifts.

3.2.1 Time-resolved refractometer and Thomson scattering

TRR is also an important diagnostic in high density experiments as discussed at the beginning of this chapter. The set up is a little bit different from the low density case because it shares the same incoming probe beam with TRTS, another important side diagnostic in high density experiment. The incoming divergence and angle of the probe beam is were changed to match the requirements for TRTS, but these changes do not effect the TRR very much. For Thomson scattering (TS) k-matching [72], the probe beam was set to an angle of 96° to the pump beam and was focused to overlap with the plasma with an elliptical spot of 50μm tall by 3mm wide. The calculated TS angle is 9° for scattering of the relativistic plasma wave at $5\times10^{19}cm^{-3}$. The Thomson scattered photons were collected with a lens, rotated 90°, and imaged onto the slit of a imaging-spectrograph. Note, at this high n_e, the temporal duration of the probe beam is long enough to overlap with $>$ 3 plasma periods allowing for "collective" scattering and the strong radial-component of the plasma wave allows for 3-D k-matching. An example of a TRTS spectrum is shown in the inset (upper right) to Fig.3.3. This typical TRTS spectrum is centered at about 700nm with a bandwidth of typically 40nm. The spatial resolution here is about 50μm. An example of a high-plasma-density

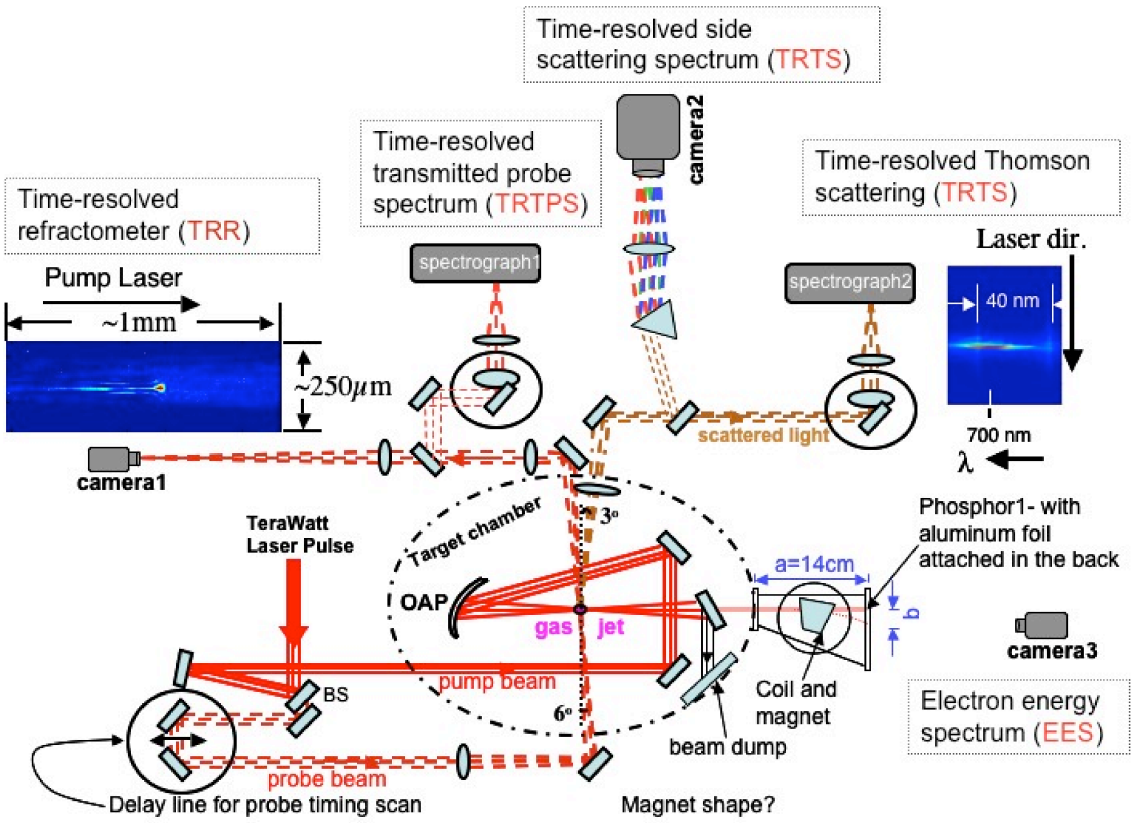

Figure 3.3: Schematic of the side view and forward direction diagnostics of the high density plasma. The two images shown are examples of the TRR (left) and TRTS (right). The pump travels from left to right for the TRR image, from top to bottom for the TRTS image. The position of the fronts for these example images is about 0.5mm into the jet.

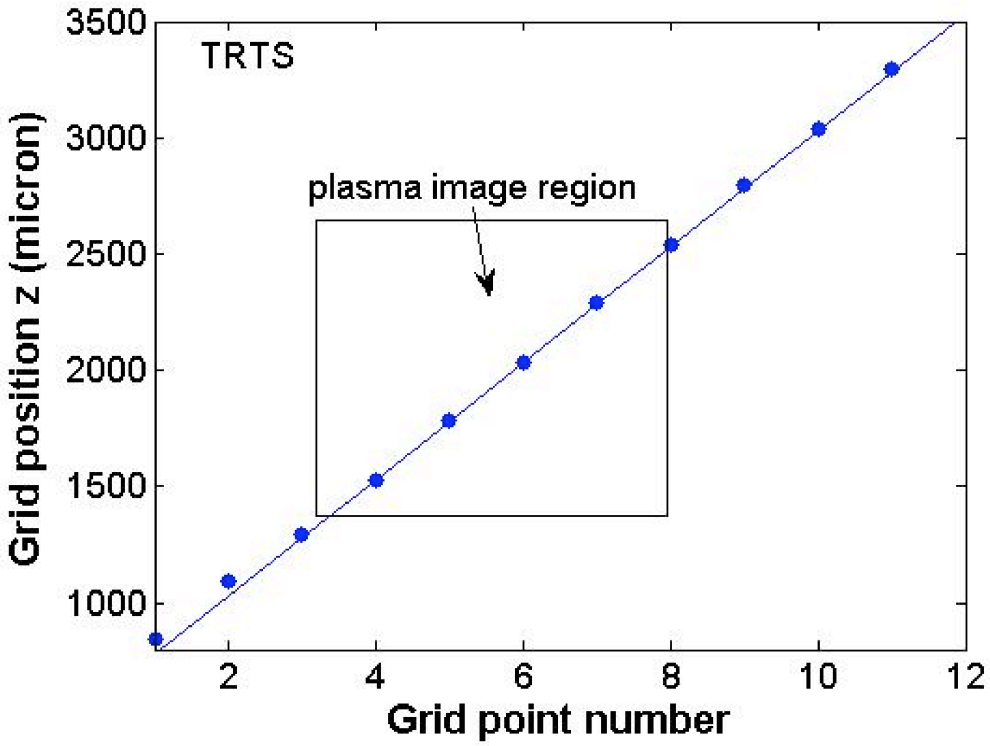

Figure 3.4: Calibration of the linearity of TRTS image using 0.5mm grids.

TRR image is also shown (upper left in Fig.3.3). Note the bright spot at the very front of this SDG image, which we believe is the first couple of "bubbles" in the plasma wave. The vertical size of this feature is probably resolution (24μm) limited.

3.2.2 Linearity of pixels VS z position in TRTS images

The linearity of TRR is the same as the low density case since the imaging system was not changed. Fig:3.4 shows the linearity of TRTS calibrated again with 0.5mm grids. Similar as in TRR case, it shows a pincushion distortion with a maximum deviation of 10μm within the plasma region, indicating a very good linearity.

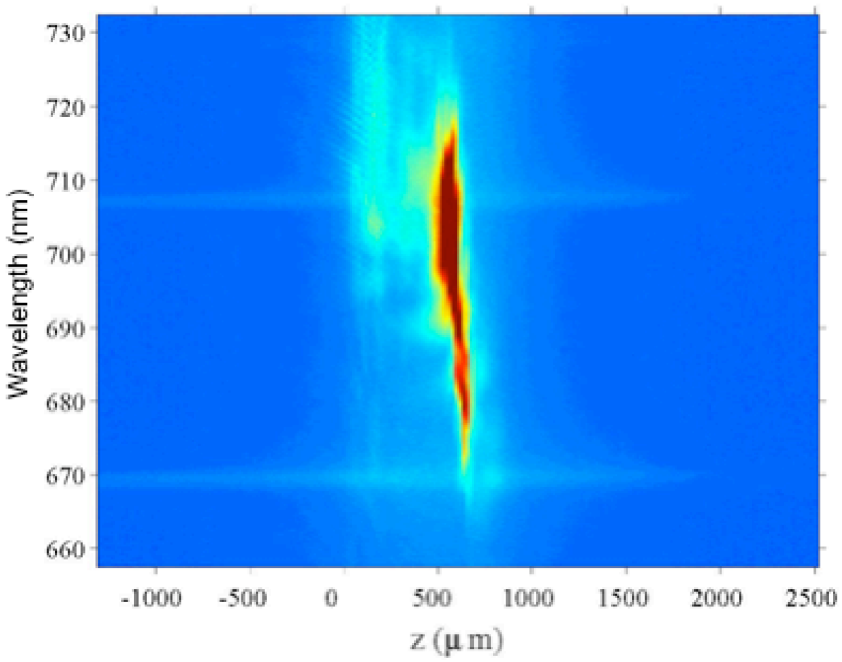

Figure 3.5: TS scattering spectrum for 2mm gas jet. Laser propagation direction is from left to right.

3.2.3 Spectrum of TS signal and k-matching angle of TS diagnostic

The TS diagnostic although called TS, is not the traditional TS, the scattering of electromagnetic radiation by a charged non-relativistic particle. In our experiments, the electrons are highly relativistic and the plasma wave is very non-linear, therefore the TS signal will not remain the same bandwidth as that of the original probe beam, instead, it will be broadened. Figure3.5 shows a typical spectrum of the TS signal. The two horizontal spectral lines are the two He lines; i.e., 707nm and 667nm. The continuum in the background is the plasma emission. The vertical bright line is the TS spectrum, which has a bandwidth of $\sim 35nm$. It is broader than the bandwidth $\sim 25nm$ of the probe beam. The wavelength shift from 810nm is $\sim 95nm - 130nm$. The real TS could be even

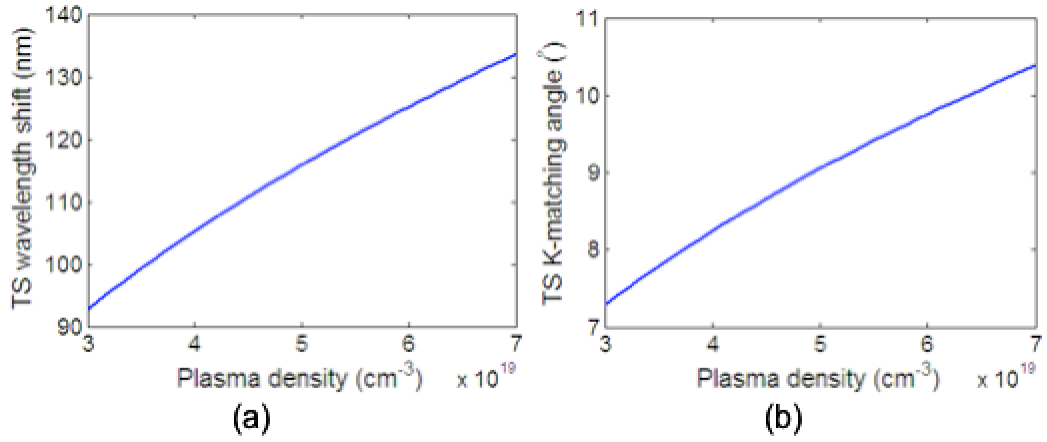

Figure 3.6: (a)TS scattering wavelength shift as a function of plasma density; (b) TS k-matching angle as a function of plasma density.

broader because this bandwidth is limited by the collection angle of the TS scattering set up. Figure3.6a and Fig.3.6b show the TS wavelength shift and the TS collection angle as a function of the plasma density respectively. The collecting lens for TS is a $2''$ lens 30cm focal length lens. The signal goes though a few $45°$ mirror and one periscope before it reaches the spectrometer. Therefore the real collection angle is only $\sim 3°$, corresponding to plasma density of from $\sim 3-7\times 10^{19}cm^{-3}$ as shown in Fig.3.6b. For this density range, the wave length shift is $\sim 95nm-130nm$ (see Fig.3.6b), which agrees with the experimental results (Fig.3.5). To prove this collection-angle-limited spectrum theory, a simple experiment was conducted. Different parts of the collection angle are blocked to see the response of the spectrum. Figure3.7 shows the results. The top picture shows when the half of the bigger collection angle is blocked, the red part of the wavelength shift disappears. The bottom picture shows when the half of the smaller collection angle is is blocked, the blue part of wavelength shift disappears. This agrees with Fig.3.6 and proves our theory.

This also explains that during a density scan, from $2\times 10^{19}cm^{-3}$ to $5.5\times$

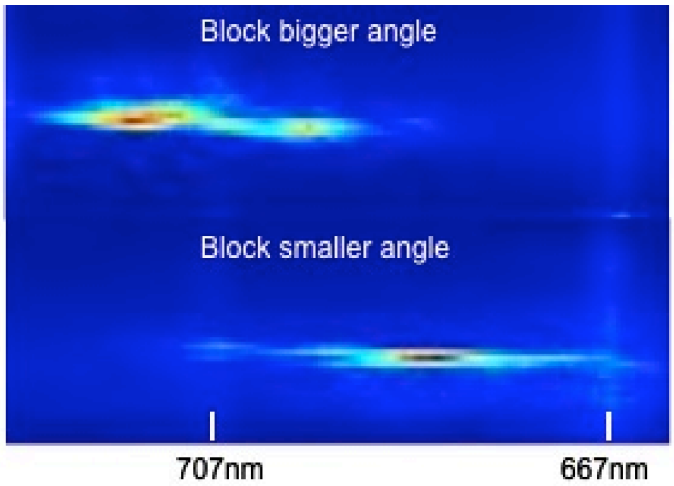

Figure 3.7: TS spectrum. Top: blocking half of the bigger collection angle; Bottom: blocking half of the smaller collection angle.

$10^{19} cm^{-3}$, only the amplitude of the TS signal gets stronger, the spectrum stays the same or only slightly more shift at higher density.

3.2.4 TRR as a prepulse monitor

An interesting thing found from a probe timing scan is that the TRR diagnostic can work as a prepulse monitor. Figure 3.8a shows an example TRR image of a shot with prepulse at the early time of a probe timing scan. The prepulse created a stripe, the front of which is marked by the letter "A". The main pulse behind the prepulse created a stripe with the front marked by the letter "B". This stripe is much brighter than that created by the prepulse because the intensity of the main pulse is much higher than the prepulse, as a result, the plasma channel created by the main pulse is much deeper than that created by the prepulse. A deeper plasma channel focuses the probe light stronger, in other words, the intensity of the focused light would appear stronger because the the image plane of the refractometry at where the plasma channel is. The prepulse is $\sim 1ns$

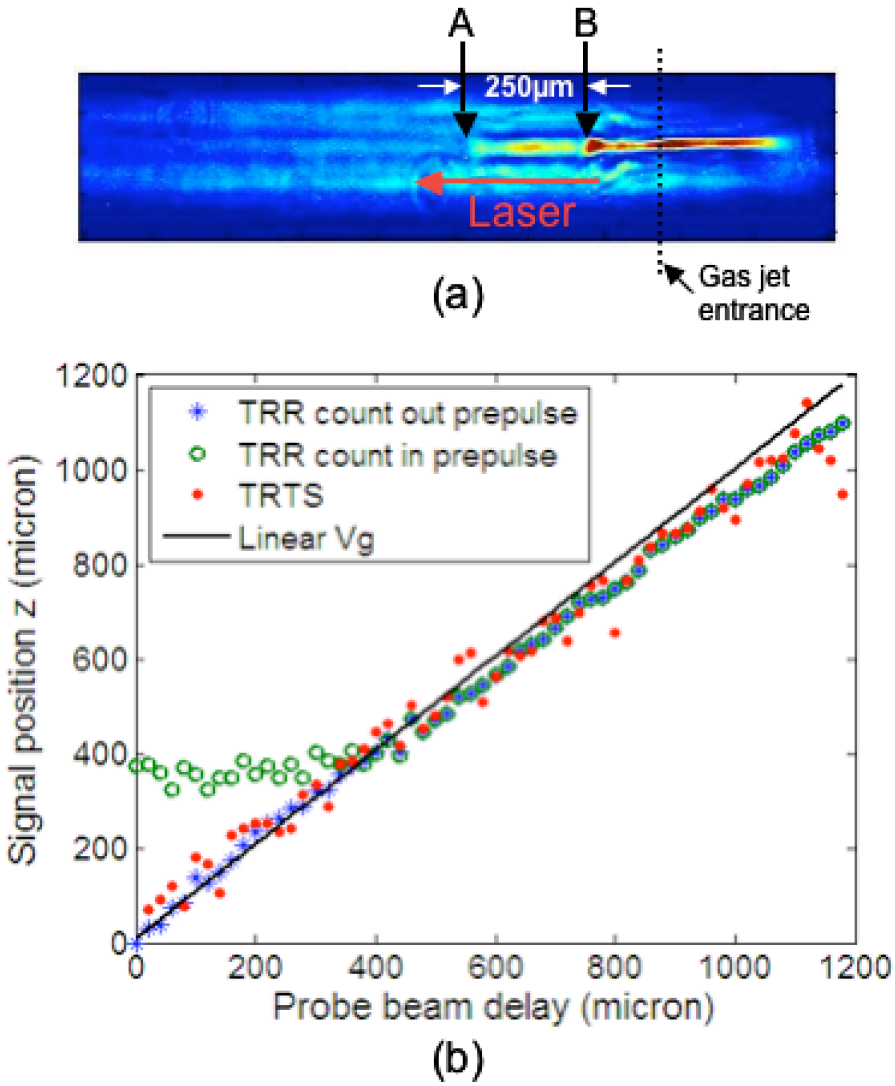

Figure 3.8: (a) A refractometry image of a shot with prepulse. "A" points to the front of the stripe created by the prepulse and "B" points to the stripe created by the main pulse. (b) The results of a probe timing scan of TRR and TRTS in a run with laser prepulse. TRR can work as a prepulse monitor here.

before the main pulse, hence it is already depleted when the main pulse arrives at the gas jet entrance. Therefore, during a probe timing scan, which usually starts when the main pulse is at the entrance of the gas jet, the stripes that the prepulse created will not move forward as the one created by the main pulse. Figure 3.8b shows the results of a probe timing scan with prepulse. The red dots are the plasma front from the TRTS signal and the black line is with a slope of the laser linear v_g at the plasma density. The blue star is the TRR signal if probing position "B", the front of the main pulse; the green circle is the TRR signal if probing the front of the overall stripe, which is "A". "A" stays constant and "B" is catching up at the beginning of the probe timing scan. After "B" passes "A", they move together together because now the front of the overall stripe becomes the front of the plasma created by the main pulse. These data show that we can probe the prepulse, and at the same time, we can count out the prepulse during a probe timing scan. Since the time resolution for a TRR is only $\sim 50fs$, as a prepulse monitor, TRR can detect a prepulse as close as a few hundred femtoseconds before the main pulse It is a very accurate, simple and direct. prepulse monitor so far. Looking at the refractometry image when there is a prepulse, we can adjust the timing of PC1 and PC2 in regenerative amplifier to get rid of the prepulse (see Chapter 3, Section 2.1.6).

3.2.5 Side scattering spectrum

Another side diagnostic is side scattering spectrum (SSS). It measures the spectrum of the side scattering signal of the pump beam from the plasma, therefore no probe beam is needed. It shares the collection lens and a mirror with the TRTS set up as shown in Fig.3.3. A beam splitter sends the side scattered signal to a 60° prism, which will disperse the signal and image different wavelength

signal to a different position on a MicronViewer 7290 camera, manufactured by Electrophysics. This camera has a good spectral response from 400nm to 2.2μm. The SSS signal is supposed to be very broad-band ($> 1\mu$m), which is the reason that a prism spectrometer is used instead of a grating spectrometer (which only measures a narrow spectrum, like a few hundred nm.) The side scattered signal is much stronger and broader than the TRTS signal and its location does not change with the probe beam, therefore, TRTS and SSS can be separated if they run simultaneously in one experiment.

3.2.6 Time-resolved transmitted probe spectrum

The time-resolved transmitted probe spectrum (TRTPS) is also measured in high density experiments. The set up is to simply stick a beam splitter in the beam going to TRR camera, rotate the beam 90° and image the center of the gas jet plasma to a imaging spectrometer slit. It measures the spectrum of the probe beam that transmitted through different longitudinal parts: the front, behind the front and the tail of the plasma. It is also time resolved, therefore it shows the spectrum change at each part of the plasma as the pump beam propagates forward.

3.3 Forward direction diagnostics

The forward direction diagnostics for both low and high density experiments are the forward scattering spectrum (FSS), SBD and the electron energy spectrum (EES), only that there were no measurable SBD and EES signals for low density experiments.

The FSS is also found to be very broad from the simulation results, therefore

a similar set up is used as that of the SSS diagnostic (shown in Fig.3.1). The pump beam, after propagating through the gas jet, 95% of the light is reflected by a 800nm broadband coated, $1/4''$ beam-splitter to reduce self-phase modulation of the transmitted laser beam as it goes through the lenses and vacuum window. The transmitted pump light is collected and sent through a prism and imaged by an imaging lens to a MircronViewer 7290 camera. A set-up like this to measure a spectrum range of almost 2μm has never been used before in laser plasma acceleration experiments.

The SBD is located at a small angle the forward direction so as not to block the electron and forward laser signals). It measures the X-Ray signal generated from accelerated electrons striking objects within the vacuum chamber (bremstrahlung radiation and provides a rough measure of the quantity or charge of accelerated electrons.

The set up of EES is shown in Fig.3.3. An deflecting electron spectrometer, which can measure electron energies up to 50MeV, is attached to the forward port of the target chamber. There is one coil and magnet both above and below the rectangular vacuum-extension box to produce vertical magnetic field across the waveguide. The pump beam was dumped by a gold coated mirror with a 0.8mm diameter hole in the center. The hole is for passing the electron beam, however some of the laser light will also leak through it. The leaking laser light will be further dumped by an aluminum foil attached in the back side of the phosphor used to visualize the electrons. The accelerated electrons escaping from the plasma will pass the magnetic field and be deflected along trajectories determined by the energy of the particular electron and the strength of the magnetic field and finally reach the phosphor at different energy-dependent positions. Camera3 images the deflection of the electrons on the phosphor. Knowing the magnetic field and the

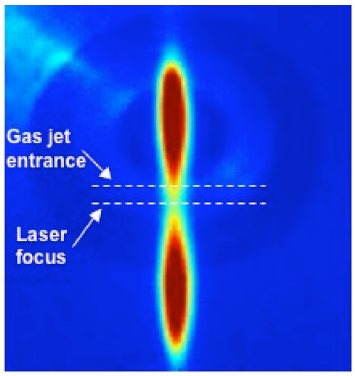

Figure 3.9: Top view image of the dumbbell plasma produced in a static fill and the position of gas jet.

deflection length b on the phosphor, the electron energy can be calculated as

$$\epsilon = \frac{B\,(KG)\,R\,(cm)}{3.33}\,(MeV)\,, \tag{3.1}$$

where $R = \frac{a^2+b^2}{2b}$ is the electron orbit radius, and a is the straight-line longitudinal projection of the electron trajectory as it leaves the plasma. The magnetic field depends on the current of the coil. A B vs I curve was measured independently which includes saturation effects in the magnetic circuit.

3.4 Top view diagnostics

The set up of TVI is simply one camera on top of the target chamber imaging the plasma and the gas jet. It is used for alignment purpose because it can see the gas jet and the "dumbbell" shaped plasma created by the pump pulse interacting with a low pressure ($<$ 10torr) static fill N_2 gas, as shown in Fig.3.9. We know that the middle of the dumbbell is where the laser focus is. Therefore the gas jet can be moved so that the entrance of the gas jet will overlap with the middle of the dumbbell, the laser focus, which is the best condition for laser and gas-jet plasma interaction. Due to the limitation of the resolution of the camera and the

uncertainty of the gas jet entrance, this is only to set the initial position of the gas jet. The final position will be fine tuned based on the electron signal as the gas jet is moved slightly about this initial condition.

3.5 Summary

This chapter introduced the set-up and important aspects of the mainly nine diagnostics used in the experiments. There is one top view diagnostics, TVI, used for alignment purpose for all experiments. Three forward direction diagnostics, SBD, EES and FSS were used to measure the accelerated electrons and the forward scattering spectrum. Four time-resolved side view diagnostics tell us the evolution of the velocity of the plasma wave-front, as well as the plasma density and some plasma wave amplitude information. The spectrum of TS signal has also been discussed. It has much broader bandwidth compared with the bandwidth of the probe beam due to the nonlinearity of the plasma wave. The measured spectrum on the spectrometer is limited by the k-matching angle. TRR can also be used as a new and simple method for measuring laser prepulse. The SSS is used for measuring the self-side scattering spectrum that may indicate the spatial location of the rapid electron acceleration and escaping processes. The set-up for all these diagnostics are very compact so that a maximum of 6 diagnostics can be used simultaneously, which helps us to understand the physics by correlating the data from different diagnostics. For SSS and FSS, a prism and a camera with broad band spectral response are used for measuring the spectrum of from 400nm to 2μm the first time in LWFA. The results of the FSS, SSS, EES and the time-resolved diagnostics will be discussed in later chapters.

CHAPTER 4

Forward scattering spectrum

The physics of nonlinear optics of plasma at relativistic intensities for short-pulse lasers has been studied both theoretically and experimentally [73–76]. There are two main plasma effects that modulate the spectrum of the laser pulse, which is measured in the forward scattering spectrum (FSS) diagnostic. The first is a parametric instability called Raman forward scattering (RFS): the decay of an incident electromagnetic wave of frequency ω_0 into a plasma wave of frequency ω_p and two forward propagating electromagnetic sidebands at the Stokes $(\omega_0 - n\omega_p)$ and anti-Stokes $(\omega_0 + n\omega_p)$ frequencies where n is a positive integer. The Stoke's and the anti-Stoke's waves beat with the pump so that the ponderomotive force of the beat-wave further enhances the plasma wave which in turn scatters more light providing a feedback loop for the instability. The other effect is relativistic self-phase modulation (SPM). It is well recognized that the index of refraction for a laser pulse that is copropagating with with a plasma density wave has a useful expansion expressed as

$$\eta = \left(1 - \frac{1}{2}\frac{\omega_p^2}{\omega_0^2}\left(1 + \frac{\delta n}{n} - \frac{\langle a_0^2\rangle}{2} - 2\frac{\delta\omega_0}{\omega_0}\right)\right), \tag{4.1}$$

where the last three terms take into account modulations in: the plasma density; the laser amplitude; and the laser frequency. As a result, the phase velocity $(v_\psi = c\eta^{-1})$ of the laser will be modulated by these factors. For the part of the laser traveling down a plasma density hill, the phase velocity of the front is smaller

than that in of the back, which causes the laser oscillation to "compress", and thus the laser frequency to increase. This is so called photon acceleration since this blue-shifting will ultimately result in an acceleration of the group velocity. Traveling up the plasma density hill will be the opposite; i.e., photon deceleration will occur. This modulation in frequency $\delta\omega \ll \omega_p$ causes the group velocity to vary periodically along the plasma wave and thus leads to longitudinal bunching of the laser intensity. This is how the relativistic SPM happens. Experimental evidence shows that RFS dominates in the FSS with relatively long ($\geq$ 0.5ps) laser pulse [73,77]. As the laser pulse gets shorter, SPM starts over weighing RFS and even dominates the FSS [73]. This is because the laser pulse length enters strongly into the growth of RFS, but the SPM growth can occur in relatively short pulses.

4.1 Gain ratio of RFS and SPM

In the short pulse regime the RFS instability has a spatial-temporal growth. Mori [45, 73] calculated the growth rates of RFS and SPM to be

$$g_{rfs} = \frac{a_0}{\sqrt{2}} \frac{\omega_p^2}{\omega_0} (\psi\tau)^{1/2} \tag{4.2}$$

and

$$g_{spm} = \frac{a_0^2}{8} \frac{\omega_p^2}{\omega_0} \tau \tag{4.3}$$

respectively, where ψ is the laser pulse length in time and τ is the interaction length of the laser with the plasma in time. In the presence of a very intense ($a_0 \gg 1$) laser, the plasma frequency $\omega_p \propto 1/a_0$, therefore as a_0 increases to certain value, the growth rate of RFS and SPM will drop [77]. The gain ratio of RFS and SPM can be calculated as

$$G_r = \frac{G_{rfs}}{G_{spm}} = \frac{e^{g_{spm}}/2\pi g_{spm}}{e^{g_{rfs}}/2\pi g_{rfs}} = \frac{g_{rfs}}{g_{smp}} e^{\frac{a_0\omega_p^2\tau^{1/2}}{\omega_0}\left(\frac{1}{sqrt2}\psi^{1/2} - \frac{a_0}{8}\tau^1/2\right)} \tag{4.4}$$

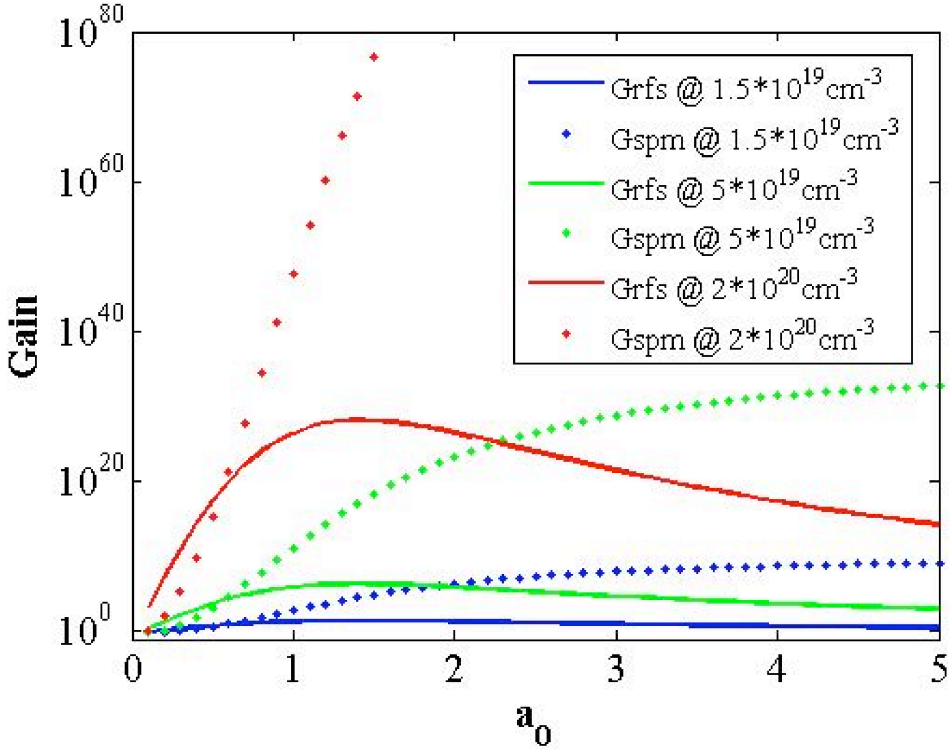

Figure 4.1: RFS and SPM gain as a function of a_0 at three plasma densities in the range of the experiment. Note that 750μm is used as the interaction length for density at $5 \times 10^{19} cm^{-3}$ and $2 \times 10^{20} cm^{-3}$ is , while 1.5mm is used for density at $1.5 \times 10^{19} cm^{-3}$.

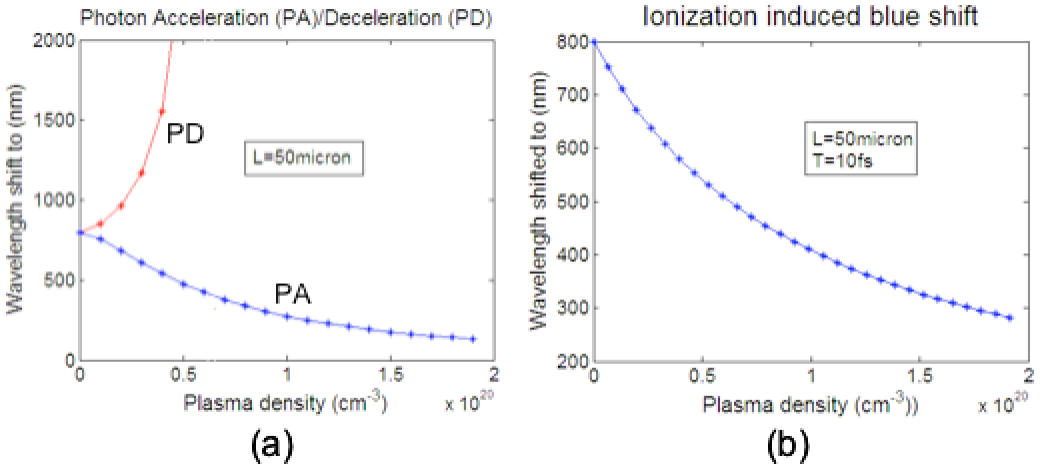

Figure 4.2: Frequency shift calculation a) from photon acceleration b) from ionization induced blue shift at different plasma densities.

For a 50 fs long laser pulse interacting with a plasma for $\geq 750\mu$m, as long as $a_0 > 0.5$, $G_r < 1$, and therefore SPM will dominate over RFS in the forward spectrum (see Fig.4.1). In our experiments, $a_0 \sim 1$ is used and self-focusing further increases a_0. We expect, therefore, that SPM will strongly dominate the FSS. For this same laser condition, the higher the plasma density, the stronger the SPM as shown in Fig.4.1. In the high density case, the SPM instability growth is a few order of magnitude larger than that in the low density case due to the self-focusing effect which increases a_0 in the former case. Calculation shows that this is true even the interaction length for the lower density case ($1.5 \times 10^{19} cm^{-3}$) is increase by a factor of 2 since measurement shows that the laser pump depletion length is about 2 times longer at $1.5 \times 10^{19} cm^{-3}$ than $5 \times 10^{19} cm^{-3}$.

4.2 Calculation of the frequency shift of photon acceleration and ionization induced blue shift

As discussed in the previous section, photon acceleration (including photon deceleration) occurs when the laser photons climb down or up the plasma density hill associated with a co-propagating electron plasma wave. The laser experiences a longitudinal variation of the index of refraction which it views as nearly stationary causing the frequency to undergo an up- or down-shift, spaced at λ_p. Assume the maximum density modulation is δn and the average plasma density is n_0, then index of refraction $\eta \simeq 1 \pm \frac{1}{2}\frac{\delta n}{n_c}\sin(\omega_p(t - z/v_p))$. Hence, the phase change after an interaction length of L is

$$\phi = k\int \eta dz = k\left(1 \pm \frac{1}{2}\frac{\delta n}{n_c}\sin(\omega_p(t - z/v_p))\right)L \tag{4.5}$$

Therefore the average frequency shift can be derived as

$$\langle \triangle\omega_{PA}\rangle = \frac{d\phi}{dt} = k\int \eta dz = \pm\omega_0\frac{\delta n}{n_c}\frac{\pi L}{\lambda_p}\langle\cos(ck_p t)\rangle \simeq \pm 0.018\omega_0\frac{L}{\lambda_p} \tag{4.6}$$

The last expression assumes $\delta n/n_0 = 0.5$

Laser frequency can also change in a relativistic ionization front [78] as the plasma density and thus the index of refraction, changes rapidly with time: $\eta = 1 - \frac{1}{2}\frac{n(t)}{n_c}$. Assume $n(t) = \frac{n}{T}t$ where T is the ionization time, thus the frequency blue shift in this ionization front (ionization induced blue shifts) is

$$d\omega_{IIB} = \omega_0\frac{n}{n_c}\frac{dt}{T} \tag{4.7}$$

Therefore the average frequency shift can be derived as

$$\triangle\omega_{IIB} = \omega_0\frac{n}{n_c}\frac{L}{cT} \tag{4.8}$$

Using the relation $\omega = 2\pi c/\lambda$, the shift of the wavelength can be easily derived for the above two cases. Fig.4.2a and b show the shifted wavelength as a function

of the plasma density for the PA and IIB, respectively, assuming the original center wavelength is 0.8μm, an interaction length of 50μm for both cases and an ionization time T of 5fs. Although both effect show a big frequency shift, there should be many more photons that experience PA than IIB for a laser pulse with a length equal or longer than the plasma wavelength because IIB only happen at the very front of the laser pulse (the ionization front) while PA happens over about half of the laser length.

The longitudinal distribution of photon acceleration and photon deceleration in a plasma wave can be calculated using Eq.4.6. Fig.4.3 shows the results of the calculation for $L = 50\mu$m. For Fig.4.3a, the horizontal axis is the time and the vertical axis is the amplitude of the laser electric field E_L. The curves have been offset for clarity. The plasma wave (red dashed curve) is taken to have a sinusoidal shape with $\delta n = 0.5$. The incoming laser (blue curve at the top) is initially transform-limited with a gaussian longitudinal profile. The green curve at the bottom shows the transmitted pulse after interacting with with the wave, according to Eq.4.6. We can see that going up the plasma-density hill causes a red shift of the laser frequency, as noted before. Note that the number of laser periods is conserved but the laser has now been modulated in phase or frequency (for a sinusoidal modulation, phase- and frequency-modulation are identical). The spacing of the transmitted laser periods gives the local laser wavelength. From the phase-modulation point of view, the derivative of this curve gives the instantaneous frequency. This instantaneous frequency vs. time has been converted to wavelength vs. time and plotted in Fig.4.3b along with the same plasma wave as in Fig.4.3a. For Fig.4.3b, the vertical axis is both the wavelength in microns for the laser spectrum (green) and the amplitude of the density modulation for the plasma wave (red dashed curve) respectively. We see that, for these parameters, after the laser interacts with the plasma wave , its

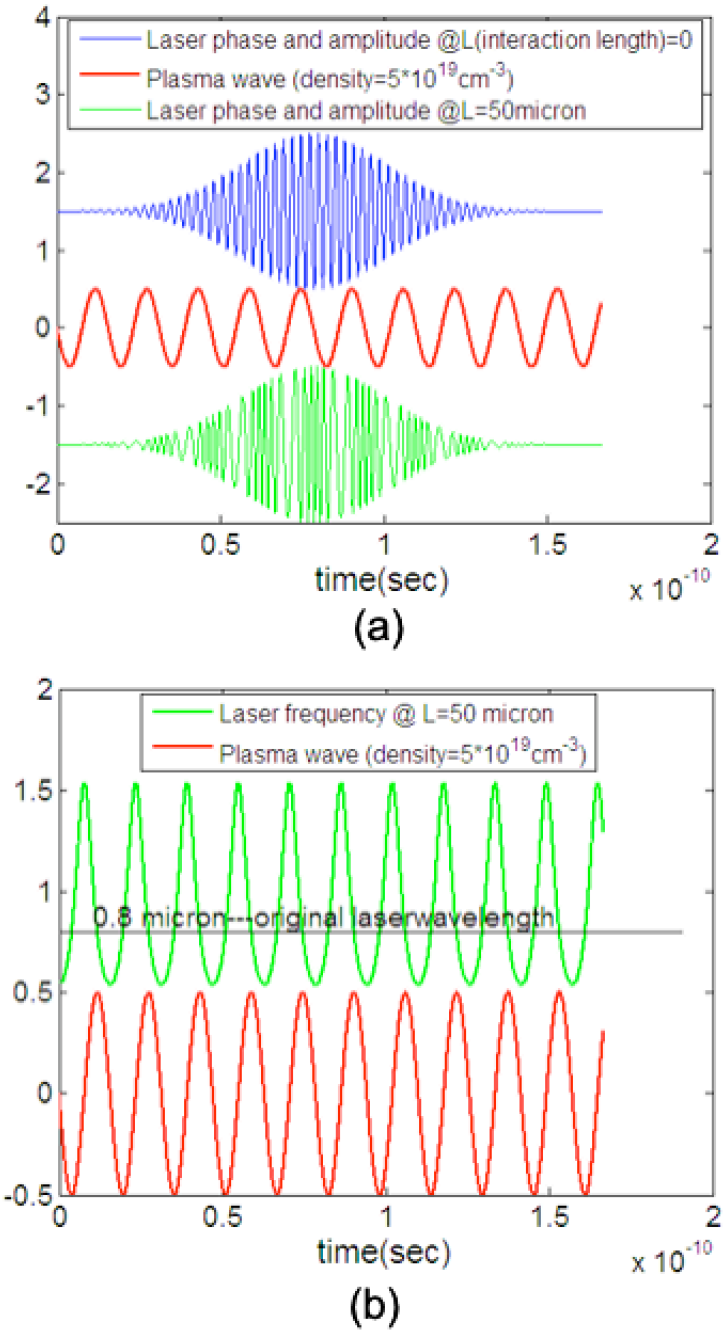

Figure 4.3: (a) Laser oscillation before (blue) and after (green) interacting with a plasma wave (red); (b) Laser frequency shift with respect to the plasma wave.

wavelength will blue shift to $\sim 0.5\mu$m and red shift to $\sim 1.5\mu$m. The wavelength shift is not symmetric. It tends to spike up for the red shift. If we consider the implications for real experiments where the plasma wave is driven by the laser pulse rather than a fixed initial condition, the frequency shift in the laser pulse can lead to an enhancement of the plasma wave. As we know, since $a_0 \propto E_L/\omega_0$, the red shifted light will have a higher a_0. Since the ponderomotive force driving the plasma wave $\propto \triangle\langle a_0^2\rangle$, the positive modulation of the plasma density can grow greater than n_0 and spike up, while the negative modulation will remain low and get broader in space. In other words, the red-shifted light is produced at the correct phase to enhance the wake. This can be taken as the "physical picture" for the SPM instability. Thus the red-shifted light may stay in phase with the wake and cause it to slow down as v_g becomes smaller. The blue-shifted light will not play much role since this will dephase rapidly from the wave due to group velocity dispersion.

4.3 Experimental and simulation results of FSS

The experimental set up for FSS was introduced in the previous chapter. The original set up used a grating spectrometer instead of the prism spectrometer shown in Fig.3.1. However, because the high dispersion of the gratings, the camera chip can only cover a wavelength range of $\sim$ 200nm. Therefore the grating spectrometer was only used for the FSS in the low density 2mm gas jet experiments, which had a spectral broadening of $\sim$ 100nm on both side of λ_0. This will not be discussed in detail since this dissertation focuses on the interaction of the laser pulse with high density plasmas.

The high density gas jet experiments, including the 2mm gas jet and the 1 mm gas jet, show a frequency up and down shift of $> \omega_0/2$; i.e., a wavelength

range of 400nm to 1.6μm. Traditional grating spectrometers can not cover such a broad range. Therefore a low dispersion spectrometer was built with a prism and the spectrum was recorded on a vidicon camera with good spectral response from 400nm to 2.2μm(Fig.3.1). Fig.4.4a shows the raw results of the forward spectrum obtained from the high density 2mm gas jet for various pressures. However, as introduced in Chapter3, section 3.3, the laser light went through a beam splitter (for dumping most of the laser light) which has a broadband 800nm coating. The transfer function of which is plotted as the purple curve in both Figure 4.4a and Figure 4.4b. Figure 4.4b shows the forward spectrum after applying the transfer function for various pressures. This was the first experiment to measure a FSS in such a broad range (from 2ω to $1/2\omega$) to our knowledge. The red side and blue side of the spectrum were taken on separate data sets so that the resolution of each side of the spectrum were better by a factor of two than taking the whole spectrum on one camera chip. The red and blue side of the spectrum were combined together at the wavelength of $\sim 1\mu$m. The two sides of the spectrum do not match perfectly because of the uneven background exposure on the camera. The periodic, but nonlinear plasma wave (discussed in section 4.2) indicates both a photon acceleration and a photon deceleration, in other words, blue shifted and red shifted signals. There would be extra blue shift induced from the ionization of the gas jet too. If we take the laser and plasma as one system, this system will obey energy conservation, in other words, the energy that the laser lose as a result of the photon deceleration is about the same energy of the plasma wave plus the energy of the accelerated electrons. Fig.4.4a shows that as the pressure and thus the plasma density increases, the amplitude of the blue shifted signal decreases and the red peak ($> 1\mu$m) moves towards longer wavelength (except at 700psi where a huge x-ray signal was detected from the SBD which indicates significantly increased electron acceleration). This is because as the plasma density increases,

both the plasma wave amplitude and the number of electrons that are likely to get accelerated will increase, hence the photon deceleration induced red shifted signal will increase. Since the photon number is conserved, therefore, the photon acceleration induced blue shifted signal will decrease. Fig.4.4b shows that after applying the transfer function to the raw spectrum, we lose most of the large red and blue shifted signal. All we can see is the spectrum broadening around λ_0, 810nm. This could be because there is more laser light that gets diffracted due to the non perfect Gaussian profile of the laser and refracted by the ionization of the plasma. For example, the light in the rings around the focal spot, which contains about $\sim 30\%$ of the total laser energy, will be diffracted away and not experience any photon acceleration or deceleration. The interferometry image in Fig.4.4c shows that the transverse size of the ionized plasma is about 150μm, while the refractometry image shows that the transverse size of the plasma wave is only about 30μm. Therefore the ionization induced refraction also increase the amplitude of the 810nm (center wavelength of the initial laser light) that is collected by the prism spectrometer. Therefore these photons around 810nm will saturate the camera and appears like a strong broadening of the 810nm laser light.

Simulation work is done for comparing with the experimental results of most of the diagnostics. It is a 3D OSIRIS simulation done in UCLA plasma simulation group by Wei Lu and Frank Tsung. A 2TW, 50fs laser pulse was launched with a focused spot size of 50μm to the edge of the $5 \times 10^{19} cm^{-3}$ uniform plasma. The results of FSS from both the simulation and experiment are shown in Fig.4.5 is the laser spectrum after it propagates $\sim$1.2mm (where the experimental diagnostic shows that the laser energy almost completely depletes, which will be discussed in later chapters) in a He plasma with a density of $5 \times 10^{19} cm^{-3}$. The deceleration signal (red shifted signal) from simulation seem to agree with that from the

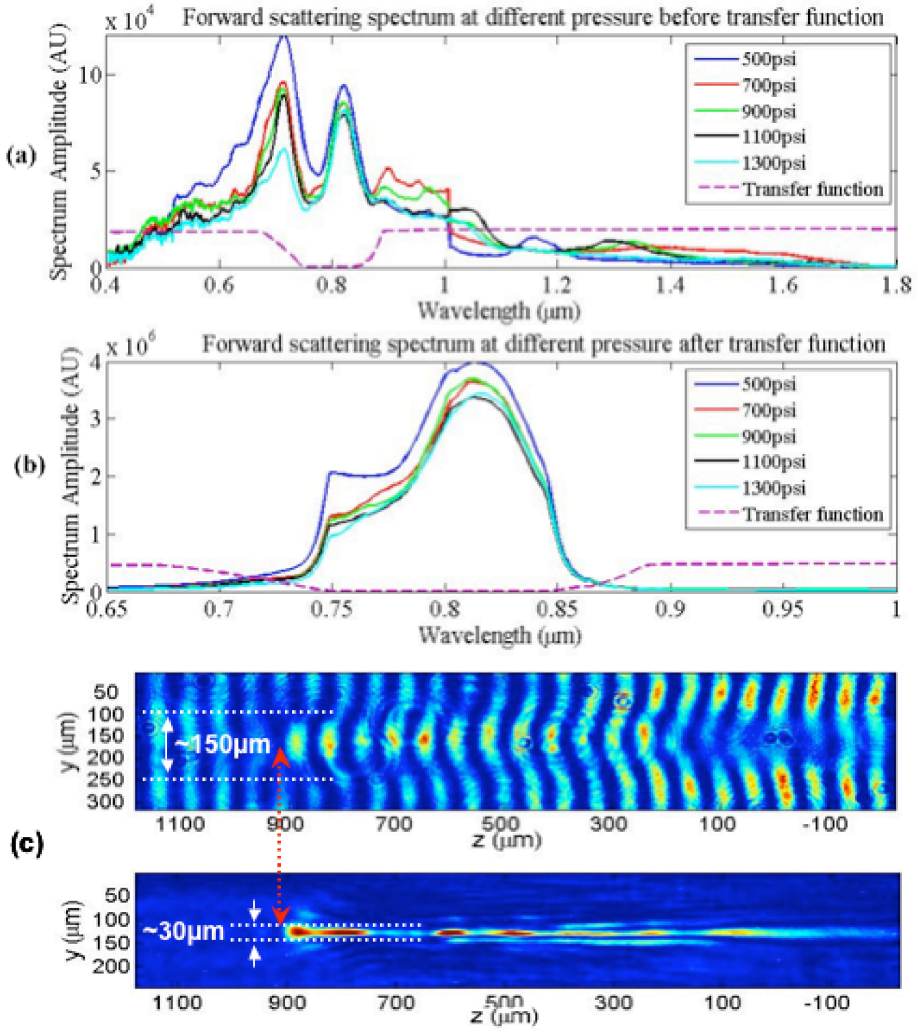

Figure 4.4: a)Forward scattering spectrum at different pressure before applying the transfer function; (b) Forward scattering spectrum at different pressure after applying the transfer function; The transfer function is the purple curve plotted in both figures; (c)An interferometry image of the plasma for the low density experiment and a refractometry image for the high density 2mm gas jet experiment. The red dotted arrow marks the plasma fronts. The laser is going from right to left.

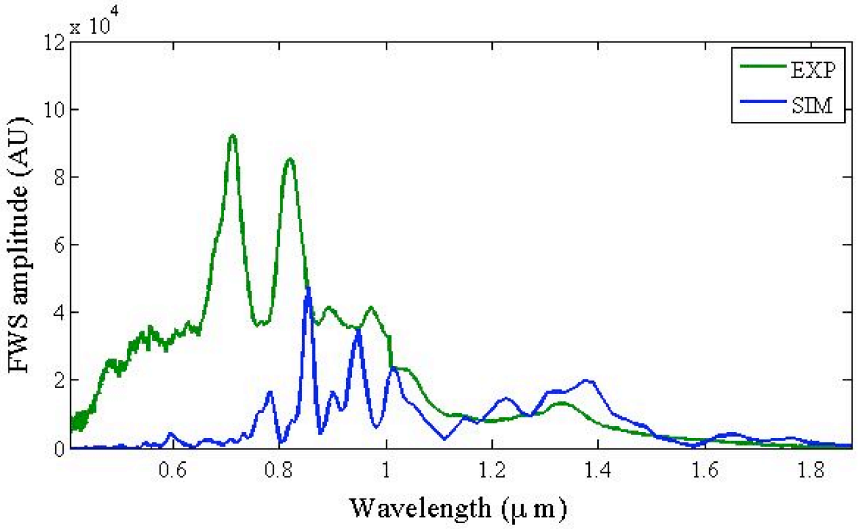

Figure 4.5: Simulation (green line) and experimental (blue line) results of forward spectrum.

experiments reasonably well. The blue shifted signal from the experiment appears stronger than from the simulation. The reason is that the simulation doesn't include the ionization induced blue shift. The center part of the spectrum is much stronger in experiment than in simulation. The reason is discussed in previous paragraph.

4.4 Summary

A broad band spectrum from 2ω to $1/2\omega$ was observed the first time in the FSS diagnostics when a high intensity ($\sim$ 2TW) ultra-short ($\sim$ 50fs) laser pulse interacts with a plasma of $\geq 5\times10^{19}cm^{-3}$ the density. Due to the high growth rate ratio of SPM over FRS, no FRS was observed. A red shifted signal up to 1.6μm was observed and attributed to photon deceleration. Simulation work shows good agreement on the deceleration induced red shift in the forward spectrum.

CHAPTER 5

Electron energy spectrum

As discussed in the previous chapter, in the high density experiments, the observed large photon deceleration of the laser pulse suggests the presence of large-amplitude plasma waves. We have already noted that since $P > P_{cr}$, the laser spot size within the plasma is almost certainly ∼2-3 times smaller than the incident size so that the laser E-field can, within L_{sf}, become ∼2-3 times larger. Since the vector potential $\propto E/\omega$, the photon deceleration can boost the initial local vector potential up to ∼4-9 times larger. Thus, after some propagation in the plasma, we can expect the ponderomotive force $\propto a_0$ to become strong enough to put us into the blowout or bubble regime where electron trapping can easily occur. The energy of the electrons is measured with an imaging electron spectrometer, introduced in chapter 3 section 3.3. As we expected, there are no measurable electrons in the low density experiment, while in high density experiment (for both the 1mm and 2mm gas jets), quasi-monoenergetic electron beams were often detected. However the reproducibility of these measurements was low due to: (a) the necessity of having a "slit" (the hole in the gold coated mirror) for the electron spectrometer and; (b) the low probability of the electrons hitting the slit due to a fluctuation in the direction of the accelerated electrons. This pointing instability issue is discussed below.

5.1 Pointing instability

In the high density experiments, due to the highly nonlinear process of laser evolution, from self-focusing to bubble formation, any asymmetry at the beginning of the jet can be amplified later and cause a pointing instability where the electron trajectory is off from the forward direction. This happens even in simulation where the asymmetry is from statistical noise. Figure5.1 shows the plasma density evolution when the laser pulse (with the same parameters as that of our laser) interacts with a gas jet of density of $5 \times 10^{19} cm^{-3}$ with a 200μm long ramp. The images are snapshots in time of a slice through the center of the "moving window" simulation box and are in an order of left to right and up to down. The simulation shows that the asymmetry develops in the laser polarization direction. At the beginning of the blowout phase (dump 23), it is the wave buckets in the front that are a little bit distorted from a symmetric bubble. Here, where $c\tau_L \approx 3\lambda_p$, the electrons accelerated in the sheath of the bubble as well as those injected into the bubble interact with the laser field (polarized in the plane of the images in Fig.5.1). Since the electron velocity is now close to the laser phase velocity, the wavelength of the laser seen by these electrons is highly elongated due to the relativistic Lorentz expansion. Thus they see an electric 'wiggler' rather than a ponderomotive force. It is this quasi-static laser field that causes the bending of the electron trajectory. Later on, the plasma wake caused by the bent electrons will guide some of the laser power away. The simulation show no deflection in the plane perpendicular to the plane of polarization.

The statistics of the electron pointing instability in the experimental data agrees with this interpretation. This indicates that the instability—actually, the shot-to-shot random phase of the laser field that the trapped electrons encounter—is caused by the electrical field of the laser pulse and thus would not occur if

$c\tau_L \approx \lambda_p/2$ — the desired operating condition for a LWFA. In Chapter3 where the set-up of the electron energy diagnostic was introduced, we see that electrons reach the phosphor only if they can make through the 1cm diameter hole (the spectrometer "slit") of the gold coated mirror located 25cm away from the gas jet. This requires a pointing jitter of $< 1^\circ$. Fig.5.5 shows electrons leaving at an angle of $\sim 6^\circ \gg 1^\circ$. Therefore, for many experimental shots, the electron beams will not make through the hole.

5.2 Experimental results

In the 2mm, high-density gas jet experiments, electrons that show up on the phosphor appear mostly in the form of quasi-monoenergetic electron beams, as shown in Figs.5.4b and c. Figure5.3 shows phosphor images of two typical shots taken with the magnetic field turned off; i.e., no dispersion in energy. The core of the electron beam is seen to be collimated with a divergence angle of only $< 0.5^\circ$, albeit surrounded by a halo of possibly low energy electrons. Figure5.4a shows a rare shot where either the electron "beam" has a big divergence angle and fills the hole in the gold mirror or the core of the beam missed the hole and we see only a low energy halo. In either case, the horizontal size of the bright area is the "shadow" or projected size of the slit (the hole in the gold mirror) on the phosphor, while the vertical size is limited by the phosphor itself. From this picture, knowing the distances of the gas jet and the slit to the phosphor, the uncertainty of the electron energy can be obtained for the quasi-monoenergetic shots shown in Figs.5.4b and c. Assuming (incorrectly) that the center of this "shadow" corresponds to infinite energy, Fig.5.4b shows a electron beam of finite energy but positive charge, which is clearly can not be true. Considering that the electrons may have entered the left edge of the slit, (the projection seen in

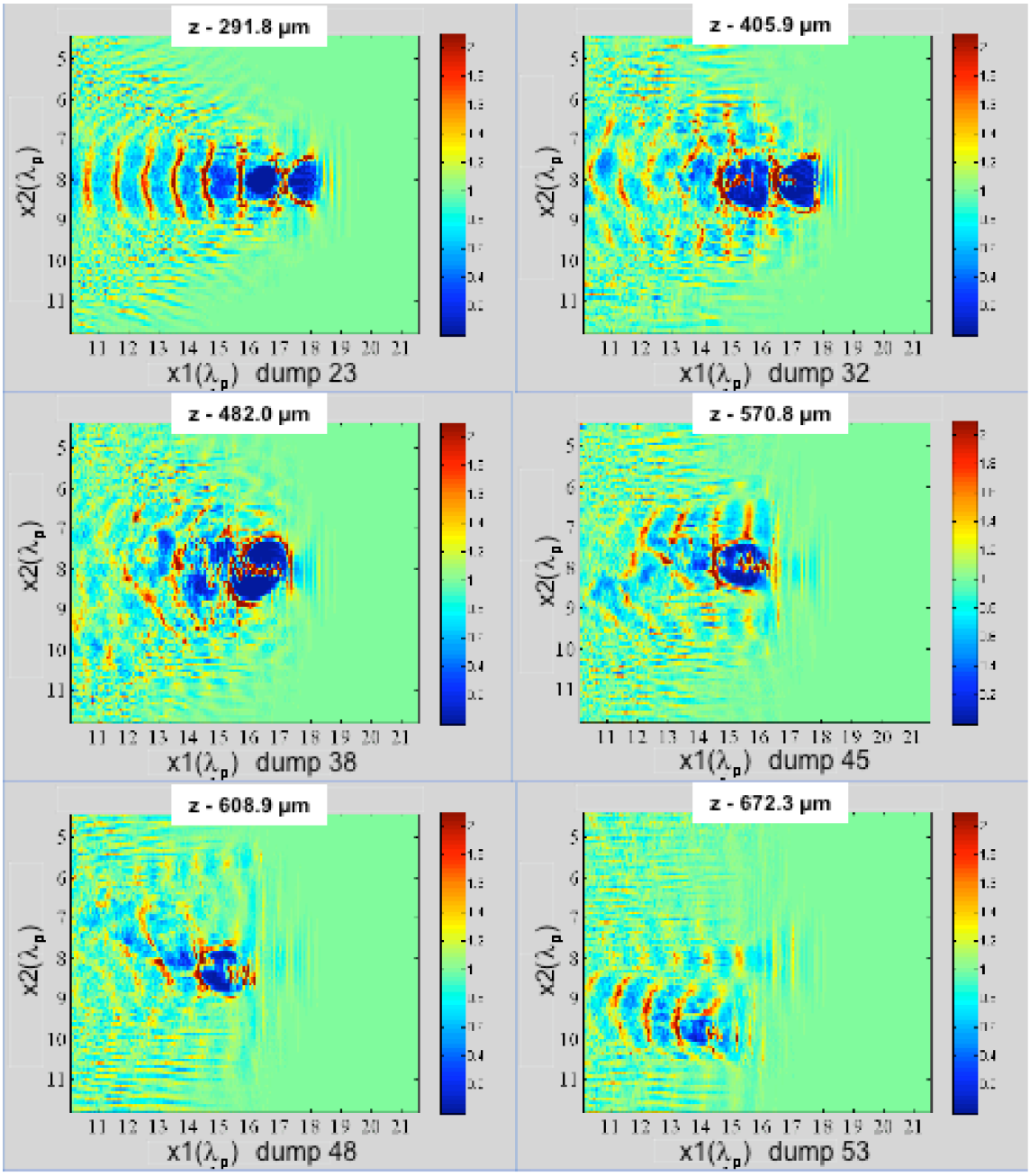

Figure 5.1: Simulation results of plasma density at different propagation distance of the laser. The x2 axis is the laser polarization direction, x1 axis is the laser propagation direction.

Fig.5.4a), the electron energy in Fig.5.4b can be anywhere from 70MeV to ∞. For the same reason, the energy of the electron beam shown in Fig.5.4c can be from 10MeV to 70MeV. Although choosing a more narrow slit in principle could resolve this uncertainty, we estimated that the number of shots (per day of running) would be so low as to lead to new questions about the statistics of that sample. A new electron spectrometer was subsequently designed to capture an image of the electron beam before the magnetic field (and thus define the slit location) as well as after the magnetic field. This "two-screen" method will be implemented in the future.

The number of electrons were measured with an integrated current transformer (ICT) which was put in the vacuum chamber in the forward direction in the early days of the experiments. It was taken out later because we found it contaminated the vacuum chamber. The maximum number of accelerated electrons were measured as $180pC$, shown in Fig.5.2. The vertical axis is the amplitude of the phosphor image and the horizontal axis is the amplitude of the ICT signal. The experimental data shows a reasonable correlation between these two signals.

In the 1mm gas jet experiment with a much higher density ($n_p \sim 2 \times 10^{20} cm^{-3}$), the electrons were not as well collimated as those in 2mm gas jet experiment. For most of the shots, the electrons filled the wide slit (the hole in the gold mirror) and appear on phosphor as shown in Fig.5.5a (magnetic field off) and in Fig.5.5c (high magnetic field). Only for a few shots did the electrons form a monoenergetic beam, one of which is shown in Fig.5.5b. We believe that this enhanced divergence is because, when the laser pulse interacts with this very high density plasma, it typically results in severe likelihood. Such filamentary structure could in fact be seen in the refractometry diagnostic. The angular spread can be due to a combination of the angular spread of individual filaments and the

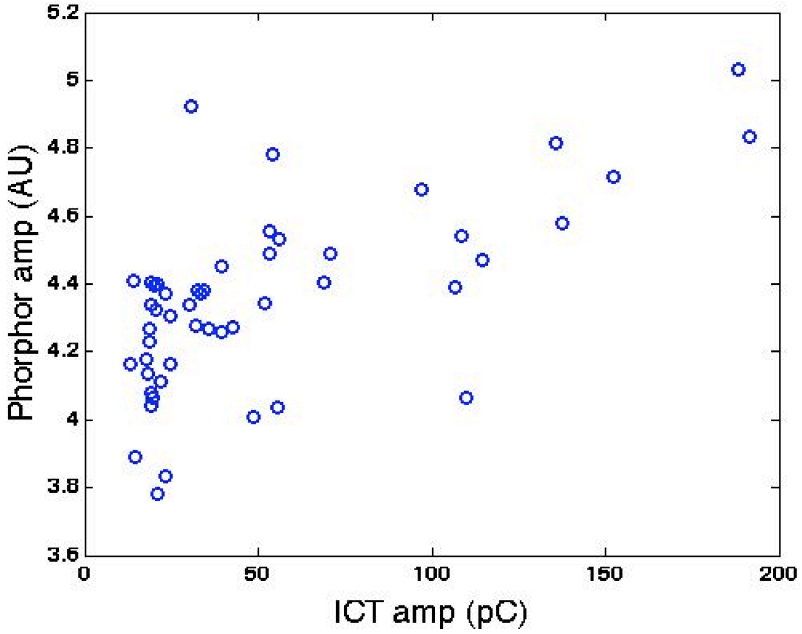

Figure 5.2: The intensity of light on the phosphor versus the ICT amplitude, the unit of which is converted into number of pC.

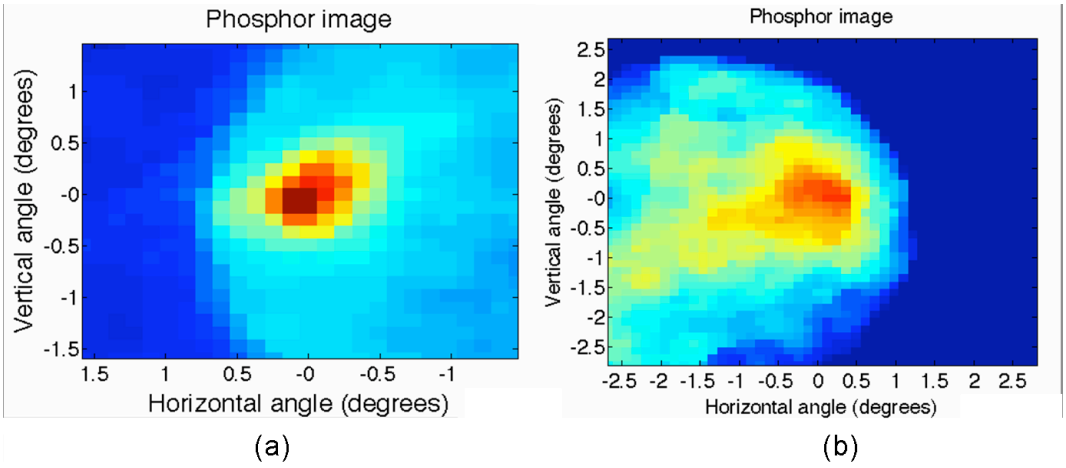

Figure 5.3: Phosphor image of electrons. (a) and (b) show the divergence angle of the electron beam of two typical shots.

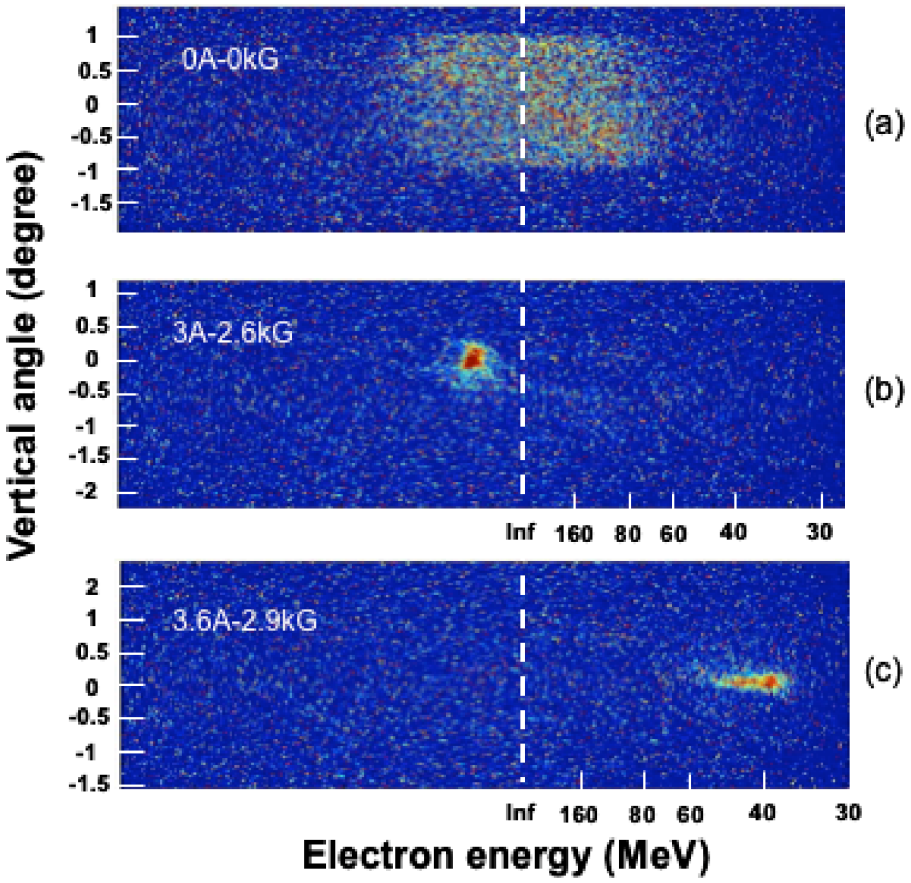

Figure 5.4: Electron spectrometer image for 2mm gas jet experiment. a) No magnetic field, electrons fill up the hole in the gold mirror. The projection of the hole on the phosphor can be used to estimate the uncertainty of the electron energy measured with the magnetic field on. b) Electron spectrum at $B = 2.6$kG. c) Electron spectrum at $B = 2.9$kG.

likelihood of rapid dephasing of the electrons with the plasma wave which would cause them to lose energy and be more susceptible to scattering by the laser and wake fields.

5.3 Simulation results

The simulation discussed in Fig.5.1 also gives the electron energy spectrum at different interaction lengths (L) and four of these are shown in Fig.5.6. The horizontal is the electron energy, and the vertical axis the the position along laser propagation direction with laser going from left to right. The first bucket is a little bit before (to the right of) the 150μm mark. The color axis shows the charge density of accelerated electrons which has been integrated over the two transverse directions. For $L = 300\mu$m (see Fig.5.6), after the laser has self-focused and the laser vector potential has grown due to some photon deceleration, the electrons have been trapped and accelerated within each plasma wakefield bucket, especially the first two because the laser pulse length is about two plasma wave lengths and is still strongly driving these two buckets. The highest energy can reach a couple hundred MeV. As more electrons get trapped, any laser-pulse intensity behind the second bucket gets diffracted away. Mono-energetic electron bunches (below 100MeV) start to form (shown in picture $L = 350\mu$m) as they rotate in phase space at roughly the dephasing length. As laser goes further, the group velocity of the laser—and thus the phase velocity of the plasma wave—will drop because of photon deceleration and head erosion, which will cause severe dephasing of the electrons. As shown at $L = 450mu$m, electrons in the fisrt bucket (where photon deceleration is strongest) have lost most of their energy. Meanwhile, those electrons that were in the second bucket have entered the accelerating portion of the first bucket (see Figure5.1) and have been boosted

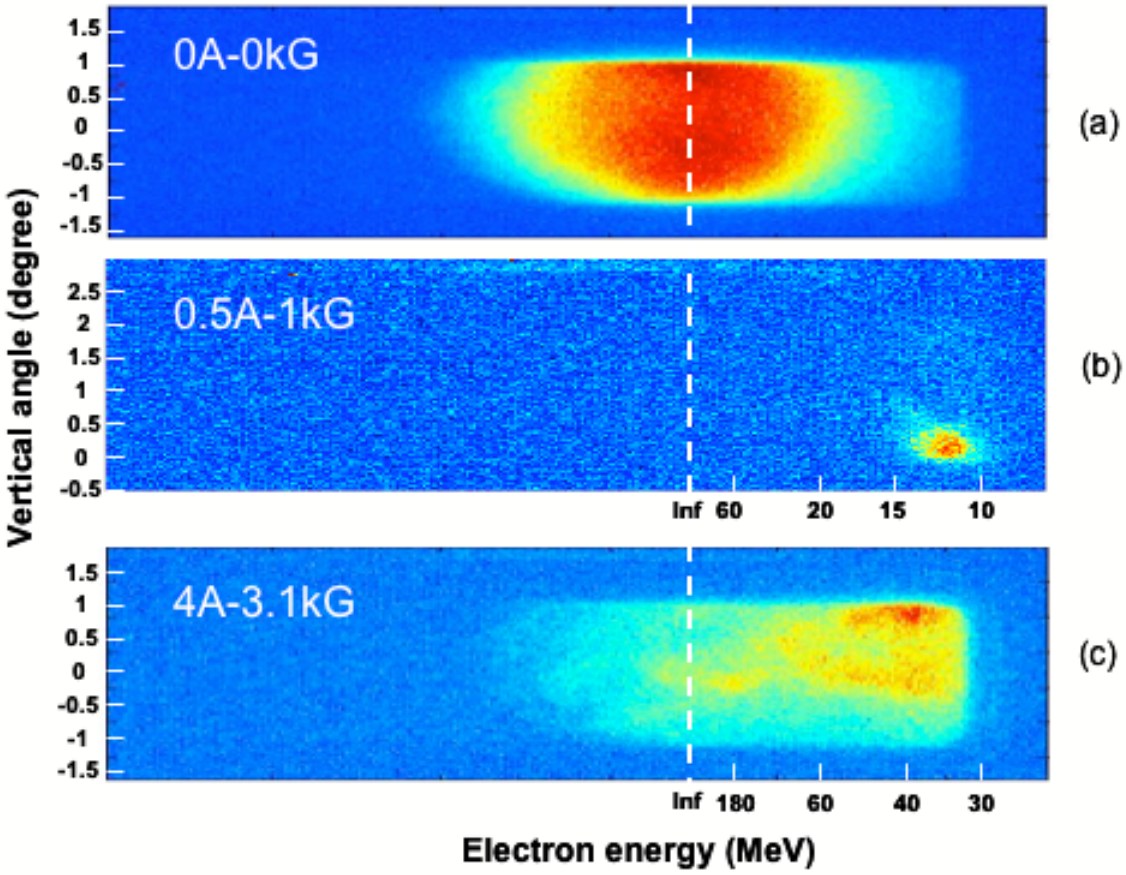

Figure 5.5: Electron spectrometer image for 2mm gas jet experiment. a) No magnetic field, electrons fill up the hole in the gold mirror. The projection of the hole on the phosphor can be used to estimate the uncertainty of the electron energy measured with the magnetic field on. b) Electron spectrum at $B = 1$kG. c) Electron spectrum at $B = 3.1$kG.

up to even higher energies. .

As the laser pulse reaches the pump depletion length ($\sim 600\mu$m), the red-shifting of the laser is so severe that the on-axis electrons have dephased and the number of electrons above, say, 100MeV, has dropped substantially. However, there are still spectral features at a few tens MeV and higher which may end up as the "beams" on the phosphor within the experiment. We suspect that these surviving spectral features may be those that wandered off axis due to the pointing instability discussed earlier in this Chapter. Although this simulation shows a large number of low-energy electrons, we measure quasi-monoenergetic beams on the phosphor for most of the shots in 2mm gas jet experiment. There could be two reasons for this: firstly, the signal-to-noise ratio is so high on the phosphor images (due to the low bit-depth of the camera and the large safe-operating distance to the phosphor) that the low energy spectrum is buried in noise; secondly, as we will see in the next Chapter, all the accelerated electrons must penetrate through additional plasma (beyond the pump-depletion length) where they will produce there own wake. This is already seen in the last frame in Fig.5.1 where the escaping, high-energy electrons are producing their own wake. We would expect that the large number of very-low-energy electrons would be scattered transversely either in the on-axis remnant of the laser wake or in the remnant of the wakefield from the escaping electrons. When the magnetic field is off, there is always a measurable halo around the core of the electron beam, as seen in Fig.5.3, which could be these (scattered) low-energy electrons seen in simulation.

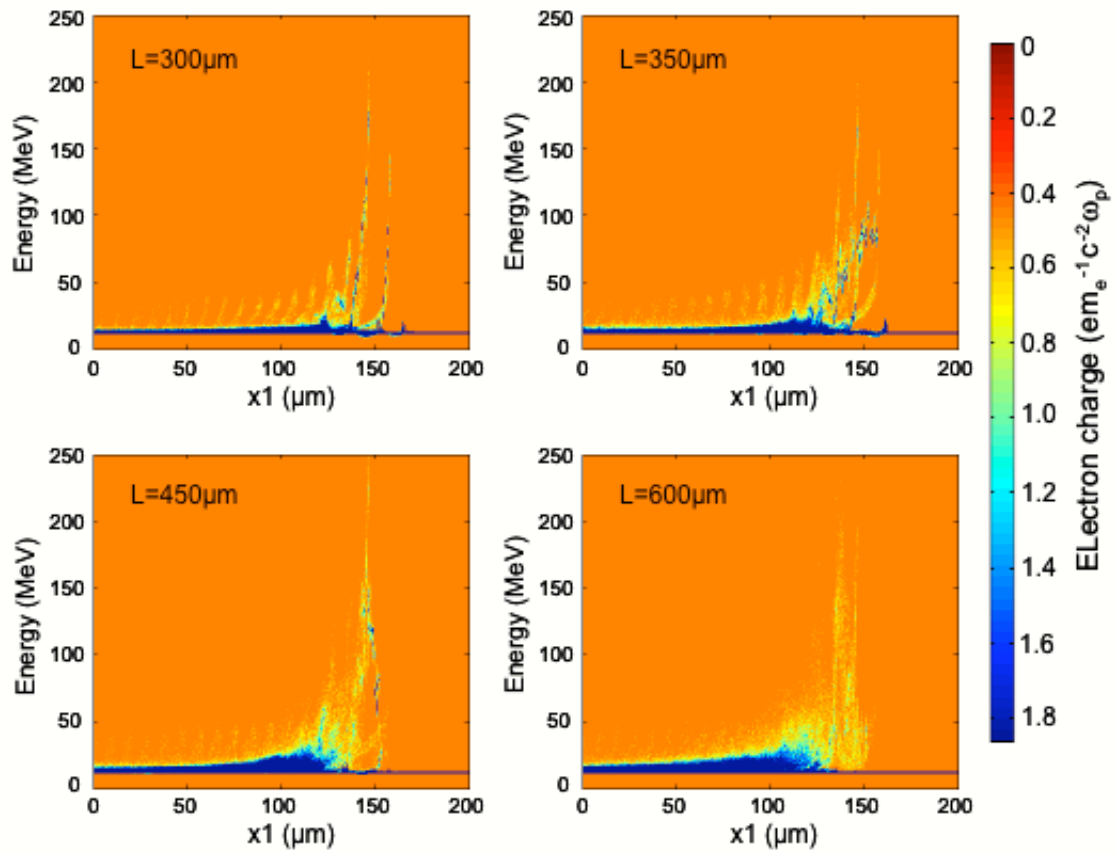

Figure 5.6: Electron spectrum from simulation for 2mm gas jet experiment at different laser plasma interaction lengths L.

5.4 Summary

In summary, quasi-monoenergetic electron beams of 10MeV to 80MeV (possibly higher) have been routinely measured in the 2mm ($5 \times 10^{19}\text{cm}^{-3}$) gas jet experiment. The charge of electrons is typically a couple of hundred pico-Coulombs. In the 1mm gas jet experiment ($20 \times 10^{19}\text{cm}^{-3}$) filamentation and dephasing are so severe as to make meaningful energy measurements nearly impossible. The pointing jitter is a problem for both cases because of high plasma densities where the laser pulse length is 2 to 4 times the plasma wavelength. Simulations for the 2mm gas jet conditions show a pointing jitter of $\sim 1^\circ$, which is sufficient for the electron beam to pass though an essentially arbitrary point in the hole in the gold mirror (our slit) and hit the phosphor with a shot-to-shot variation of the "infinite" energy point. This is the most important reason why the electron beam energy cannot be stated precisely or correlated to other experimental factors. Nevertheless, simulation shows that our energy estimates for the 2mm gas jet case are not out of bounds. The low-energy portion of the spectrum seen in simulations are not very well reproduced in the experimental results. The reason is partly experimental (the low signal-to-noise in the phosphor image) and partly physics, due to a scattering loss of the low energy part of the spectrum after propagating through the remainder of the plasma, which the simulations do not account for.

CHAPTER 6

Evolution of relativistic plasma wavefront

In a laser wakefield accelerator experiment where the length of the pump laser pulse is a few plasma periods long, the leading edge of the laser pulse undergoes head-erosion and frequency downshifting as the laser energy is transferred to the wake. Therefore, after some propagation distance, the group velocity of the leading edge of of the pump pulse and therefore of the driven electron plasma wave- will slow down. This can have implications for the dephasing length of the accelerated electrons and therefore needs to be understood experimentally. We have carried out an experimental investigation where we have measured the velocity v_f of the 'wave-front' of the plasma wave driven by a nominally 50fs (FWHM), intense ($a_0 \sim 1$), 0.8μm laser pulse. To determine the speed of the wave front, time- and space-resolved refractometry, interferometry, and Thomson scattering were used. In this chapter, a low density experiment ($n_e \sim 1.3 \times 10^{19} cm^{-3}$), which doesn't involve electron acceleration will first be discussed as a reference, then a high density 2mm gas jet experiment ($n_e \sim 5 \times 10^{19} cm^{-3}$) will be introduced and the correlation of the evolution of the plasma wavefront and electron acceleration process will be discussed.

6.1 Evolution of plasma wavefront in low density experiments

In chapter3 section3.1.2, the interpretation of TRR and TRI has been discussed using the inset in Fig3.1. We know that the time evolution of plasma wave-front and ionization front were obtained by recording TRR and TRI images with delay-line time steps of 333fs. A selection of the resulting images are shown in Fig.6.1a. The delay time labeled 'zero' corresponds to the case where the probe pulse and the pump pulse overlap in time at the entrance to the gas jet. The blue circles (green diamonds) in Fig.6.1b show the longitudinal position of the plasma wave-front (ionization front) while the red line is the linear v_g of the pump beam for a uniform plasma of $n_e = 1.3 \times 10^{19} cm{-}3$. The shot-to- shot variation in the data are thought to be due to real variations in the incoming pump pulse and/or in the initial profile of the He-gas from the jet. Additionally, due to the discreteness of the fringes, there are inherent uncertainties ($\pm 20\mu$m) as to where the ionization front actually begins. To the extent that the data for the position of these fronts follows the linear group velocity (the red line), we may conclude that, at this low n_e, the pump propagates with no substantial distortion of its envelope or spectrum all the way to $\sim$1.5mm, the end of the gas jet. In fact, the maximum measured shift in FSS was only a few times of the pump-laser bandwidth of $\sim$24nm (see Chapter4) and no accelerated electrons were observed. When we go to the high-density gas jet, the limited collection angle for the probe beam will render the interferometry essentially useless. That is, fringe information is lost due to refraction. However, as we will see, the apparent focusing effect of the density depression at the very front of the refractometry will more than compensate for this strong probe-beam diffraction.

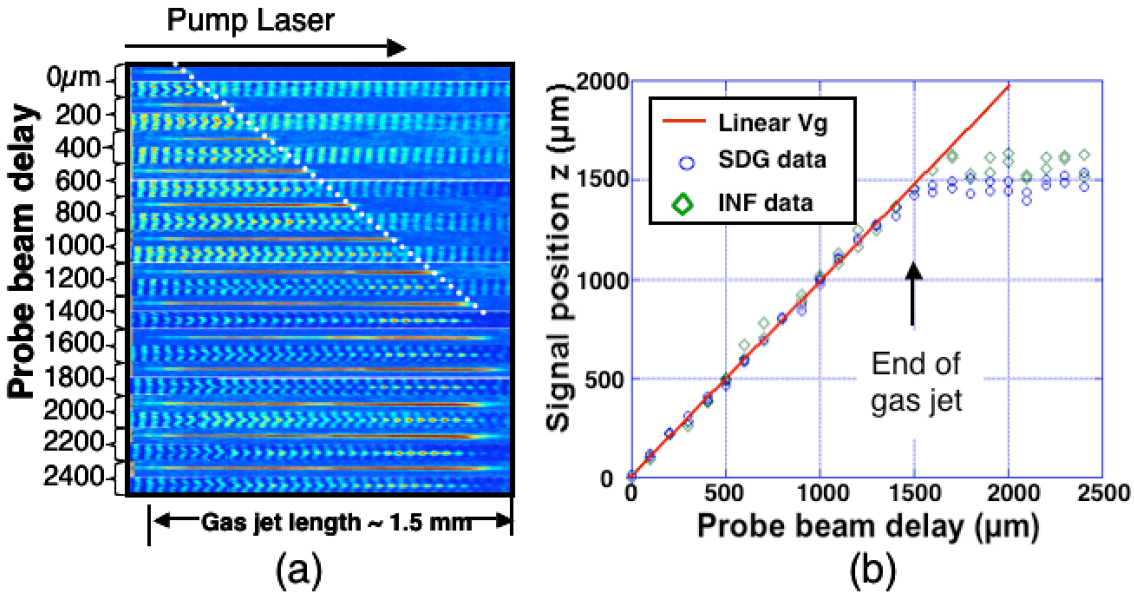

Figure 6.1: (a) Selected TRR and TRI image pairs for the low density ($1.3 \times 10^{19} cm^{-3}$) experiment. The front of which is be plotted in (b). The dashed line is a guide for the eye. (b) Experimental results for SDG (blue circles) and INF (green diamonds) of the probe timing scan (333fs or 20μm steps) along with the laser linear v_g (red line). The white dashed line in (a) is a guide for the eye.

6.2 Evolution of relativistic plasma wavefront high density experiments

Figure6.2 shows the result of a probe-beam timing scan. This timing scan begins with the probe pulse temporally overlapping the pump pulse at the entrance of the gas jet and ends 1.2mm into the gas jet with a step size of 67fs (20μm). Some selected TS and SDG images are shown side-by-side in Fig.6.2a and Fig.6.2b. The probe beam delays for these are labeled on the left. From data plotted in Fig.6.2c, one can see that, in contrast to the low n_e case of Fig.6.2b, the velocity of both the plasma wavefront and the extreme front-edge of the TS begin to depart from the linear v_g beyond about 300μm into the plasma. At 800μm into the plasma, the measured drop in these velocities (the slope of the plotted data) is about 5 percent which represents about an 40μm slippage of these fronts relative to v_g. Results from the FSS diagnostic (Chapter4) reveal considerably wings on the red side. Results from the electron spectrometer diagnostic (Chapter5) indicate electrons out to about 40 MeV and often appeared to be quasi-monoenergetic. With the dipole magnet of the electron spectrometer off, some shots showed forward emitted electrons that were extremely well collimated (<than 5 mrad full angle). Comparing with the low density results, it can be concluded that the slowing down of the plasma wavefront may well be associated with the acceleration of electrons; i.e., a large wakefield in the blowout or bubble regime.

6.3 The four stages of electron acceleration indicated by the time scan results

To understand more about the relationship between the plasma wavefront evolution and the process of electron acceleration, the experimental results will be

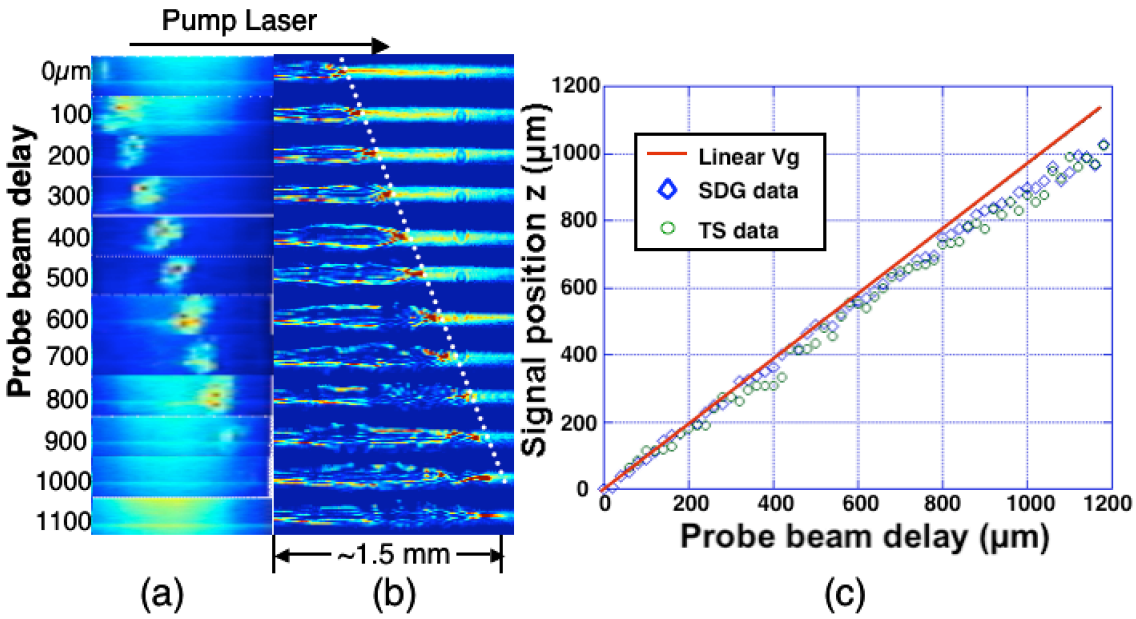

Figure 6.2: (a) Selected TS images; (b) the corresponding SDG images. The dashed line in (b) is representative of the position of a plasma wavefront for the small-delay shots; (c) positions of the TS (green dots) and SDG (blue diamonds) for all images, 67fs steps. The red line in (c) is the linear v_g for a uniform plasma at this n_e.

plotted again but in a "speed of light window" and compared with the simulation results. It is found that the plasma wavefront evolution clearly reflects the laser self-focusing, dephasing, photon deceleration and pump depletion inside of a plasma. These four concepts just mentioned were introduced in Chapter 1.

6.3.1 Moving window results of low density probe timing scan

Again as a reference, the low density data will be shown first here in Fig.6.3 as was done in section6.1. Figure6.3a shows the simulation results of the plasma density evolution with time. This simulation launches a laser pulse with the same parameters as the laser used in the experiments, into a plasma with a density of $1.3 \times 10^{19} cm^{-3}$. The horizontal axis of Fig.6.3a is time or, in the experimental case, the probe beam delay. The vertical axis is the longitudinal position z. Each vertical pixel column is a lineout down along the center of the plasma channel at that particular time, time being the horizontal axis. The laser is moving up. The time scale for this simulation-derived image is the same as the scale as the experimental data shown in Fig.6.3b. The black, nearly-horizontal dotted line in Fig.6.3a lies along the the density peak at the back of the first plasma wave period. If the plasma wave moves with the velocity of the laser linear group velocity, it will follow this line, as can be shown by a simple calculation. Therefore this line can also be viewed as the line of v_g. Figure6.3b shows the experimental results of the TRR in the moving window in a probe timing scan which is, in other words, a re-plotting of the TRR data in Fig.6.1b but in a speed-of-light window to magnify the small deviation of the motion of the plasma wavefront from the v_g line. The red line in Fig.6.3b is the same as the black dotted line in Fig.6.3a, the "Vg line". Figure6.3b tells us that the plasma front more or less follows the linear Vg line within the entire gas jet length ($\sim$ 1.5mm). This indicates that

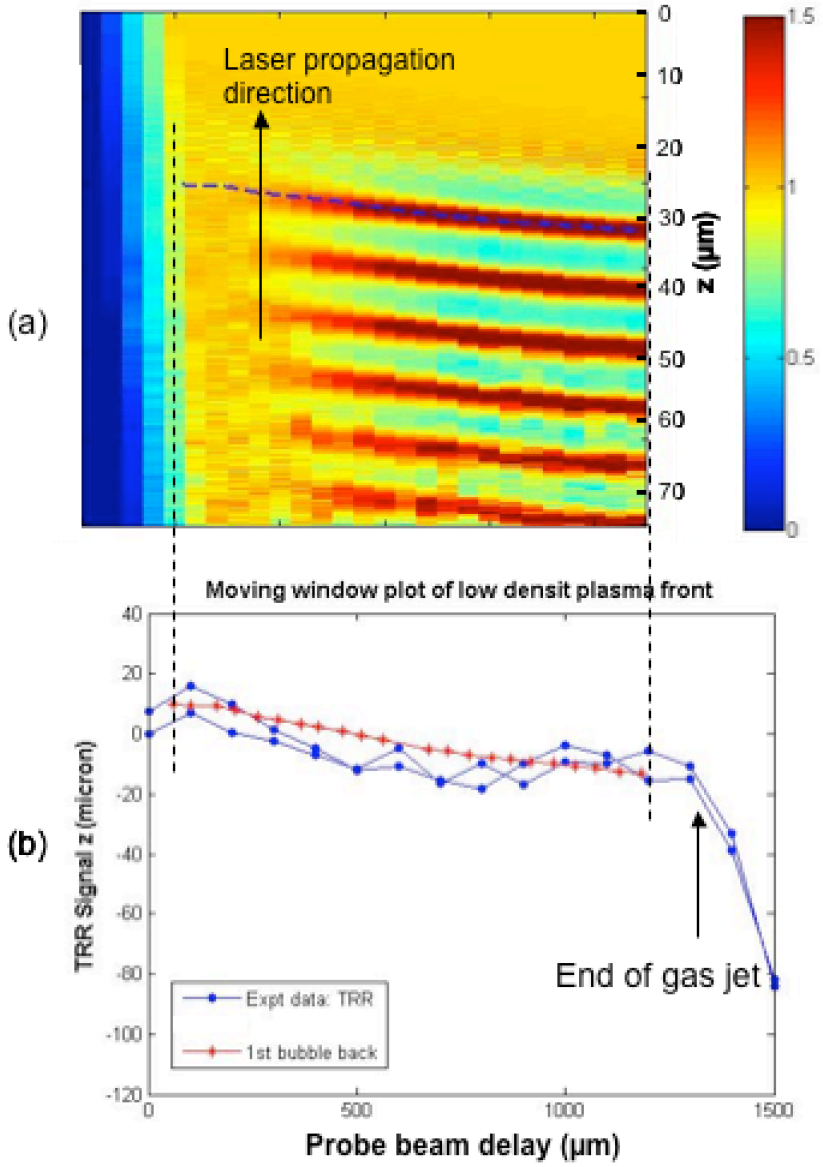

Figure 6.3: (a) Simulation results of plasma density wave and (b) experimental results of plasma wavefront evolution during a probe timing scan in speed of light window (moving window). Pump laser is going up in the figure. The red line in (b) is the same as the black dotted line in (a) and it follows the laser linear group velocity at this plasma density almost exactly.

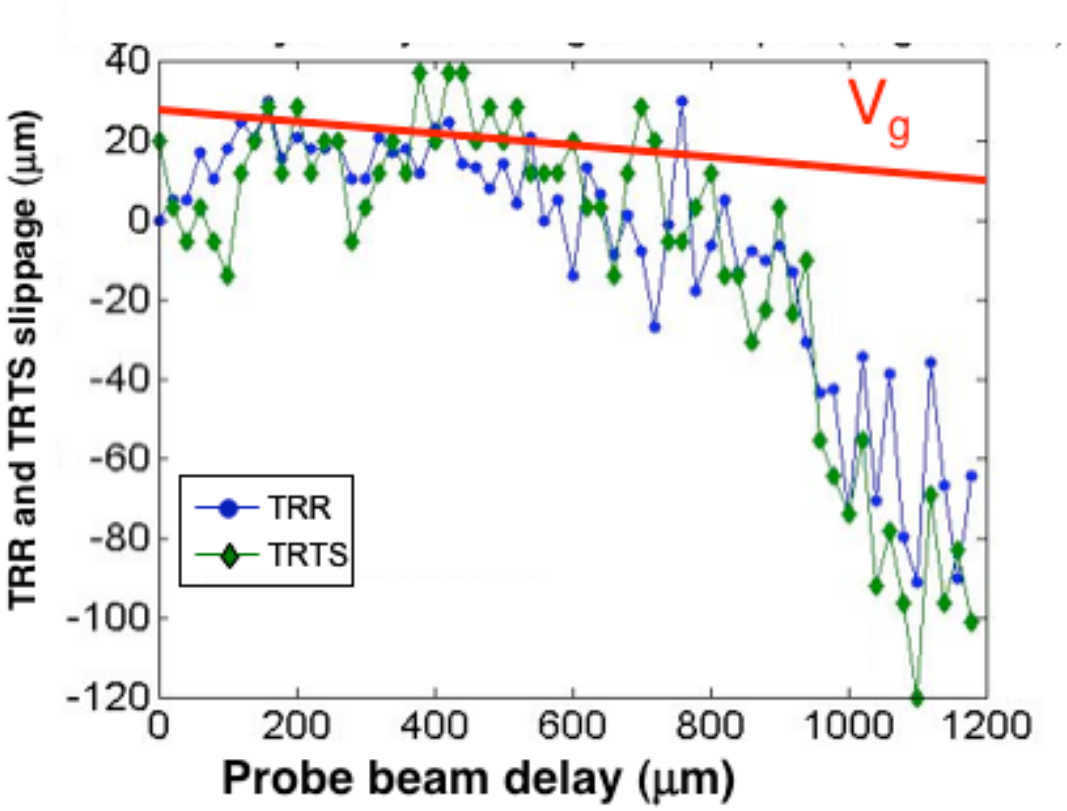

Figure 6.4: Moving window plot of the high density timing scan experimental results.

there is no physical process that causes the plasma wavefront to deviate from the linear Vg line in this low density experiment.

6.3.2 Moving window results of high density probe timing scan

Figure 6.4 shows the moving window plot of the high density timing scan experimental results, a re-plot of Fig.6.2c in the speed-of-light window. The red line is again the v_g line for this higher density of $5 \times 10^{19} cm^{-3}$. We notice that the plasma wavefront moves faster than v_g at the beginning and then slows down. Near the end, it slows down much faster. The total slippage is $\sim 100\mu$m over the

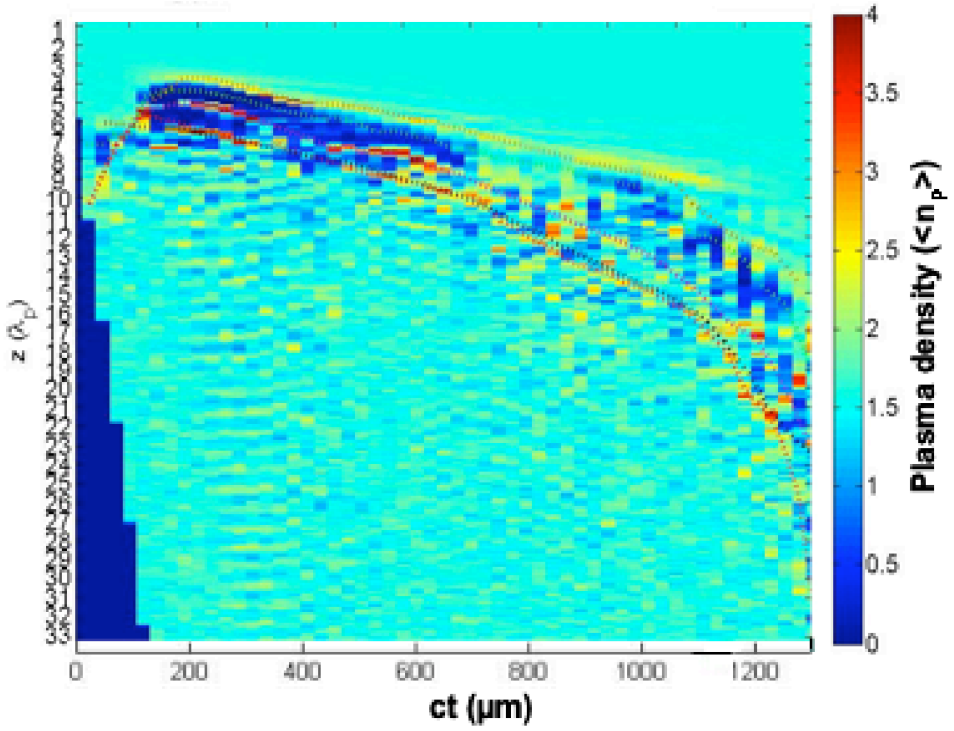

Figure 6.5: Moving window plot of the plasma density from the high density simulation.

1200μm scan. Before looking into explanations for this deviation from v_g, let's look at the simulation data for these conditions.

Figure 6.5 shows the moving window plot of the plasma density for this high-density simulation, which is the same plot as Fig.6.3a but with a density of $5 \times 10^{19} cm^{-3}$, the same as the gas jet density in the high density experiments now being discussed. Again, each vertical pixel column is the center lineout of the plasma density at the time (or propagation distance) indicated on the horizontal axis. Figure 6.6 shows the corresponding laser field and self focusing, pump depletion, group velocity changes. Figure6.7 shows the experimental results and simulation results together. The simulation lines are the dotted lines in Fig.6.5. These dotted lines follow: the front of first bucket (or bubble); the center of the

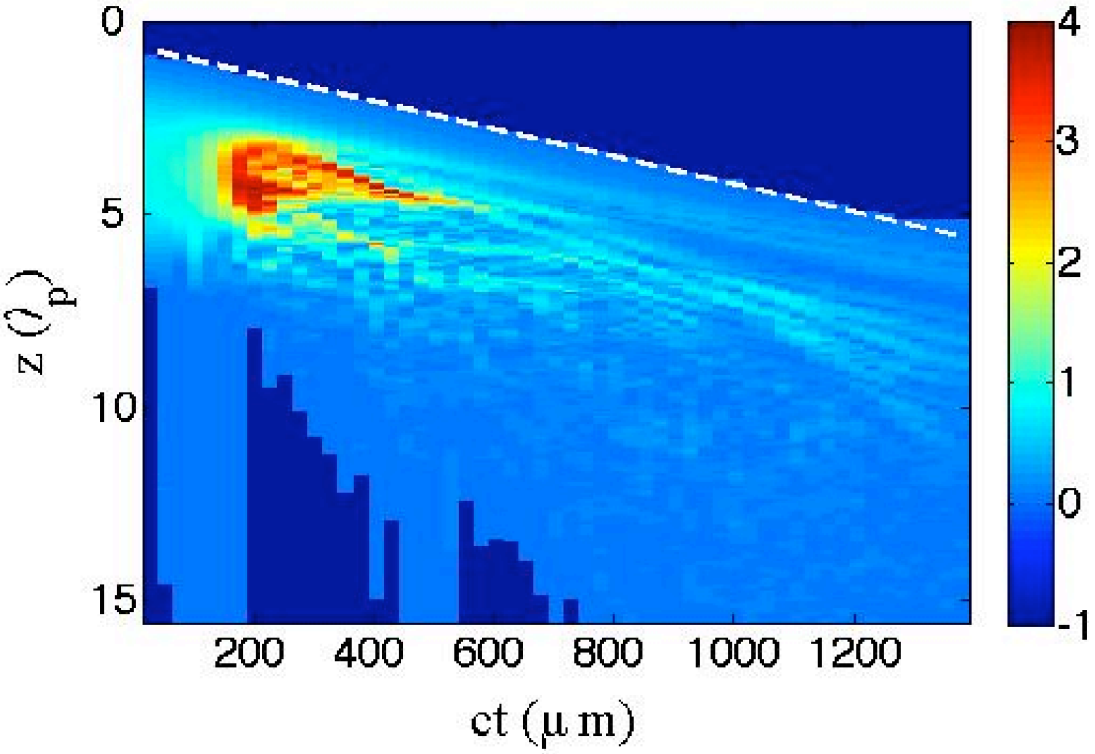

Figure 6.6: Moving window plot of the normalized transverse electric field of the laser (with contributions from the 3-D plasma wakefield at larger z's, also from the high density simulation.

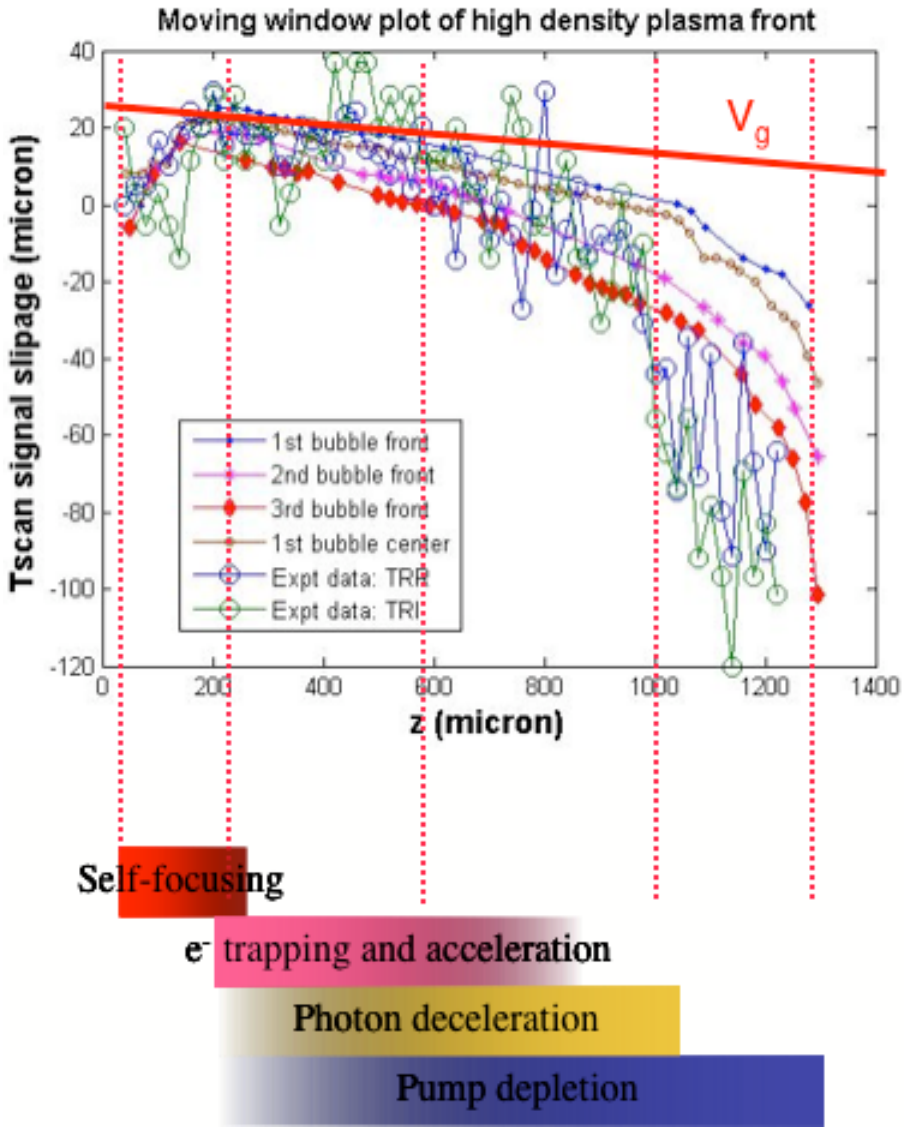

Figure 6.7: Experimental and simulation results of probe timing scan of plasma front. Four stages of electron acceleration are specified. The laser self-focusing length (second red dotted line), the dephasing length (third red dotted line), and the pump depletion length (fourth red dotted line) are labeled.

first bucket; the front of the second bucket; and the front of the third bucket, respectively. Although the experimental results match the lines from the simulation very well up to 1mm, we cannot infer from this which feature is responsible for the bright spot in the refractometry. We believe that the refractometry signal is due to the focusing effects of the first two buckets, since that is approximately the transit time of the probe beam.

These 50fs time resolution diagnostics give us a very unique way of measuring the small (20μm) variations in the movement of plasma wavefront. Based on the evolution of the plasma wavefront in the speed-of-light window and the simulation pictures in Fig.6.5 and in Fig.6.6, four stages of the laser-plasma evolution that lead to electron acceleration can be identified: self-focusing, e^- trapping and acceleration, photon deceleration leading to a drop in v_p, and finally pump depletion, as shown in the lower part of Fig.6.7. The intensity of the color bar for each of these (overlapping) stages is meant to indicates the strength of the phenomenon that is happening. These four stages will be summarized below.

In the first $\sim 200\mu$m of propagation, the plasma wavefront appears to move faster than the speed of light. This is because the wake amplitude scales with the ponderomotive force and the contours of constant a_0 are moving forward as the laser self focuses. This is clearly seen in Fig.6.6. In Chapter 1, the self-focusing length was calculated to be $\sim 200\mu$m using the same laser and plasma parameter, which agrees with the simulation and the experimental results. After this self-focusing, the vector potential of the laser increase from < 1 to about 4. This tremendous increasing in a_0 causes plasma wave grow very quickly into the nonlinear blowout regime and start trapping electrons. The simulation shows that this process of trapping and acceleration lasts for a few hundred microns; i.e., to $L \approx 400 - 600\mu$m. The experimental data track the simulation data

quite well over this range in Fig.6.7. The dephasing length calculated in Chapter 1 is a few hundred microns for large a_0 and drops to $\sim 200\mu$m as a_0 drops to below 1, assuming the laser frequency is a constant. This also more or less agrees with the dephasing length marked by the third red dotted line in Fig.6.7. More electrons get trapped and accelerated at the beginning when the electrical field of the plasma wave is high. As the plasma wave is generated by the laser and the electrons gain energy from the plasma wave, the laser lose energy. The number of photons is conserved, therefore the laser frequency must drop. This is energy-balance argument for photon deceleration, which has been discussed in Chapter 4, Section 4.2. Photon deceleration by definition would start as soon as the plasma wave is generated and continue until there is no plasma wave generated from the laser, as shown from the yellow color bar in Fig.6.7. Although we have not discussed this since Chapter 1, the etching of the large a_0 laser pulse — which occurs from the front of the pulse to the back, as described by Decker et al [50] — also contributes to the reduction of wavefront velocity in this range. The last stage is pump depletion, which is caused by the combination of photon deceleration, dispersion, head erosion and diffraction. At the pump depletion length the laser energy is tremendously reduced to a level that can no longer generate plasma wave, which is at the fourth red dotted line in Fig.6.7. This also agrees with the calculated results in Fig.1.1. After pump depletion length, the laser will continue further weakening depleting mostly by diffraction, which happen much faster in experiments compared with simulations because the laser used in experiment is far from an ideal Gaussian beam.

6.4 Summary

Taking the evolution of the plasma wavefront at low density experiment as a reference, this chapter discussed the evolution of the relativistic plasma wavefront at high density 2mm gas jet experiment at a spatial resolution of $\sim 20\mu$m using TRR and TRTS diagnostics. Correlating these results with the forward spectrum and electron spectrum as well as the simulation results, four stages of laser-plasma interaction: laser self-focusing, electron trapping and acceleration, dephasing and pump depletion, have been identified from the results of the evolution of the relativistic plasma wavefront. The estimates of self-focusing length, dephasing length and pump depletion length suggested by these results agree with the calculated results in Chapter 1.

CHAPTER 7

Conclusions

The Laser Wakefield Accelerator (LWFA) schemes is being studied in more than two dozen laboratories around the world and yet none of the experiments to-date have been carried out either in the linear wakefield regime or in the bubble regime. Most of the work falls in the so-called forced laser wakefield regime (F-LWFA) where the initially non-optimal (too long) laser pulse must evolve into a pulse suitable for exciting a large wakefield. The F-LWFA regime nevertheless has shown to generate low divergence (small emittance) and quasi-monoenergetic electrons beams in several experiments.

Exactly how an initially long pulse evolves to excite the wakefield that is reminiscent of that produced in the bubble regime and exactly how and where in this wakefield do the electrons become trapped are questions that have not been definitively answered yet. Furthermore it is not clear how the electrons escape from the wakefield and retain their relatively narrow energy distribution. It was the purpose of this work to answer some of these questions.

The laser used in this study was a 2TW, 50fs (FWHM), $\lambda = 0.81\mu$m Ti:Sapphire CPA laser focused to a 10μm spot size to give nominal intensity of $2\times10^{18}Wcm^{-2}$ or a normalized vector potential of $a_0 \sim 1$. At this power, the critical power for self-focusing is exceeded for plasma densities $n_e > 1.3 \times 10^{19}cm^{-3}$. We carried out two sets of experiment. The first at a plasma density of $1.3\times10^{19}cm^{-3}$ where the 50fs laser pulse was about 2 plasma wavelengths long but the laser power was

near the threshold power for relativistic self-focusing. At this density the linear estimate of the dephasing length was $\sim$ 1.5mm and the pump depletion length was $\sim$ 2mm. The second set of experiment was carried out at a higher density of $\sim 5 \times 10^{19} cm^{-3}$. The 2TW laser power was now clearly above the threshold for relativistic self-focusing and the laser pulse now occupied at at least 3 plasma wavelengths of a relativistic plasma wave. Both densities were produced using a gas jet nominally 2mm wide (in some cases an even higher density, 1mm diameter gas jet with n_e of $\sim 1.5 \times 10^{20} cm^{-3}$ was used.) At this higher density ($\sim 5 \times 10^{19} cm^{-3}$) the dephasing length $L_d \sim 200\mu$m and the pump depletion length was estimated to be 500μm. The laser beam propagation through the low density gas jet, where the wake excitation and relativistic self-focusing effects are relatively weak, is used as a reference for investigating the various nonlinear aspects of the laser-plasma interaction in the subsequent high-density beam propagation experiments.

A total of nine diagnostics were used in these two sets of experiment. The top view diagnostic, top view image (TVI), was used for alignment purpose for all experiments. Since it can see the relative position of the laser focus and the gas jet nozzle, the TVI was used to put the entrance of the gas jet at the laser focus. In he forward direction, a surface barrier detector (SBD) and an electron energy spectrometer (EES) were used to measure the X-Ray signal and the electron spectrum respectively. Another forward direction diagnostic, the forward scattering spectrum (FSS), which uses a low dispersion prism and a broadband ($400nm - 2.2\mu$m) spectral response camera, was used to measure the broadband forward scattering spectrum. Most importantly, the time-resolved side view diagnostics: time-resolved refractometry (TRR); time-resolved interferometry (TRI); and time-resolved Thomson scattering (TRTS), all with a temporal resolution of $\sim$ 70fs (or spatial resolution of $\sim 20\mu$m), were used to measure the evolution

of the plasma wave-front, and thus help to identify the different phases of laser-plasma interaction. Besides this, TRR can also be used as a prepulse monitor as it can distinguish between the plasmas generated by the prepulse and the main pulse. Another side view diagnostic is the side scattering spectrum (SSS). The set up is similar as that of the FSS. It also uses the prism and the broadband camera to measure the self-side scattering spectrum. The set up for these diagnostics is very compact so that a maximum of 6 diagnostics can be used simultaneously, which helps us to understand the physics by correlating the data generated by these different diagnostics.

Four overlapping but distinguishable phases of the evolution of the plasma wakefield were identified in the high density experiment using the three time resolved diagnostics, TRR, TRI and TRTS. It was found that at the beginning of the laser-plasma interaction, the wakefield appears to move faster than its linear phase velocity as the laser pulse relativistically self-focuses and its vector potential increases by a factor of 2-3. Then for the next nearly one linear dephasing length, the "plasma wavefront" or the "wake density front" propagates at approximately the nonlinear group velocity of the laser in the plasma. In the simulations of our experiments, the electron trapping is seen to occur at the beginning of this phase. In the third phase, the wakefield density front begins to slow down. This slowdown is thought to be related mostly to photon deceleration as a consequence of energy transfer to the wake. The etching of the large a_0 laser pulse—which occurs from the front of the pulse to the back, also contributes to the slowing down of wavefront velocity in this range. The last phase is when the wakefront rapidly recedes relative to the laser pulse as the energy of the laser pulse depletes. This occurs approximately when the laser propagates about one linear pump depletion length. Forward scattering spectral measurements show significant red-shifting in the spectrum, indicating a severe photon deceleration during the laser

propagation through the plasma. The red shifted spectrum, up to $\sim 1.6\mu$m, contributes to most of slow down of the wake density front in the third phase discussed above.

Highly collimated, quasi-monoenergetic electron beams were detected in the high density experiments. Electron energies of 10MeV to 80MeV (possibly higher) were measured. The charge of the electrons is a couple of hundred pico-coulombs. The electrons have to travel with an angle of $< 1^\circ$ from the forward direction in order to pass through the hole in the gold mirror (spectrometer slit) and to reach the phosphor. The pointing jitter was considered a main reason for the bad reproducibility of the electron beams.

The results of SSS (See Appendix A), which were obtained in the very high density ($1.5 \times 10^{20} cm^{-3}$), 1mm gas jet experiment, show that the broadband side scattering spectrum may be a signature of the "explosion" or "collapse" of the nonlinear plasma wave, accompanied by an explosive photon deceleration. The length of the radiation is very short (on order of tens of microns) compared with the overall laser-plasma interaction length. The location of this broadband $600nm - 2\mu$m but mostly red shifted side scattering signal moves toward the entrance of the gas jet with increasing plasma density as the laser evolves more quickly at high plasma density. For the higher plasma densities, there is a red peak in the spectrum, which shifts towards blue as the plasma density increases. This is because the photon deceleration depends more strongly on the interaction length than the plasma density.

The results of the three-dimensional particle-in-cell code simulations of our experiment agree very well with most of the experimental results. The four phases of the plasma wakefield were reproduced in the simulation. The electron spectrum measured in the experiment agrees with that in the simulation qualitatively.

Even the pointing jitter observed in the experiment was reproduced in a few simulations. The red shifted signal (up to $\sim 1.6\mu$m) due to the photon deceleration was also observed both in experiment and in simulation. However, the simulation doesn't seem to explain the low emittance of the electron beams measured in the experiment. The emittance of the electron beam in the simulations seems to be blown up as a result dephasing and interaction of the electrons with the laser field.

APPENDIX A

Side scattering spectrum

In this chapter we will discuss the results of the spectra measured in the side scattering diagnostic introduced in Chapter 3. These results, as well as the evolution of the plasma front obtained in the probe timing scan of TRR and TRTS in the previous Chapter, help in understanding the physical processes accompanying electron acceleration in a LWFA. As mentioned in the Introduction of chapter1, there are two papers that reported the experimental work on evidences of electron self trapping and the eventual escaping of the electrons from the plasma. One is the PRL paper by Thomas, et al. [65]. It was published in February 2007, shortly after we finished taking the side scattering data in our lab. This paper presented results from spatially- and spectrally-resolved side scattering they called "wave-breaking radiation" in the paper. The authors claim that "the emission is a signature of the violent initial acceleration, and hence can be used as a diagnostic of the self-injection mechanism." The broadband ($\sim$ 500nm to $\sim$ 800nm) emission shown in Fig.A.1 (a figure from Thomas, et al.) is only $\sim 30\mu$m long at a plasma density of $3.2 \times 10^{19} cm^{-3}$, much shorter than the overall interaction length of apparently, $> 450\mu$m. Both the location and the total energy of the emission change with plasma density n_e, as shown in Fig.A.2. the left panel of Fig.A.2 shows that (with large error bars), the total energy E of the emission as a function of n_e can be fit with a linear function. The right panel shows the position of this broadband radiation as a function of n_e and is fit with a function

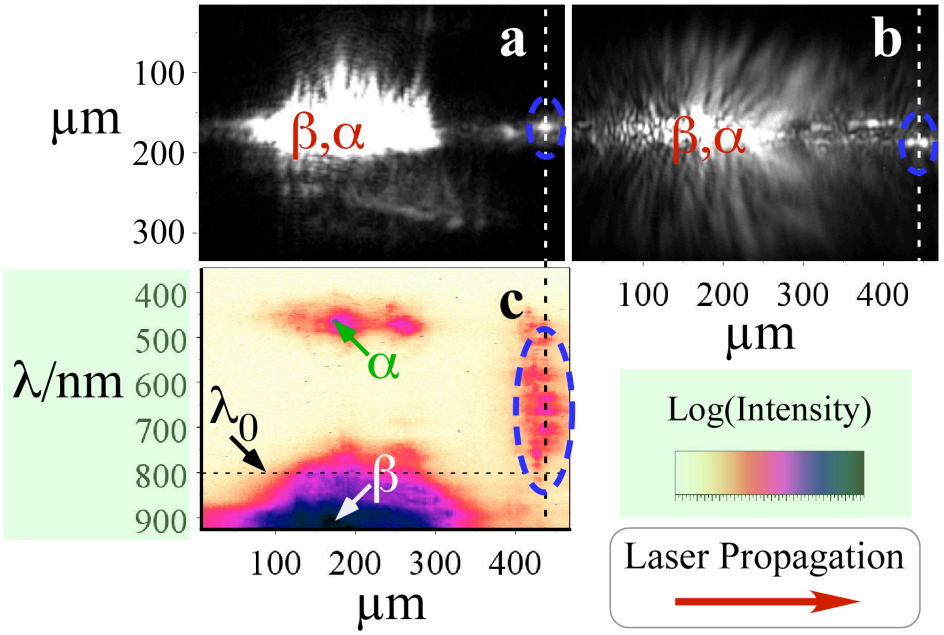

Figure A.1: Figure 2 in the PRL paper by Thomas et al published in 2007. Simultaneous measurement of (a) top view image (b) side view image (with 800 ± 20nm interference filter) and (c) imaging spectrometer for a shot at $3.2 \times 10^{19} cm^{-3}$. The laser propagates from left to right. α and β are the stokes line of Raman side-scatter and its associated second harmonic. Circled is the emission of broadband radiation occurring later in the interaction.

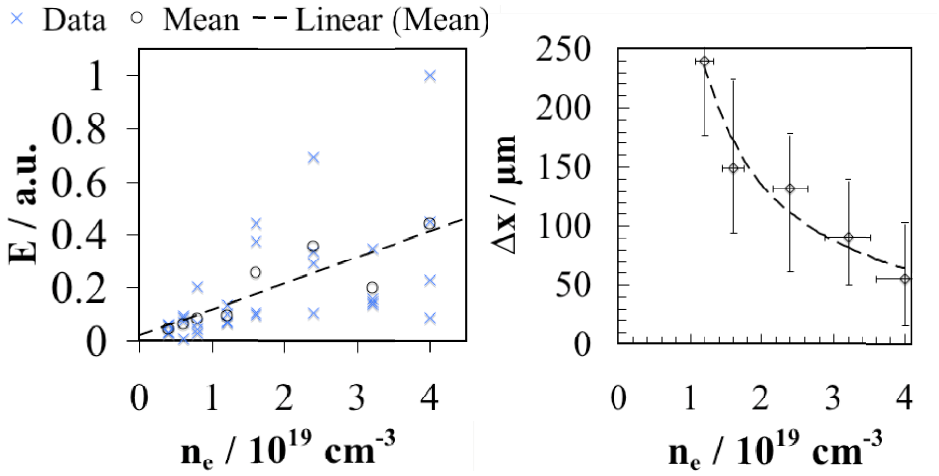

Figure A.2: Figure 3 of the PRL paper by Thomas et al. (Left) The total energy E in the broadband radiation emission as a function of initial electron number density n_e with a linear fit. (Right) The relative position $\delta x$from focus of the earliest emission as a function of n_e with $1/n_e$ fit.

$1/n_e$. This seems consistent with the fact that the higher the n_e, the higher the trapped electron density (left panel) and the quicker evolution of the laser (right panel). The other paper, a PRE by Chang et al [64] published in March 2007, measured the electron trapping and acceleration process using a "tomographic" technique. here, a sequence of shots with identical parameters for the laser and gas jet entrance were taken but with a laser knife to cleave off more and more of the exit of the gas jet, effectively changing the maximum interaction length. Of course the plasma was not sliced off, but the laser knife heated a variable length of the gas jet exit and hydrodynamic expansion subsequently lowered n_e, thus terminating the LWFA interaction. The results in this paper showed that the monoenergetic electrons are all trapped at about the same location, $\sim 600\mu$m from zero density or $\sim 400\mu$m after the density ramp. These trapped electrons are accelerated to $\sim$ 40MeV within 200μm at a plasma density of $4 \times 10^{19} cm^{-3}$.

After that, the electrons maintain the same energy; in other words, no "dephasing" occurs afterward this 200μm acceleration zone. Had there been dephasing the electron energy should have dropped below 40MeV with further propagation. This result of chang et al. at $n_e \simeq 4 \times 10^{19} cm^{-3}$ can be compared to Thomas et al., of Fig.A.2. Note that the broadband emission came from location of $\sim 450\mu$m at a same plasma density. Thomas didn't say where the zero location is, however if it is at the entrance of the uniform density region, this location (where the broadband emission) occurs seems to be the close to the position where the monoenergetic electron trapping and escaping occurs in Chang's paper. This can not be just a coincidence. However, more studies need to be carried out upon this.

The following sections show the results of side scattering diagnostic from the high density 1mm gas jet experiment conducted in our lab, which has similar diagnostics as the work of Thomas et al... The plasma density (see Chapter 3 Fig.2.11 and Fig.2.12) is $\sim 1.5 \times 10^{20} cm^{-3}$, much higher than both of the plasma densities used in the above papers. Comparison of our results with those in these papers will be made below while a detailed discussion will be given later in this Chapter, after correlating the results of the side scattering with the evolution of the plasma front.

A.1 Side scattering spectrum and position

As introduced in Chapter3 Section3.2.5, the side scattering diagnostic images and measures the spectrum of side scattering signal. Fig.A.3 shows the spectrums of the side scattering signals for various pressures. The spectrum are much broader, especially on the red side, than that shown in Fig.A.1. There could be two reasons: the much higher plasma density in our experiment somehow leads

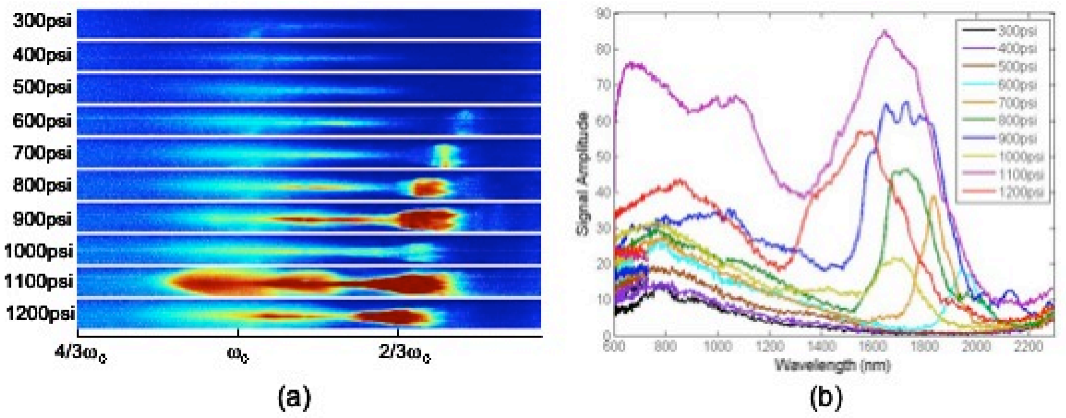

Figure A.3: (a) Side scattering images of a backing pressure scan from 300psi to 1200psi. The horizontal axis is the frequency. The vertical axis of each image from top to bottom, is the laser propagation direction, however the resolution is not very good. The window of the image covers only the bright side scattering signal shown in Fig.A.4. (b). The horizontal line out of (a) for each pressure with the horizontal axis converted to wavelength.

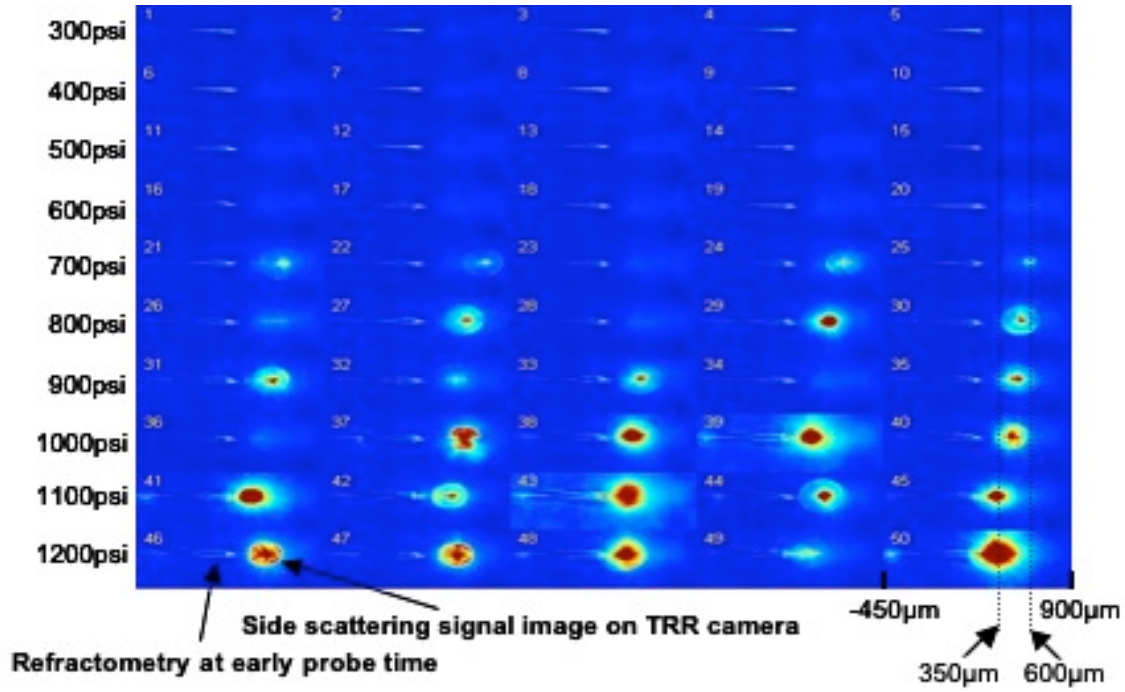

Figure A.4: Refractometry image without the $800/20nm$ interference filter for seeing the broad band side scattering signal (Signal after the front of the refractometry stripe). Laser if traveling from left to right. The probe time is set to be very early so that the refractometry stripe will not overlap the side scattering signal. There are 5 shots for each pressure. The horizontal size of the image is 1350μm, from $z = -450\mu$m to $z = 900\mu$m with the $z = 0$ at the entrance of the gas jet. As the pressure goes up, the location of the side scattering signal moves left, towards the entrance of the gas jet. For the last shot of each pressure, the center moves $\sim 600\mu$m to $\sim 350\mu$m as the pressure rises from 300psi to 1200psi.

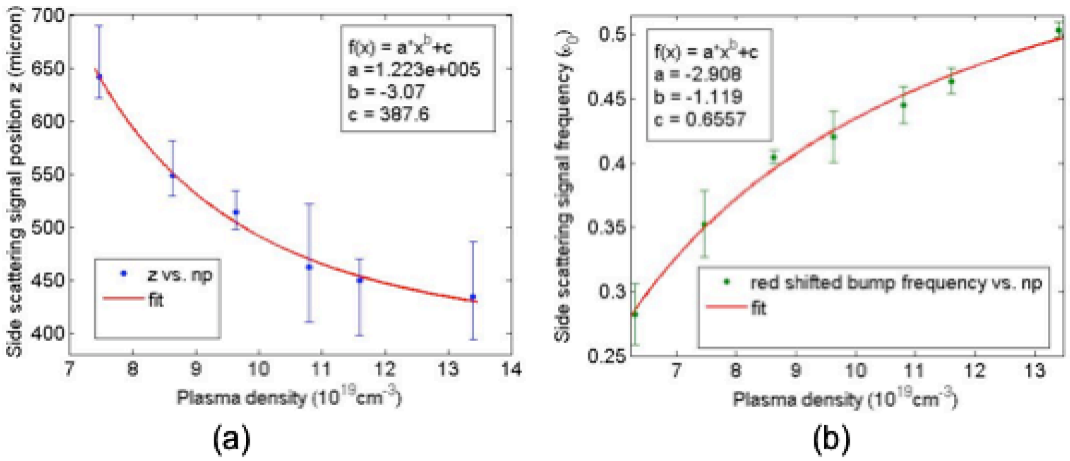

Figure A.5: (a) The position of the side scattering signal versus plasma density. The blue dots with error bars are measured from the images in Fig.A.4; the red curve is the power fit for the data. (b) The frequency of the red shifted bump in the side scattering spectrum (ref Fig.A.3) versus the plasma density. The green dots with error bars are experimental data and the red curve is the power fit for the data.

to a broader spectrum; or, the camera that Thomas used has a narrower spectral response. Figure.A.3a shows the images (raw data) of the side scattering spectrum and Fig.A.3b is simply the lineouts from Fig.A.3a with the horizontal axis switched to wavelength. Figure A.3a shows that the total energy of the SS signal increase with pressure, which agrees with Thomas's results shown in Fig.A.2a. (This particular 1000 psi shot is not typical; it is usually much stronger.) We see from this figure that at higher pressures, there is a "bump" on the red side of the spectrum and it shifts towards "blue" as the pressure goes up. The frequency where this bump occurs is plotted as a function of n_e along with a power fit of $\sim -1/n_e$ in Fig.A.5b. The discussion on this relationship will be made in the end of next paragraph.

The spatial resolution of the side scattering image is not very good, therefore refractometry without 800nm/20nm interference filter is used instead for measuring the location of the side scattering signal. Fig.A.4 shows the locations of the signal for various pressures. The laser is propagating from left to right. There are 5 shots for each pressure. In each image, there is a regular refractometry image plus a side scattering signal because the 800/20nm interference filter before the refractometry camera was removed for the broadband side scattering spectrum to show up on the camera. The probe time for the refractometry is set early so that the side scattering signal occurs later than the time when the probe beam meets the plasma, in other words, the side scattering signal is in front of the plasma front shown in the refractometry image. The length of the side scattering signal is on the order of tens of microns, much shorter than the interaction length. Again from Fig.A.4 it is clear that as the pressure goes up, the total energy of the side scattering signal increases. The location of the signal moves towards the entrance of the gas jet not only as the pressure increases, which was also found by Thomas et al., but also as the total energy of the side scattering signal increases for a

same pressure. If this emission really comes from the electron trapping, they both suggest quicker evolution of the laser at higher trapped electron density. Fig.A.5a plotted the location of side scattering signal as a function of plasma density n_e with a power fit of $\sim n_e^{-3}$, unlike the $1/n_e$ fit in Fig.A.2. Following the fit of $\sim n_e^{-3}$, the side scattering signal would occur much later than what Thomas et al. showed in Fig.A.2 at a plasma density of $3.2^{19} cm^{-3}$. Another difference is that the broadband emission in Fig.A.1 are mostly blue shifted light from the original wave length, while the side scattering signal shown here are mostly red shifted. Assuming the radiation is really a signature of the "initial acceleration" of "100 micro-bunches" of electrons as Thomas claims, the power of the radiation for each electron can be calculated as, $P = \frac{2}{3}\frac{e^2}{m^2c^3}\frac{dE}{dx}^2 = 3.5 * 10^{-14} W$ using an accelerate rate of $\frac{dE}{dx} = 14 GeV/cm$. Multiplying it with a large electron number $\sim 10^8$ and a long interaction time $\sim 100 fs$, the total energy of the radiation is nothing ($3.5 * 10{-}19J$). This energy is not likely to show up on the camera. Another thing is that the "initial accelerations" of "100 micro-bunches" of electrons are not like to occur at the same time (within$\sim 30\mu$m) even from the simulation results in the paper.

One alternative interpretation could be a plasma wave "explosion" or "collapse" theory. The nonlinearity of laser plasma interaction would be higher in a higher density plasma. The plasma density would spike up as well as the red shift of the laser light from photon deceleration. The nonlinearity may reach to a saturation point as it accumulates with the increasing of interaction length. At this point, the plasma wave may "explode" or "collapse" and this process may produce large red shifted emissions. After this explosion, the original plasma wave will disappear and the laser, that may still have enough intensity to drive a new plasma wave, will deplete very fast. If this is true, it explains the location change of side scattering signal with plasma density too. The higher

the plasma density, the earlier this explosion would happen because everything evolves faster at higher plasma density. The frequency shift of photon deceleration, $\langle \triangle \omega_{PA} \rangle \sim (n_e)^{1/2} L$(refer equation4.6), depends more on interaction length L than the plasma density n_e, which explains the the shift of the red bump in the side scattering spectrum decreases less as n_e increase. This particular location of the side scattering signal may be the very spot that the electrons are released from the plasma wave. This could explain that the electrons, after they were accelerated to certain energy, will escape from the plasma wave and maintain the same energy afterwards, as shown by Chang et al. [64]. It makes sense because after the explosion, the plasma wakefield is instantly and temporally gone, which gives the electrons chance to travel freely forwards. Although plasma wakefield may be generated again by the remaining laser energy, it would be behind the electrons since the laser group velocity would drop substantially after the huge photon deceleration.

A.2 Correlation of side scattering signal with probe timing scan results

This section will briefly introduce the results of the evolution of plasma front in high density 1mm gas jet experiments and correlate it with the results of the side scattering diagnostic to see if the above theory still stands. Fig.A.6 shows results of the evolution of plasma front in 1mm gas experiment at a plasma density of $\sim 1.35 \times 10^{20} cm^{-3}$. The green triangles are the TRTS data and the blue dots are the TRR data. This timing scan started from 200μm before the gas jet entrance. The data show that after the laser propagates 450μm inside of the gas jet, the plasma front slips quickly from the laser linear V_g. The group velocity of the laser is proximately the phase velocity of the plasma front, therefore the nonlinear laser

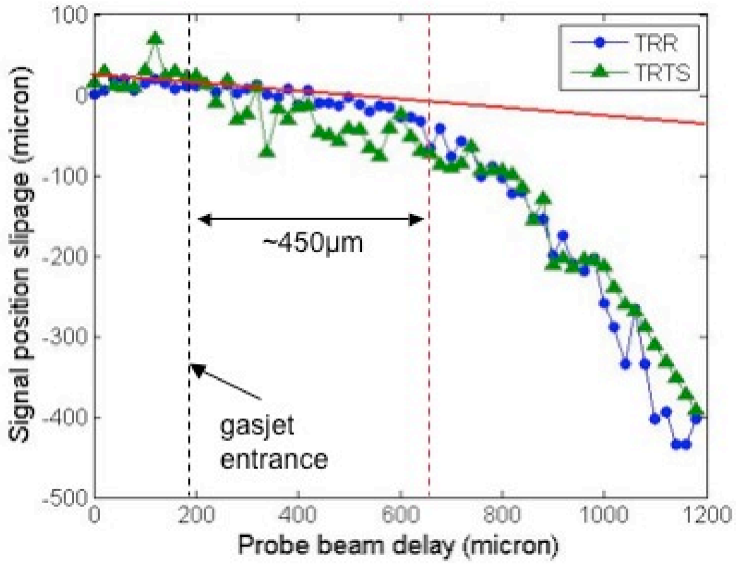

Figure A.6: Moving window probe timing scan results for 1mm gas jet with a plasma density of $\sim 1.35 \times 10^{20} cm^{-3}$. The red line is the group velocity of the laser beam at this plasma density.

V_g drops substantially too at $\sim 450\mu$m inside of the gas jet, which indicate a quick pump depletion as discussed in previous Chapter. Therefore the results support the "explosion" theory in the above paragraph.

A.3 Summary

In summery, this chapter introduced the results of side scattering diagnostics and found that it might be a signature of the "explosion" or "collapse" of the nonlinear plasma wave. The related two papers published recently in 2007 were introduced first. One by Thomas et al showed a similar very short side scattering signal with broadband blue shifted emission. They believed that this emission came from the "initial acceleration" of the self-trapped electrons when they are

accelerated to relativistic energies. The other paper by Chang et al showed that the monoenergetic electrons got trapped together and accelerated about 200μm before they "escape" from the effect of the plasma wave. The side scattering spectrum obtained in out experimental also occurs over a very short (on order of tens of microns) distance. The signals are broadband and mostly red shifted. The location of the signal moves earlier with increasing density. These signals, same or different from that shown in Thomas's paper, are not likely from the electron trapping because otherwise it would be much weaker and occur much earlier over a longer interaction length. However everything seems to be explained if it is really the signature of the "explosion" of the nonlinear plasma wave, which is very likely to happen in such a high density gas jet. The photon deceleration at the "explosion" explains the the location change and the large red shift in the spectrum of the side scattering signals. The instant disappearance of the plasma wave also explains the releasing of electrons without dephasing (results Chang et al showed). This makes a big step on understanding the physical schemes of producing monoenergetic electrons from LWFA.

References

[1] P. Maine, D. Strickland, P. Bado, M. Pessot, and G. Mourou. "Generation of ultrahigh peak power pulses by chirped pulse amplification." *IEEE JOURNAL OF QUANTUM ELECTRONICS*, **24**(2):398–403, Feb 1988.

[2] D. Strickland and G. Mourou. "Compression of amplified chirped optical pulses." *OPTICS COMMUNICATIONS*, **56**:219–221, 1985.

[3] M. Ferray, L. A. Lompre, O. Gobert, A. L'Huillier, G. Mainfray, C. Manus, and A. Sanchez. "Multiterawatt picosecond Nd:glass laser system at 1053 nm." *OPTICS COMMUNICATIONS*, **75**:278–281, 1990.

[4] F. G. Patterson, R. Gonzales, and M. D. Perry. "Compact 10-TW, 800-fa, Nd:glass laser." *OPTICS LETTERS*, **16**:1107–1109, 1991.

[5] C. Sauteret, D. Husson, G. Thiell, S. Seznec, S. Gary, A. Migus, and G. Mourou. "generation of 20-TW pulses of picosecond duration using chirped-pulse amplification in a Nd:glass power chain." *OPTICS LETTERS*, **16**:238–240, 1991.

[6] J. P. Watteau, G. Bonnaud, J. Coutant, R. Dautray, A. Decoster, M. Louis-Jacquet, J. Ouvry, J. Souteret, S. Seznec, and D. Teychenne. "Experimental program on the 20-TW laser system." *PHYSICS OF FLUIDS B-PLASMA PHYSICS*, **4**:2217–2223, 1992.

[7] G. Mourou and D. Umstadter. "Development od applications of compact high-intensity lasers." *PHYSICS OF FLUIDS B-PLASMA PHYSICS*, **4**:2315–2325, 1992.

[8] M. D. Perry and G. Mourou. "Terawatt to petawatt subpicosecond lasers." *SCIENCE*, **64**:917–924, 1994.

[9] K Witte, C Gahn, J Meyer ter Vehn, G Pretzler, A Pukhov, and G Tsakiris. "Physics of ultra-intense laser-plasma interaction." *PLASMA PHYSICS AND CONTROLLED FUSION*, **41**:B221–B230, 1999.

[10] S. C. Wilks P. Amendt, D. C. Eder. "X-ray lasing by optical-field-induced ionization." *PHYSICAL REVIEW LETTERS*, **66**:2589–2592, 1991.

[11] G. D. Enright N. H. Burnett. "Population inversion in the recombination of optically-ionized plasmas." *IEEE JOURNAL OF QUANTUM ELECTRONICS*, **26**:1797–1808, 1990.

[12] N. H. Burnett and P. B. Corkum. "Cold plasma production for recombination extreme ultraviolet lasers by optical-field-induced-ionization." *JOURNAL OF THE OPTICAL SOCIETY OF AMERICA B-OPTICAL PHYSICS*, **6**:1195–1199, 1985.

[13] J. C. Solem, T. S. Luk, K. Boyer, and C. K. Phodes. "Prospects for X-ray amplification with charge-displacement self-channeling." *IEEE JOURNAL OF QUANTUM ELECTRONICS*, **25**:2423–2430, 1989.

[14] M. Tabak, J. Hammer, M. E. Glinsky, W. L. Kruer, S. C. Wilks, J. Woodworth, E. M. Campbell, and M. D. Perry. "Ignition and high gain with ultrapowerful lasers." *PHYSICS OF PLASMAS*, **1**:1626–1634, 1994.

[15] H. Ruhl, S. V. Bulanov, T. E. Cowan, T. V. Liseikina, P. Nickles, F. Pegoraro, M. Roth, and W. Sandner. "Computer simulation of the three-dimensional regime of proton acceleration in the interaction of laser radiation with a thin spherical target." *PLASMA PHYSICS REPORTS*, **27**(5):363–371, May 2001.

[16] T. Tajima and J. M. Dawson. "Laser electron-accelerator." *PHYSICAL REVIEW LETTERS*, **43**(4):267–270, 1979.

[17] T. Katsouleas, C. Joshi, J. M. Dawson, F. F. CHen, C. Clayton, W. B. Mori, C. Darrow, and D. Umstadter. "Plasma accelerators." *AIP CONFERENCE PROCEEDINGS*, (130):63–98, 1985.

[18] T. C. Katsouleas and J. M. Dawson. "Unlimited electron acceleration in laser-driven plasma-waves." *PHYSICAL REVIEW LETTERS*, **51**(5):392–395, 1983.

[19] J. Krall, A. Ting, E. Esarey, and P. Sprangle. "Enhanced acceleration in a self-modulated-laser wake field accelerator." *PHYSICAL REVIEW E*, **48**(3):2157–2161, Sep 1993.

[20] J. Faure, Y. Glinec, A. Pukhov, S. Kiselev, S. Gordienko, E. Lefebvre, J. P. Rousseau, F. Burgy, and V. Malka. "A laser-plasma accelerator producing monoenergetic electron beams." *NATURE*, **431**(7008):541–544, Sep 2004.

[21] S. P. D. Mangles, C. D. Murphy, Z. Najmudin, A. G. R. Thomas, J. L. Collier, A. E. Dangor, E. J. Divall, P. S. Foster, J. G. Gallacher, C. J. Hooker, D. A. Jaroszynski, A. J. Langley, W. B. Mori, P. A. Norreys, F. S. Tsung, R. Viskup, B. R. Walton, and K. Krushelnick. "Monoenergetic beams of relativistic electrons from intense laser-plasma interactions." *NATURE*, **431**(7008):535–538, Sep 2004.

[22] C. G. R. Geddes, C. Toth, J. van Tilborg, E. Esarey, C. B. Schroeder, D. Bruhwiler, C. Nieter, J. Cary, and W. P. Leemans. "High-quality electron beams from a laser wakefield accelerator using plasma-channel guiding." *NATURE*, **431**(7008):538–541, Sep 2004.

[23] C. Joshi, W. B. Mori, T. Katsouleas, J. M. Dawson, J. M. Kindel, and D. W. Forslund. "Ultrahigh gradient particle-acceleration by intense laser-driven plasma-density waves." *NATURE*, **311**(5986):525–529, 1984.

[24] C. E. Clayton, C. Joshi, C. Darrow, and D. Umstadter. "Relativistic plasma-wave excitation by collinear optical mixing." *PHYSICAL REVIEW LETTERS*, **54**(21):2343–2346, 1985.

[25] C. E. Clayton, K. A. Marsh, A. Dyson, M. J. Everett, A. Lal, W. P. Leemans, R. Williams, and C. Joshi. "Ultrahigh-gradient acceleration of injected electrons by laser-excited relativistic electron-plasma waves." *PHYSICAL REVIEW LETTERS*, **70**(1):37–40, Jan 1993.

[26] M. Everett, A. Lal, D. Gordon, C. E. Clayton, K. A. Marsh, and C. Joshi. "Trapped electron acceleration by a laser-driven relativistic plasma-wave." *NATURE*, **368**:527–529, 1994.

[27] A. Lal, D. Gordon, K. Wharton, C. E. Clayton, K. A. Marsh, W. B. Mori, C. Joshi, M. J. Everett, and T. W. Johnston. "Spatio-temporal dynamics of the resonantly excited relativistic plasma wave driven by a CO2 laser." *PHYSICS OF PLASMAS*, **4**:1434–1447, 1997.

[28] C. E. Clayton, M. J. Everett, A. Lal, D. Gordon, K. A. Marsh, and C. Joshi. "Acceleration and scattering of injected electrons in plasma beat-wave accelerator experiments." *PHYSICS OF PLASMAS*, **1**(5):1753–1760, May 1994.

[29] Anthony E. Siegman. *Lasers*. University Science Books, 1986.

[30] H. Hamster, A. Sullivan, S. Gordon, W. White, and R.W. Falcone. "Subpicosecond, electromagnetic pulses from intense laser-plasma interaction." *PHYSICAL REVIEW LETTERS*, **71**:2725, 1993.

[31] F. Amiranoff, S. Baton, D. Bernard, B. Cros, D. Descamps, F. Dorchies, F. Jacquet, V. Malka, J. R. Marques, G. Matthieussent, P. Mine, A. Modena, P. Mora, J. Morillo, and Z. Najmudin. "Observation of laser wakefield acceleration of electrons." *PHYSICAL REVIEW LETTERS*, **81**(5):995–998, Aug 1998.

[32] C. W. Siders, S. P. LeBlanc, D. Fisher, T. Tajima, M. C. Downer, A. Babine, A. Stepanov, and A. Sergeev. "Laser wakefield excitation and measurement by femtosecond longitudinal interferometry." *PHYSICAL REVIEW LETTERS*, **76**(19):3570–3573, May 1996.

[33] J. R. Marques, J. P. Geindre, F. Amiranoff, P. Audebert, J. C. Gauthier, A. Antonetti, and G. Grillon. "Temporal and spatial measurements of the electron density perturbation produced in the wake of an ultrashort laser pulse." *PHYSICAL REVIEW LETTERS*, **76**(19):3566–3569, May 1996.

[34] D. Gordon, K. C. Tzeng, C. E. Clayton, A. E. Dangor, V. Malka, K. A. Marsh, A. Modena, W. B. Mori, P. Muggli, Z. Najmudin, D. Neely, C. Danson, and C. Joshi. "Observation of electron energies beyond the linear dephasing limit from a laser-excited relativistic plasma wave." *PHYSICAL REVIEW LETTERS*, **80**(10):2133–2136, Mar 1998.

[35] P. Sprangle, E. Esarey, J. Krall, and G. Joyce. "Propagation and guiding of intense laser pulses in plasmas." *PHYSICAL REVIEW LETTERS*, **69**:2200, 1992.

[36] T. M. Antonsen, Jr., and P. Mora. "Self-focusing and Raman scattering of laser pulses in tenuous plasmas." *PHYSICAL REVIEW LETTERS*, **69**:2204, 1992.

[37] C. Joshi, T. Tajima, J. M. Dawson, H. A. Baldis, and N. A. Ebrahim. "Forward Raman instability and electron acceleration." *PHYSICAL REVIEW LETTERS*, **47**:1285, 1981.

[38] C. A. Coverdale, C. B. Darrow, C. D. Decker, W. B. Mori, K. C. Tzeng, K. A. Marsh, C. E. Clayton, and C. Joshi. "Propagation of intense subpicosecond laser-pulses through underdense plasmas." *PHYSICAL REVIEW LETTERS*, **74**(23):4659–4662, Jun 1995.

[39] A. Modena, Z. Najmudin, A. E. Dangor, C. E. CLAYTON, K. A. Marsh, C. Joshi, C. B. Darrow, D. Neely, and F. N. Walsh. "Electron aaceleration from the breaking of relativistic plasma waves." *NATURE*, **337**:606–608, 1995.

[40] R. Wagner, S. Y. Chen, A. Maksimchuk, and D. Umstadter. "Electron acceleration by a laser wakefield in a relativistically self-guided channel." *PHYSICAL REVIEW LETTERS*, **78**(16):3125–3128, Apr 1997.

[41] C. I. Moore, A. Ting, K. Krushelnick, E. Esarey, R. F. Hubbard, B. Hafizi, H. R. Burris, C. Manka, and P. Sprangle. "Electron trapping in self-modulated laser Wakefields by Raman backscatter." *PHYSICAL REVIEW LETTERS*, **79**(20):3909–3912, Nov 1997.

[42] W. P. Leemans, D. Rodgers, P. E. Catravas, C. G. R. Geddes, G. Fubiani, E. Esarey, B. A. Shadwick, R. Donahue, and A. Smith. "Gamma-neutron activation experiments using laser wakefield accelerators." *PHYSICS OF PLASMAS*, **8**:2510, 2001.

[43] V. Malka, J. Faure, J. R. Marques, F. Amiranoff, J. P. Rousseau, S. Ranc, J. P. Chambaret, Z. Najmudin, B. Walton, P. Mora, and A. Solodov. "Characterization of electron beams produced by ultrashort (30 fs) laser pulses." *PHYSICS OF PLASMAS*, **8**(6):2605–2608, Jun 2001.

[44] C. Joshi. "The development of laser- and beam-driven plasma accelerators as an experimental field." *PHYSICS OF PLASMAS*, **14**:055501, 2007.

[45] C. Max, J. Arons, and A. B. Langdon. "Self-modulation and self-focusing of electromagnetic waves in plasmas." *PHYSICAL REVIEW LETTERS*, **33**:209–212, 1974.

[46] E. Esarey, P. Sprangle, J. Krall, and A. Ting. "Overview of plasma-based accelerator concepts." *IEEE TRANSACTIONS ON PLASMA SCIENCE*, **24**(2):252–288, Apr 1996.

[47] C. Joshi, T. Tajima, J. M. Dawson, H. A. Baldis, and N. A. Ebrahim. "Forward Raman instability and electron acceleration." *PHYSICAL REVIEW LETTERS*, **47**:1285–1288, 1981.

[48] K. Nakajima, D. Fisher, T. Kawakubo, H. Nakanishi, A. Ogata, Y. Kato, Y. Kitagawa, R. Kodama, K. Miwa, H. Shiraga, K. Suzuki, K. Yamakawa, T. Zhang, Y. Sakawa, T. Shoji, Y. Nishida, N. Yugami, M. Downer, and T. Tajima. "Observation of ultrahigh gradient electron acceleration by a self-modulated intense short laser pulse." *PHYSICAL REVIEW LETTERS*, **74**:4428–4431, 1995.

[49] V. Malka, S. Fritzler, E. Lefebvre, M. M. Aleonard, F. Burgy, J. P. Chambaret, J. F. Chemin, K. Krushelnick, G. Malka, S. P. D. Mangles, Z. Najmudin, M. Pittman, J. P. Rousseau, J. N. Scheurer, B. Walton, and A. E. Dangor. "Electron acceleration by a wake field forced by an intense ultrashort laser pulse." *SCIENCE*, **298**(5598):1596–1600, Nov 2002.

[50] C. D. Decker, W. B. Mori, K. C. Tzeng, and T. C. Katsouleas. "Modeling single-frequency laser-plasma acceleration using particle-in-cell simulations: The physics of beam breakup." *IEEE TRANSACTIONS ON PLASMA SCIENCE*, **24**(2):379–392, Apr 1996.

[51] W. P. Leemans, C. W. Siders, E. Esarey, N. E. Andreev, G. Shvets, and W. B. Mori. "Plasma guiding and wakefield generation for second-generation experiments." *IEEE TRANSACTIONS ON PLASMA SCIENCE*, **24**:331–342, 1996.

[52] A. Pukhov and J. Meyer-ter Vehn. "Laser wake field acceleration: the highly non-linear broken-wave regime." *APPLIED PHYSICS B-LASERS AND OPTICS*, **74**(4-5):355–361, Apr 2002.

[53] W. P. Leemans, B. Nagler, A. J. Gonsalves, C. Toth, K. Nakamura, C. G. R. Geddes, E. Esarey, C. B. Schroeder, and S. M. Hooker. "GeV electron beams from a centimetre-scale accelerator." *NATURE PHYSICS*, **2**(10):696–699, Oct 2006.

[54] P. Sprangle, C. M. Tang, and E. Esarey. "Relativistic self-focusing of short-pulse radiation beams in plasmas." *IEEE TRANSACTIONS ON PLASMA SCIENCE*, **15**(2):145–153, Apr 1987.

[55] S. V. Bulanov, V. I. Kirsanov, and A. S. Sakharov. "Excitation of ultrarelativistic plasma-waves by pulse of electromagnetic-radiation." *JETP LETTERS*, **50**(4):198–201, Aug 1989.

[56] A. Ting, E. Esarey, and P. Sprangle. "Nonlinear wake-field generation and relativistic focusing of intense laser-pulses in plasmas." *PHYSICS OF FLUIDS B-PLASMA PHYSICS*, **2**:1390, 1990.

[57] S. V. Bulanov, I. N. Inovenkov, V. I. Kirsanov, N. M. Naumova, and A. S. Sakharov. "Nonlinear depletion of ultrashort and relativistically strong laser-pulses in an underdense plasma." *PHYSICS OF FLUIDS B-PLASMA PHYSICS*, **4**(7):1935–1942, Jul 1992.

[58] W. Lu, M. Tzoufras, C. Joshi, F. S. Tsung, W. B. Mori, J. Vieira, R. A. Fonseca, and L. O. Silva. "Generating multi-GeV electron bunches using single stage laser wakefield acceleration in a 3D nonlinear regime." *PHYSICAL REVIEW SPECIAL TOPICS-ACCELERATORS AND BEAMS*, **10**:061301, 2007.

[59] G. Matthieussent. "Relativistic particle acceleration using lasers and plasmas." *PLASMA PHYSICS AND CONTROLLED FUSION*, **39**:A161–A175, 1997.

[60] J. M. Dawson. "Nonlinear electron oscillations in a cold plasma." *PHYSICAL REVIEW*, **113**:383–387, 1959.

[61] A. I. Akhiezer and R. V. Polovin. "Dibarton resonance manifestation in deuteron electrodisintegration near pion-production threxhold." *SOVIET PHYSICS-JETP*, **50**:198, 1989.

[62] T. Katsouleas and W. B. Mori. "Wave-Breaking Amplitude of Relativistic Oscillations in a Thermal Plasma." *PHYSICAL REVIEW LETTERS*, **61**:90, 1988.

[63] C. T. Hsieh, C. M. Huang, C. L. Chang, Y. C. Ho, Y. S. Chen, J. Y. Lin, J. Wang, and S. Y. Chen. "Tomography of injection and acceleration of monoenergetic electrons in a laser-wakefield accelerator." *PHYSICAL REVIEW LETTERS*, **96**(9):095001, Mar 2006.

[64] C. L. Chang, C. T. Hsieh, Y. C. Ho, Y. S. Chen, J. Y. Lin, J. Wang, and S. Y. Chen. "Production of a monoenergetic electron bunch in a self-injected laser-wakefield accelerator." *PHYSICAL REVIEW E*, **75**(3):036402, Mar 2007.

[65] A. G. R. Thomas, S. P. D. Mangles, Z. Najmudin, M. C. Kaluza, C. D. Murphy, and K. Krushelnick. "Measurements of wave-breaking radiation from a laser-wakefield accelerator." *PHYSICAL REVIEW LETTERS*, **98**(5):054802, Feb 2007.

[66] O. E. Martinez. "3000 times grating compressor with positive group velocity dispersion: Application to fiber compensation in 1.3-1.6 micron region." *IEEE JOURNAL OF QUANTUM ELECTRONICS*, **QE-23**(1):59–64, Jan 1987.

[67] M. M. Murnane, H. C. Kapteyn, and R. W. Falcone. "High-Density Plasmas Produced by Ultrafast Laser Pulses." *PHYSICAL REVIEW LETTERS*, **62**:155, 1989.

[68] W. P. Leemans, C. E. Clayton, W. B. Mori, K. A. Marsh, P. K. Kaw, A. Dyson, and C. Joshi. "Experiments and simulations of tunnel-ionized plasmas." *PHYSICAL REVIEW A*, **46**:1091–1105, 1992.

[69] S. Semushin and V. Malka. "High density gas jet nozzle design for laser target production." *REVIEW OF SCIENTIFIC INSTRUMENTS*, **72**(7):2961–2965, 2001.

[70] K. Bockasten. "Transformation of Observed Radiances into Radial Distribution Transformation of Observed Radiances into Radial Distribution of the Emission of a Plasma." *JOURNAL OF THE OPTICAL SOCIETY OF AMERICA*, **51**(9):943–947, 1961.

[71] E. Hecht. *Optics*. Addison Wesley Longman, 3 edition, 1998.

[72] C. E. Clayton. "Diagnostics for laser accelerators." In V. Yakimenko, editor, *American Institute of Physics Conference Series*, volume 737, pp. 137–159, 2004.

[73] W. B. Mori. "The physics of the nonlinear optics of plasmas at relativistic intensities for short-pulse lasers." *IEEE JOURNAL OF QUANTUM ELECTRONICS*, **33**(11):1942–1953, Nov 1997.

[74] C. D. Decker and W. B. Mori. "Group-velocity of large-amplitude electromagnetic-waves in a plasma." *PHYSICAL REVIEW LETTERS*, **72**(4):490–493, Jan 1994.

[75] S. C. Wilks, J. M. Dawson, W. B. Mori, T. Katsouleas, and M. E. Jones. "Photon accelerator." *PHYSICAL REVIEW LETTERS*, **62**(22):2600–2603, May 1989.

[76] C. D. Murphy, R. Trines, J. Vieira, A. J. W. Reitsma, R. Bingham, J. L. Collier, E. J. Divall, P. S. Foster, C. J. Hooker, A. J. Langley, P. A. Norreys, R. A. Fonseca, F. Fiuza, L. O. Silva, J. T. Mendonca, W. B. Mori, J. G. Gallacher, R. Viskup, D. A. Jaroszynski, S. P. D. Mangles, A. G. R. Thomas, K. Krushelnick, and Z. Najmudin. "Evidence of photon acceleration by laser wake fields." *PHYSICS OF PLASMAS*, **13**(3):033108, Mar 2006.

[77] A. Modena, Z. Najmudin, A. E. Dangor, C. E. Clayton, K. A. Marsh, C. Joshi, V. Malka, C. B. Darrow, and C. Danson. "Observation of Raman forward scattering and electron acceleration in the relativistic regime." *IEEE TRANSACTIONS ON PLASMA SCIENCE*, **24**(2):289–295, Apr 1996.

[78] W. B. Mori. "Generation of tunable radiation using an underdense ionization front." *PHYSICAL REVIEW A*, **44**(8):5118–5121, 1991.